CRANFIELD UNIVERSITY

School of Engineering

M.Sc. by Research Thesis

Full Time

February 2013 - February 2014

Pablo Aguado

Large-Eddy Simulation of air-fuel mixing in Dry Low NOx GTU Combustor

Supervisor:

Dr. Panagiotis Tsoutsanis

February 2014

Except where acknowledged in the customary manner, the material presented in this thesis is, to the best of my knowledge, original and has not been submitted in whole or part for a degree in any university.

_____

Name of the Student

Abstract

The in-house code FLAMENCO is developed to simulate the mixing process in a Dry Low NOx GTU Combustor. The physical approach is defined to model 3D-unsteady, compressible, multi-species flows where turbulence plays a major role. For this purpose, Large Eddy-Simulation is applied in conjunction with high-order schemes and stable formulation of volume fraction advection. Regarding the numerical structure, FLAMENCO is a Finite-Volume Godunov-type algorithm equipped with 5^{th} and 2^{nd} Order non-oscillatory reconstruction in space and 2^{nd} Order, 4-Stages Explicit Runge-Kutta scheme for integration in time. From a mathematical point of view, the multi-species approach is governed by the 5-Equation Transport Model and is thermodynamically defined by iso-baric and perfect gas considerations, which prevent pressure oscillations. Finally, an HLLC approximate Riemann solver computes convective fluxes and 2^{nd} Order centred differences accounts for dissipation terms.

Previous research with an old version of FLAMENCO failed due to low dissipation in the jet injector tube. This issue stems from local energy being uncontrollably introduced in this small region, leading to unphysical pressure values. It was found that the combination of reflecting inflow, small cells and high gradients is responsible for acoustic wave reflection and amplification. To overcome this problem, a number of modifications including boundary conditions (Partially Non-reflecting, Non-reflecting and Nozzle-type subsonic inflows and outflows), an Adaptive Reconstruction Scheme, a more dissipative reconstruction scheme (5^{th} Order WENO) and grid changes (only in jet injector) have been introduced. As a result, local energy generation and evacuation become balanced within physical boundaries, providing stable conditions in the whole domain.

Initially, extensive validation of the new numerical approach is conducted through contrasted test cases such as Stationary and Moving Contact Wave, Shock Tube Problem, Kelvin-Helmholtz Instability and 2D-3D Explosion Problems. In the same way, strategies intended to overcome the low dissipation problem are analysed in a representative configuration. After the validation process, several simulations involving coarse and fine grids and different reconstruction schemes are run in the Dry Low NOx GTU Combustor. Finally, results are compared with experimental data, showing really good accuracy for 5^{th} Order schemes, which is specially surprising in the coarse grid. In this way, highly turbulent, heterogeneous structures such as Vortex Breakdown, Central Recirculation Zone, Precessing Vortex Core and Secondary Vortices are very well captured, demonstrating the suitability of the mixing model to deal with highly turbulent flows where critical shear layers and high mixing ratios coexist in confined domains.

Acknowledgements

This thesis could never have been written without the immeasurable support of many people. Since it is impossible for me to thank them all in just a few lines, I will focus on those whose encouragement made me give the best of myself.

Firstly, I would be eternally grateful to Dr. Ben Thornber for trusting and waiting for me to develop this project and for providing me with such a wonderful tool as FLAMENCO. His patience, help and support made things much easier and his wise advice guides me even today. I would also like to express my most sincere gratitude to Dr. Panagiotis Tsoutsanis, who not only made an incredible effort to catch up with the project in record time, but also proposed extremely smart ideas that undoubtedly increased the quality of the project. I will never forget the tireless support and understanding of Dr. Tsoutsanis, specially in the last stage of the research. It is important to me to mention Dr. Nick Asproulis, who always welcomes me with a smile on his face and dedicates me as much time as I need. I truly appreciate his support and trust in my work. Finally, I would like to thank people from Perm University for so much effort put on the research.

On a more personal note, I would like to thank my girlfriend Francesca for her continuous support. She shared joys and pains with me during this process and as far as I am concerned, she is as much responsible for this work as I am. Finally I would like to thank my sister, my father and my mother for being the greatest support in my whole life. Their love makes me face every new adventure with a smile on my face.

Pablo L. Aguado

Contents

List of Figures

List of Tables

Nomenclature

Operators and mathematical definitions

$\frac{\partial(.)}{\partial t}$	Partial derivative with respect to variable t
∇	Gradient
$\cdot$	Scalar Product
$\overline{(.)}$	Vector
$\otimes$	Tensor product
$\overline{\overline{(.)}}$	Tensor
$TI(.)$	Time integration operator

Acronyms

DLNOXGTUC	Dry Low NOx GTU Combustor
HCCI	Homogeneous Charge Compression Ignition
LES	Large-Eddy Simulation
ILES	Implicit Large-Eddy Simulation
NO_x	Oxides of nitrogen
CRZ	Central Recirculation Zone
PVC	Precessing Vortex Core
HLLC	Harten, Lax and van Leer Contact
HLL	Harten, Lax and van Leer
MUSCL	Monotone Upstream-Centred Schemes for Conservation Laws
EOS	Equation Of State
TVD	Total Variation Diminishing

ENO	Essentially Non-Oscillatory
WENO	Weighted Essentially Non-Oscillatory
MLP	Multi-dimensional Limiting Process
CFL	Courant - Friederich-Lewy number
RK	Runge-Kutta
HPC	High Performance Computing
MPI	Message Passing Interface
5thLID	5^{th}Order reconstruction Long Inner Duct

Latin letters

t	Time
Y_k	Mass fraction of Species k
z_k	Volume Fraction of Species k
p_k	Pressure of Species k
N	Number of Species
u, v, w	Orthogonal components of velocity
p_k^I	Pressure of Species k at the multifluid interface
v_k^I	Velocity of Species k at the multifluid interface
p	Static Pressure
P	Total Pressure
$\bar{\bar{I}}$	Unit tensor
E	Total Energy
q	Heat transfer
x, y, z	Curvilinear components in space
Δt	Time step
C_p	Heat capacity at constant pressure
C_v	Heat capacity at constant volume
R	Specific gas constant
T	Temperature

$\overline{U}$	Vector of conserved variables
$\overline{F}, \overline{G}, \overline{H}$	Flux vectors in ξ, η and ζ directions
n	nth time step
V	Volume
S_L, S_*, S_R	Wave speeds in left, intermediate and right states
i, j, k	Subscript in x, y and z directions
$\overline{\overline{J}}$	Jacobian tensor
Jac	Jacobian
A	Kelvin-Helmholtz instability amplitude
a	Speed of Sound
h	Enthalpy
k	Kelvin-Helmholtz instability frequency
K	Heat Conduction coefficient
L	Characteristic longitude / Wave Temporal Amplitude
D_s	Swirler outer diameter
D_{s_0}	Swirler inner diameter
D_J	Jet injector diameter
D_C	Combustion Chamber diameter
D_L	Combustion chamber length
V_{x_J}	Axial Jet FlowVelocity
V_{x_S}	Axial Swirl Flow Velocity
V_{θ_S}	Tangential Swirl Flow Velocity
V_θ	Tangential velocity
V_r	Radial velocity
Re	Reynolds Number
S	Swirl Number
y^+	Dimensionless perpendicular distance first cell - wall
x^+	Dimensionless length parallel to wall

Greek letters

ρ_k	Density of Species k
ρ	Mixture Density
λ	Velocity Relaxation Coefficient / Local Riemann Problem eigenvalue
σ	Viscous stress tensor / surface element
τ	Reynolds stress tensor
ϕ	General Variable
ψ	Limiting Function
ε	Specific internal energy / Relaxation time
β	Face Jacobian / WENO Relaxation Coefficients
ξ, η, ζ	Cartesian components
$\Delta\xi, \Delta\eta, \Delta\zeta$	Length interval in ξ, η and ζ directions
μ	Dynamic viscosity / Pressure Relaxation Coefficient
ν	Kinetic viscosity
γ	Specific heat capacity ratio
η_α	Gaussian Integration Point
ζ_β	Gaussian Integration Point
δ	Differential / Boundary Layer thickness

Chapter 1

Introduction

1.1 Dry Low NOx Gas Turbine Unit Combustor as future technology

One of the main challenges faced by today's society is sustainable development. In a changing globalised world where competition reaches unimaginable levels and industrial companies fight to clear their way towards a better position in the market, a responsible development is crucial to ensure durability of society and a future with sustainable consumption of finite resources. In their attempt to manage the situation, governments are introducing restrictive laws that constrain the conception of new technologies within many fields of development. Obviously, the energy sector is directly affected by such regulations, which are inducing a change of mentality at very basic levels. As a consequence, new designs are no longer devised under a few criteria of power and strength, but they must fulfil several requirements with a "mandatory" status. In this way, focusing on devices involving chemical-to-mechanical energy transformation, factors such as efficiency, pollutant emissions, cost, reliability, robustness, durability or weight have become essential whenever a new product is projected.

The energy sector has been deeply affected by this change in mentality and in the way engineering has to be understood. The fact that traditional energy sources such as oil and gas are running low is forcing on the one hand the development of cleaner and more efficient methodologies to deal with them and on the other hand the consideration of new unlimited renewable energies. Any contribution within these fields that helps improving the state-of-the-art of such technologies is therefore of high utility.

The extraction of chemical energy and its transformation to mechanical power are processes occurring everywhere nowadays. For instance, cars, ships, planes and electricity generation are elements that rely on such mechanisms to operate. As a consequence, the improvement of their performance is subjected to correct understanding of energy transference processes. Although great progress has been done in the matter, there are still many issues to be addressed in order to have broader control and to reach sustainable levels of energy production.

Devising modern tools for chemical energy extraction and its conversion to mechanical (or kinetic) power must take into account not only the above mentioned requirements of certain levels of efficiency, robustness, cost, etc., but also strict restrictions in pollutant emissions. Therefore, novel cutting-edge designs must be produced in order to be successful. Among such designs, the Dry Low NOx Gas Turbine Unit Combustor (see Figure 1.1 for typical configurations) emerges as an efficient element where combustion is produced in a clean way and where the usage of unnecessary raw materials is minimised.

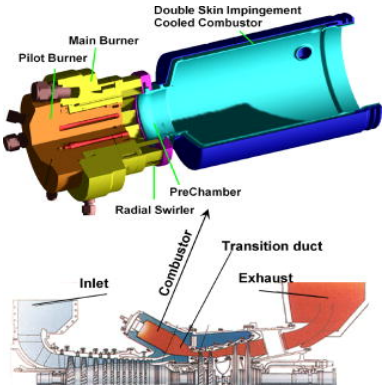

(a) CAD Model

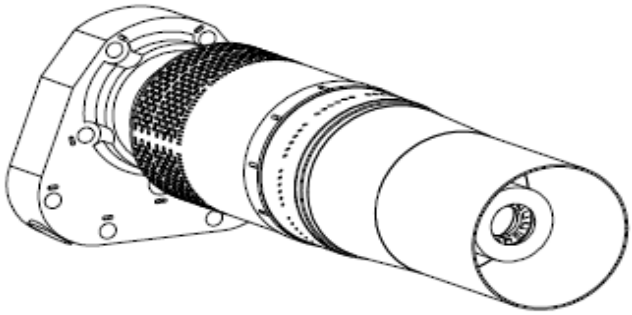

(b) Combustor plus nozzle. Reproduced from [1]

Figure 1.1: Typical Dry Low NOx Combustor design

Modern Dry Low NOx GTU combustors make use of innovative technologies to generate large amounts of mechanical power (usually employed for electric energy production) from relatively small quantities of gas or liquid fuel. As stated in Davis et al. [1] and Washam [2], in addition to high efficiency and reliability, these machines yield very low pollutant emissions in general and NOx in particular, as seen in Figure 1.2 (as a reference point, consider that typical Gas Turbines emit between 100 to 600 ppm of NOx). The major advantage of this type of gas turbines is that they decrease dramatically the employment of traditional cleaning mechanisms (water and steam injection) associated with NOx reduction by using lean premixed components under certain working conditions. As a consequence, the negative effects derived from the utilisation of such traditional methods (efficiency losses, water induced pollutants, etc.) are avoided without sacrificing performance. Finally, another important advantage of Dry Low NOx GTU combustors is their ability to deal with many different fuels, ranging from oil and gas to biofuels (see Siemens SGT-100 [3])

	Gas			Distillate		
Turbine Model	NOx (ppmvd)	CO (ppmvd)	Diluent	NOx (ppmvd)	CO (ppmd)	Diluent
MS3002(J)-RC	33	25	Dry	N/A	N/A	N/A
MS3002(J)-SC	42	50	Dry	N/A	N/A	N/A
MS5001P	25	50	Dry	65	20	Water
MS5001R	42	50	Dry	65	20	Water
MS5002C	42	50	Dry	65	20	Water
MS6001B	9	25	Dry	42	30	Water
MS7001B/E Conv.	25	25	Dry	42	30	Water
MS7001EA	9	25	Dry	42	30	Water
MS9001E	15	25	Dry	42	20	Water
	25	25	Dry	90	20	Dry
MS6001FA	25	15	Dry	42/65	20	Water/Steam
MS7001FA	25	15	Dry	42/65	20	Water/Steam
	9	9	Dry	42/65	30	Water/Steam
MS7001FB	25	15	Dry	42	20	Water
MS7001H	9	9	Dry	42/65	30	Water/Steam
MS9001EC	25	15	Dry	42/65	20	Water/Steam
MS9001FA	25	15	Dry	42/65	20	Water
MS9001FB	25	15	Dry	42	20	Water
MS9001H	25	15	Dry	42	20	Water

Figure 1.2: Pollutant emissions of different Dry Low NOx GTU Combustors. Reproduced from [1]

1.2 Mixing Processes

Energy transformation within the Dry Low NOx GTU combustor is divided, as occurs in non-premixed engines, into three well-differentiated stages: Injection, Mixing and Combustion. Although the exact boundaries of these stages are not strictly defined and may vary depending on who is performing the analysis, it is commonly accepted that the Injection stage includes all phenomena occurring within the injector and in the near region of the injector exit, the Mixing stage involves relatively unconfined flows which interact through a complex mass, momentum and heat exchange mechanism delivering a suitable fluid mixture of reactants ready to burn, and the Combustion stage considers all processes transforming such mixture into burned products. The present study focuses on the Mixing stage, addressing all the relevant phenomena that characterise the evolution of the flow at this point.

There are endless mixing processes taking place in nature, and so are the features that appear in them. For instance, from an engineering point of view, the injection and subsequent mixing in Diesel Engines, Petrol Engines, Jet Engines, Gas Turbines, Rocket Engines, domestic combustion, etc., differ significantly from one to another (see Figure 1.3), indicating that different approaches must be used when addressing any of such processes. In the case under consideration, two non-premixed flows are coaxially injected inside the combustion chamber where mixing takes place. Whereas the inner jet is set only with axial velocity, the outer flow is delivered with both axial and rotational velocities (see Figure 1.4 for a typical flow field derived from this configuration), inducing adverse

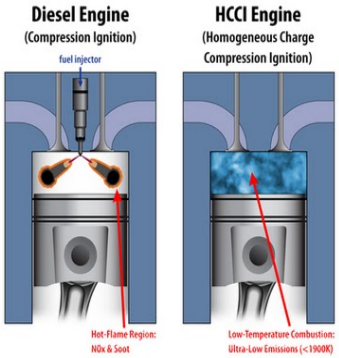

(a) Diesel and HCCI Engines

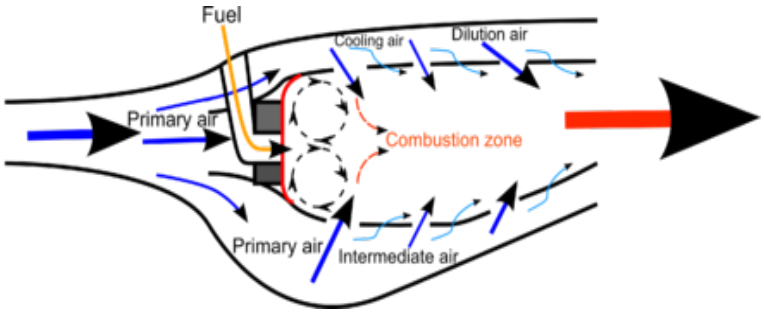

(b) Gas Turbine Combustor

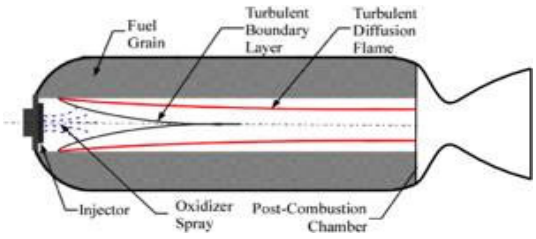

(c) Rocket Engine

(d) Space Shuttle injector

Figure 1.3: Devices where different Injection and Mixing processes occur

pressure gradients that allow proper species recirculation and mixing. This concept of coaxially injected axial and swirl flows is really advantageous in constant pressure burning devices such as Gas Turbines or Jet engines, since it allows matching flame and flow speeds leading to quick and efficient mixing. In internal combustion engines, its usage is not as generalised, but as demonstrated in Miles [4] adaptations of the idea are currently being assessed in order to take the advantages while minimising the disadvantages (swirl flows in internal combustion engines bring additional problems due to higher restrictions in space, pressure, time, etc.). As for the specific physical phenomena occurring inside the Dry Low NOx GTU combustor, details are commented in Section 2.1.

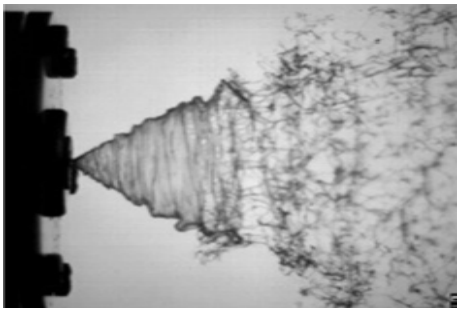

Figure 1.4: Typical flow field derived from coaxially injected Swirl-axial flows. Reproduced from [5]

1.3 Approach with FLAMENCO

The mixing process addressed in the present study has a well-defined configuration. Since real operating conditions range from gas to liquid fuels and oxidisers at many different injection speeds, it is difficult to generate a global model whose applicability is justified in any case. Therefore, analyses have to be particularised, using physical assumptions, mathematical models and numerical methods according to the case under consideration. In this study, experimental data obtained by Midgley et al. [6] using water for both the jet (inner stream) and swirling flow (outer stream) in the rig shown in Figure 1.5 have been utilised as the reference basis to compare with numerical results. In order to represent accurately real Gas Turbine combustion processes using liquid fuels and oxidisers, such experimental information was generated under typical operating conditions.

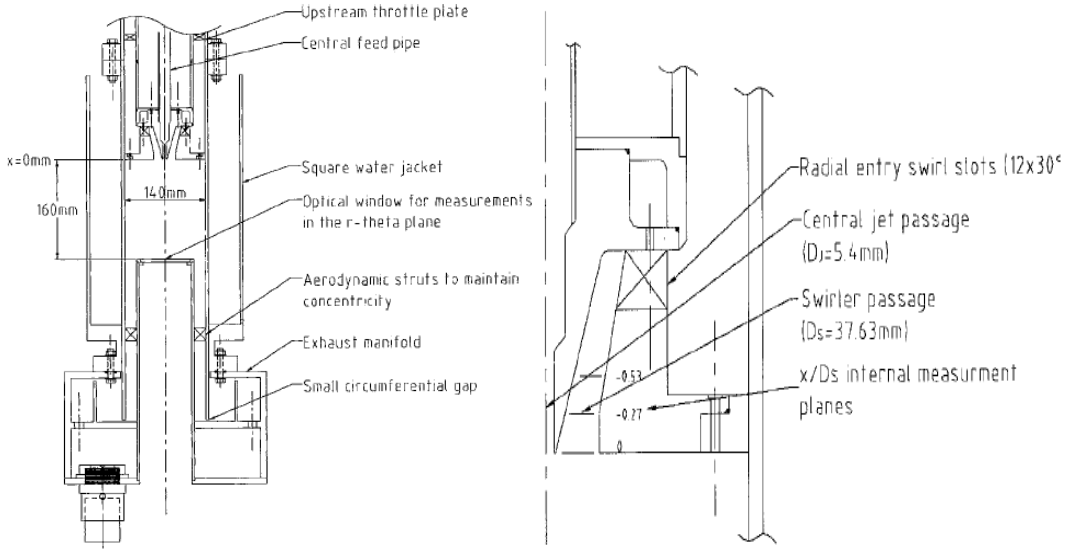

Figure 1.5: Experimental Rig used in [6]

Although ideally an incompressible code would provide the best results, this research addresses the problem from a compressible perspective using FLAMENCO, a numerical algorithm built to deal with compressible fluids. Obviously, the code notices that the speed of sound is much higher than the characteristic velocities and acts in consequence by applying the corresponding adjustments (see Low Mach Correction in Thornber [7]). In the same way, the characteristic non-dimensional parameters of the problem are specified carefully to make results consistent and comparable.

The present case has been approached before in Aguado [8] using a primary version of FLAMENCO. In that work, large discrepancies between numerical and experimental data were found, especially from a quantitative point of view. Indeed, despite the most important flow features were captured, their intensity and precise location within the

combustion chamber were significantly wrong. Therefore, the present study has been partially dedicated to understand and correct the factors that triggered such inaccuracies.

After deep analysis, it was found that the reason behind the erroneous predictions in [8] was the extremely low dissipation generated in this particular case by the first version of FLAMENCO. The effects of such low dissipation were masked in almost the whole domain, where large characteristic longitudes and relatively low velocities allow energy evacuation and equilibrium. However, inside the jet injector tube (bounded by the subsonic inflow and the exit to the combustion chamber), a dramatic combination of small cells, large characteristic velocities and numerical energy production led to unbalanced energy creation. As a consequence, small amounts of this quantity were systematically added to the existing values, provoking non-physical and uncontrolled increments in pressure which ultimately triggered a non-physical rotational flow inside this inner duct. These effects had an evident impact on subsequent flow features within the combustion chamber.

The detailed mechanism by which low dissipation is not able to balance energy production is as follows:

1. The low pressure region located near the small vertical wall between the jet and swirl injectors introduces expansion waves inside the inner tube, decreasing pressure near the walls of the jet injector (as seen in Figure 1.6). This phenomenon is produced throughout the whole simulation, affecting the total energy in a continuous way.

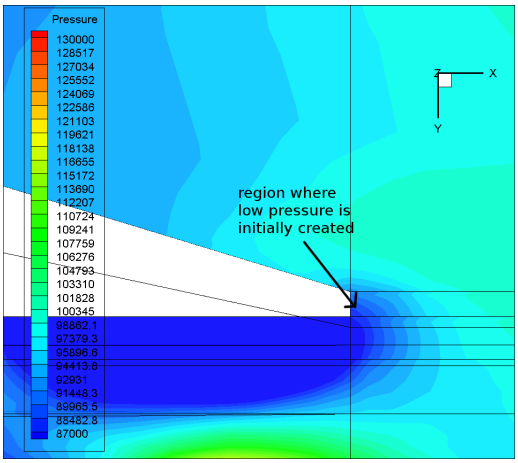

Figure 1.6: Regions where low pressure is initially developed

2. These expansion waves propagate near the walls of the duct, reflecting on them and increasing their intensity as energy is introduced from the inflow (incoming pressure waves) and the outflow. This leads to a complex aeroacoustic configuration where low pressure regions move, attached to the walls, describing a characteristic helical motion. These low pressure "bags" increase their absolute magnitude and induce a

non-physical transversal flow inside the jet injector which eventually creates high pressure areas opposed to the lower ones. It is important to mention that the point of minimum (or maximum) pressure is always located approximately at the middle of the tube, which is probably due to the fact that this is the region where local acoustic wave are less damped since it is more independent from the conditions imposed both at the inflow and the end of the duct. Figures 1.7 and 1.8 evidence the sequence described, where it is easily visible how the minimum value of pressure is produced approximately at the middle of the duct, increasing its magnitude and describing a helical motion.

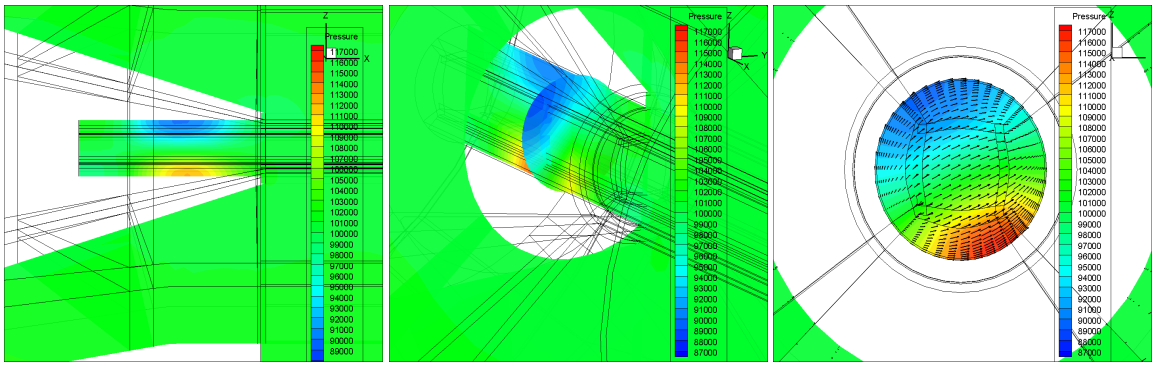

(a) Pressure bags attached to the walls. Transversal view

(b) Isometric view showing the helical layout

(c) Transversal view at the middle of the duct representing pressure contours and velocity vectors. Note that velocity depicted here was induced by pressure gradients in previous time steps

Figure 1.7: Pressure contours and velocity vectors within the jet injector

3. At this point, numerical dissipation is unable to transform local energy associated with acoustic waves. Two are the main reasons for this, namely the small cells defined in the region, where the Jacobian is extremely small, and the subsonic inflow which is not only unable to evacuate enough energy but may also introduce more. Since the local dissipation rate is lower than the creation rate, the maximum and minimum values of pressure increase.

4. As the pressure jump within the inner injector increases, so does dissipation, reaching a state where both maximum and minimum values find a boundary. At this point, local dissipation balances the creation of energy associated with pressure waves. In a standard simulation, values of approximately 287000 Pa for the maximum and 50000 Pa for the minimum were found.

This study has been largely dedicated to devise ways of overcoming this limiting issue. The techniques considered can be grouped into three different categories:

- **Geometrical**: Consists of modifying the grid either to increase dissipation within the inner injector or to decrease the creation of energy produced in this region. The

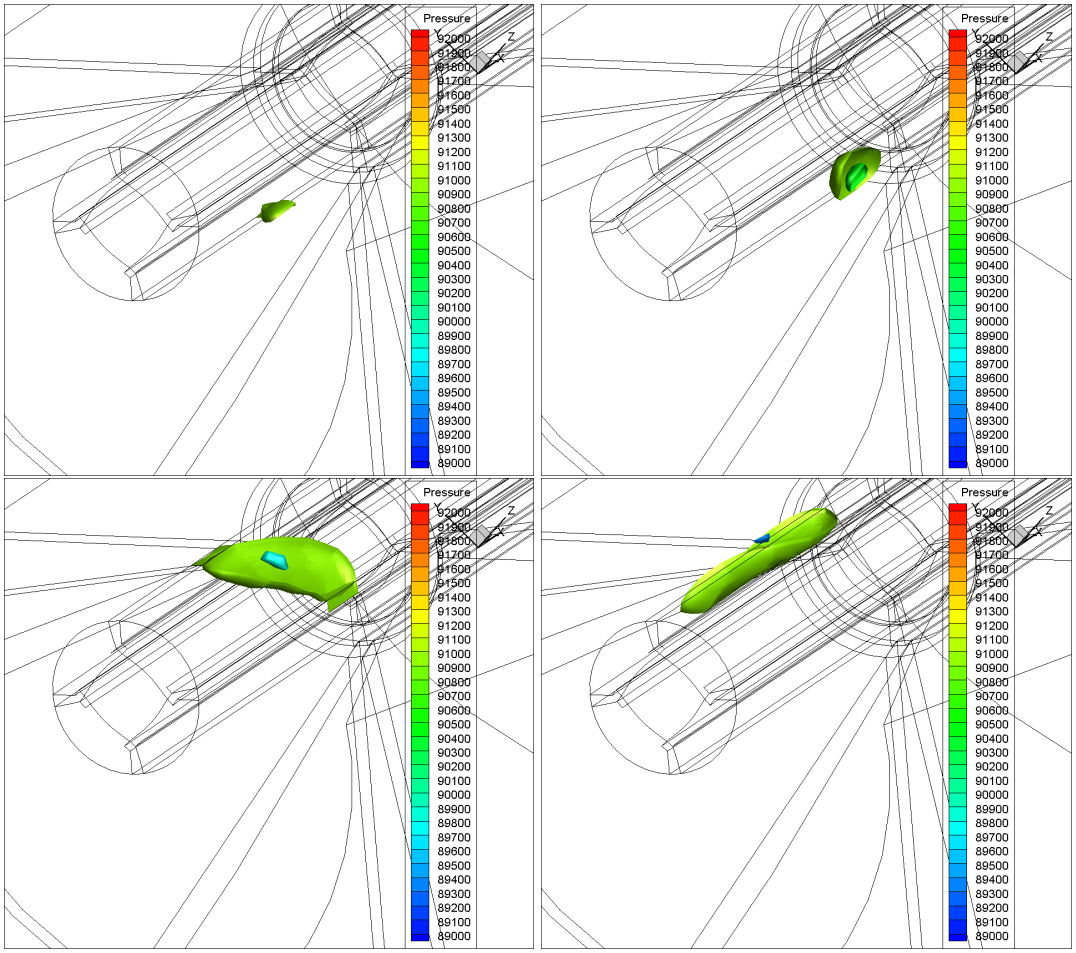

Figure 1.8: Pressure Iso-surfaces within the jet injector at different output times (increasing time from left to right and up to bottom). Two Iso-surfaces are represented, one at constant pressure 91000 Pa and the other at the maximum (in magnitude) in each case

addition of large cells at the beginning of the tube or the use of smaller inner ducts have been considered.

- **Acting over the Boundary Conditions**: This technique is based on implementing different inflow conditions so the excess of energy can be evacuated while keeping the necessary information that this boundary has to introduce. In this way, Non-Reflecting Subsonic Inflow, Partially Non-reflecting Subsonic Inflow and Stagnated Subsonic Inflow have been tested. Additionally, in order to damp acoustic waves bouncing on the walls, additional numerical dissipation has been introduced at the walls of the jet injector through an Adaptive Scheme. Details of this are given in Section 4.2.3.

- **Numerical**: Refers to alternative high-order high-resolution reconstruction schemes to those proposed in [8]. In this case, a 5^{th} Order WENO scheme has been developed to simulate the whole problem.

After several tests, it was found that best results were not obtained with one of the above

strategies, but with a calibrated combination of geometrical modifications, redefinition of boundary conditions and implementation of adaptive reconstruction schemes.

1.4 Motivation

As the requirements concerning combustion systems in general and Gas Turbines in particular become more and more restrictive, the necessity of new cutting-edge design technologies increases. Current market and governmental specifications are forcing the definition of efficient, robust, reliable and cheap devices with very low pollutant emissions, leading to a scenario where the tools and methodologies employed play a vital role. Since this trend is not only expected to continue in the future, but become more intense, it is clear that more emphasis must be placed in such stages of the development process.

The definition and development of the optimum configuration is only achievable if one possesses the adequate tools. In particular, accurate numerical algorithms are essential in order to provide fast, reliable and economically viable results. The present work arises as a natural consequence of this issue, proposing a numerical model for the simulation of flow within typical Gas Turbine combustors. Although the study of the Dry Low NOx GTU combustor was initially considered, the interest of an algorithm not only limited to Gas Turbine applications, but also suitable for more general problems (boundary layer-shock wave interactions, highly mixed flows, etc.) motivated the development of FLAMENCO as an LES three-dimensional, compressible, multispecies code.

For the sake of completion, during the development of the code additional features were added to the baseline algorithm. In this way, conventional and specifically-developed models were introduced regarding the reconstruction method of the convective fluxes, thermodynamic and mixing laws, time integration and boundary conditions. This way of proceeding not only allows comparison with typical models in the literature within the same numerical environment, but also provides a global tool with the capacity to be particularised for each problem under consideration.

Finally, the growing industrial usage of natural gas in Gas Turbines to plug the “energy gap” in electricity generation motivated a comprehensive study of the flow dynamics within the Dry Low NOx GTU combustor, a common architecture employed in such devices. Although nowadays it is mainly restricted to this sort of applications, the use of natural gas in Gas Turbines is spreading to other systems. Additionally, its suitability for jet engines is being assessed, potentially increasing the interest in this technology. As a consequence, the idea of a better understanding of the physics in this type of problems encourages the research.

1.5 Objectives

The main objective of this research is to produce a suitable tool for the simulation of 3D compressible, turbulent, multispecies flows where mixing processes play a major role. As a particular application, the performance of a Dry Low NOx GTU combustor is exhaustively studied under typical operating conditions. The overall goal is subdivided into sub-objectives which ensure adequate progression when developing the algorithm. These are outlined as:

- Description of suitable physical models, mathematical formulations and numerical methods for the simulation of turbulent compressible flows with critical mixing.
- Integration of additional features into FLAMENCO to prevent instabilities generated under certain conditions (i.e. low dissipation in highly-discretised confined regions).
- Definition and validation of FLAMENCO. Combination of typical (i.e. 5^{th} WENO reconstruction, 2^{nd} Order Runge-Kutta in time) and novel (5^{th} Order TVD reconstruction, 2^{nd} Order Stable Runge-Kutta in time) methods to make the code accurate, robust, efficient and comparable to results available in literature. Extensive validation through contrasted test cases.
- Analysis of the computational efficiency of different methods and set-ups.
- Application to the Dry Low NOx GTU combustor. In-depth study of the characteristic physical structures arising. Assessment of the numerical accuracy obtained with different models through comparison with experimental data.
- Post-process of mean and turbulent profiles to determine the relationship between the characteristic parameters and flow behaviour.
- Provide accurate results to be contrasted with data obtained in the same combustor by researchers from Perm University.
- Optimisation of FLAMENCO to make it suitable for expensive simulations.

1.6 Structure of the thesis

This thesis is structured following the logical order described in the previous section. In Chapter 2, the physical and mathematical models considered are described. Firstly, the expected phenomena taking place within the Dry Low NOx GTU combustor are presented, assessing the suitability of the physical models employed to represent them. Special attention is paid to the three main vortical structures, namely the Central

Recirculation Zone, the Precessing Vortex Core and Secondary Vortices. Secondly, the 5-Equation Transport model for compressible fluids is derived and posed, analysing different closure assumptions.

Chapter 3 describes in detail all numerical methods considered in this work. Finite Volume Godunov-Type algorithms combined with High-Order High-Resolution schemes are defined in conjunction with different thermodynamic closures. Here, time integration, reconstruction of convective fluxes and discretisation of diffusive terms, thermodynamic treatment of the mixture and closure laws are addressed.

Chapter 4 is fully dedicated to the analysis and validation of the final version of FLAMENCO. Special attention is paid to the strategies followed to balance low dissipation, including modifications in boundary conditions and reconstruction schemes. The implementation and performance of three reconstruction schemes, namely 2^{nd} Order Minmod, 5^{th} Order MLP Total Variation Diminishing and 5^{th} Order WENO, are deeply investigated, presenting from accuracy tests to computational efficiency plots.

Finally, results generated by FLAMENCO on the Dry Low NOx GTU combustor are shown in Chapter 5. All stages regarding the set-up process are clearly indicated, while also highlighting possible sources of error. Then, deep analysis is performed, post-processing statistically steady and intrinsically unsteady phenomena. Chapter 6 concludes the thesis with several ideas and recommendations for future research.

Chapter 2

Physical and Mathematical models

2.1 Mixing Processes inside a Dry Low NOx GTU Combustor

The Dry Low NOx GTU Combustor is an advanced system devised to generate high-mixing rates at relatively high speeds in confined regions. For this purpose, an external swirling air flow is injected to break an internal high-velocity fuel flow, aiming to create the proper conditions within the combustion chamber so the fluid downstream the injector recirculates. As a consequence, a low-speed region where reactions may occur is developed, producing a stable flame which remains attached without being blown-off or quenched. Consequently, the events taking place within the Dry Low NOx GTU combustion chamber hold a great complexity. Indeed, the combination of turbulent compressible flows developing inside such a confined domain, high-shear regions appearing close to the fuel injector exit, highly-unsteady macroscopic vortices moving along the chamber and adverse pressure gradients, makes the analysis very complicated.

Although there are infinite processes taking place, many authors in the literature (see for example Fu et al. [9], Ahmed [10], Syred et al. [11], Valera-Medina et al. [12, 13]) agree in defining three main vortical structures whose properties characterise fairly well the whole system: Central Recirculation Zone (CRZ), Precessing Vortex Core (PVC) and Secondary Vortices. Furthermore, these authors assert in their research works that a proper description of such structures suggests accurate understanding of the mechanism. Therefore, any attempt of modeling the physics must pay special attention to them.

The CRZ is a toroidal structure developed approximately in the middle of the combustion chamber as a consequence of the adverse pressure gradients induced by the swirling flow, which due to centrifugal forces is pushed against the outer wall creating a low pressure region near the axis of rotation close to the swirl injector exit. It is responsible not only for creating low velocities that enable stable flames, but it also recycles heat and active chemical species necessary for a clean and efficient combustion. The nature of this statistically steady structure has been deeply analysed in the literature. For instance, Perisetty et al. [14] studied the formation of the CRZ in a simple unconfined

geometry with coaxially injected swirl and axial flows. In their work, they showed that size and position of the CRZ are directly related, on the one hand, to the magnitude of the tangential momentum of the swirling flow relative to its axial momentum (swirl number), and on the other hand, to the magnitude of the swirl relative to the non-swirling flow axial momentum. These authors concluded that there is a critical Swirl number which determines the existence of the CRZ. Whereas below this critical value the adverse pressure gradient is not large enough to decelerate and induce reversed velocity in the inner flow, above it the CRZ appears, defining an aerodynamic field whose size and location is fully coupled with the magnitude of the Swirl. Figure 2.1 depicts the mesh used by [14] and subcritical and supercritical cases.

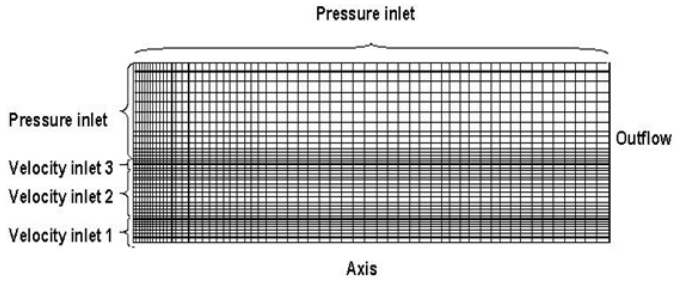

(a) Computational domain

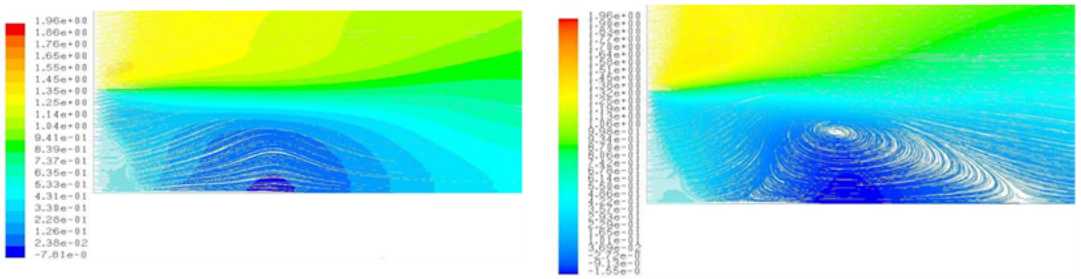

(b) Subcritical Swirl number case. CRZ does not appear

(c) Supercritical Swirl number case. CRZ appears

Figure 2.1: Coaxially injected Swirl and axial flows. Subcritical and Supercritical cases. Reproduced from [14]

The PVC is a complex three-dimensional intrinsically unsteady coherent structure located at the edge of the CRZ, extending from the swirl injector exit to the rear wall of the combustion chamber, where is broken in smaller irregular eddies. Its size and frequency increase with the flow rate and depend on the Swirl number and geometry. The PVC wraps the CRZ in a characteristic helical motion (see Figure 2.2), inducing visible perturbations in tangential velocity profiles. It is created at the lower wall of the swirl injector due to the thermodynamic fluctuations induced by the non-centred CRZ and vortex breakdown, where low pressure creates an upstream fluid motion to the interior of the duct, and contributes to increase turbulence in the high shear regions at the edge of the CRZ where high rates of mixing are found. As asserted by Syred et al. [15] and Valera-Medina et al.

[13], both CRZ and PVC structures interact in an extremely complex process (see Figure 2.3 for a schematic representation), increasing the turbulence of the whole system and creating smaller vortical structures. The potential unwanted effects of the PVC include instability enhancement and flow distortion.

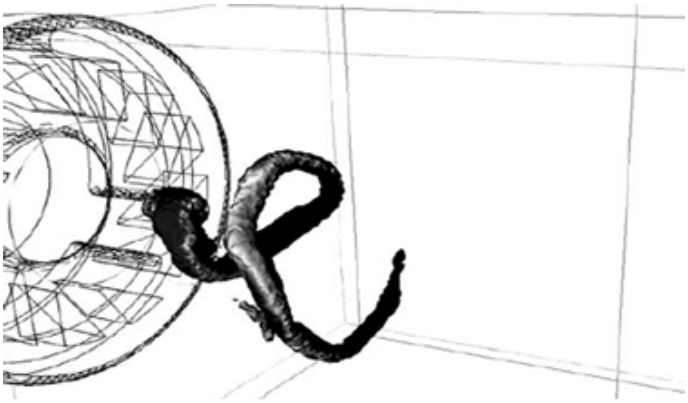

Figure 2.2: PVC helical structure originated at the swirler exit. Reproduced from Rouxa et al. [16]

The last main three-dimensional flow feature, Secondary Vortices, refers to small intrinsically unsteady structures generated right downstream the swirl injector. These eddies are mainly produced in the separation region at the edge of the swirl duct, where the swirling flow is pushed outwards due to centrifugal effects. Again, the size, distribution, frequency and intensity of these structures are highly dependent on the geometry, Swirl number and flow rate. The formation and behaviour of Secondary Vortices is a major concern in the state-of-the-art of swirl injectors, since few data are available due to their overlapped effects. Indeed, it is really difficult to isolate the perturbations they provoke, especially when they scatter around the root of the PVC. As for the moment, it is believed (see Al-Abdeli et al. [17]) that apart from affecting the behaviour of the CRZ, they also act on the formation of the PVC and the intensity of the shear layer.

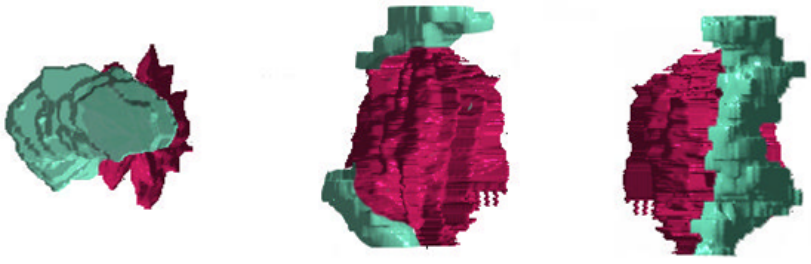

Figure 2.3: Schematic representation of the PVC-CRZ interaction. CRZ is shown in red and PVC in turquoise. Reproduced from Valera-Medina et al. [13]

There are many other phenomena taking place within the combustor, like macroscopic vortices close to the walls, the recirculation region attached to the upper corner of the

chamber, acoustic waves or heat evacuation. However, since all of them contribute to the formation of the structures above mentioned, the final configuration of these will characterise the whole problem.

In light of the above stated aerodynamic mechanisms, it remains justified that a three-dimensional, unsteady, multispecies, turbulent physical model is necessary in order to represent the problem consistently. Furthermore, the flow mixing nature of the process, where highly-stressed shear layers appear, forces the definition of a mixture model with heat and momentum dissipation. In the present study, in addition to all these considerations, compressibility is applied in order to be able to capture acoustic-related phenomena.

2.2 5-Equation Transport Model for compressible flows

A general multispecies model is required in order to perform the analysis. Although in the non-reactive mixing case under consideration only two species (air and methane as fuel coexist, a general model for N species is easily defined by setting mass, momentum and energy conservation equations for each one of them. In the Dry Low NOx GTU Combustor, non-premixed air and fuel are injected separately through coaxial ducts. Hence, the layout is effectively the same as two gas phases initially separated, with the difference that once they enter in contact, the mixture formation must be calculated. As shown later, fuel here is mathematically treated as a different species than air, but both are set with the same thermodynamic properties as air (considered as a non-reactive perfect gas). This is simply done in order to make results comparable to experiments where water was employed as both components.

The multispecies model employed here is a variation of a multifluid model with a mixture region defined. The basis of the formulation is the well known 7-Equation Multifluid Model, proposed by Baer and Nunziato [18] and tested by Saurel et al. [19] for two phases, obtained through volume fraction-averaging of the conservation equations. The extension for N species of this model is straightforward and can be expressed as

- **Mass Conservation**

$$\frac{\partial (z_k \rho_k)}{\partial t} + \nabla \cdot (z_k \rho_k \bar{v}_k) = 0 \quad k = 1, ..., N \tag{2.1}$$

- **Momentum Conservation**

$$\frac{\partial (z_k \rho_k \bar{v}_k)}{\partial t} + \nabla \cdot (z_k \rho_k \bar{v}_k \bar{v}_k) + \nabla (z_k p_k) = p_k^I \nabla z_k + \sum_{m=1}^{M} \lambda_{mk} (\bar{v}_k - \bar{v}_m) \tag{2.2}$$

$k = 1, ..., N$; *m extended to M species in contact with species k*

$p_k^I \equiv Pressure\ of\ species\ k\ at\ the\ interface$

$\lambda_{mk} \equiv Velocity\ Relaxation\ Coefficient\ relative\ to\ species\ m\ and\ k$

- **Energy Conservation**

$$\frac{\partial (z_k \rho_k E_k)}{\partial t} + \nabla \cdot (z_k \rho_k E_k \overline{v}_k) + \nabla (z_k p_k \overline{v}_k) = p_k^I \overline{v}_k^I \nabla z_k + \sum_{m=1}^{M} \lambda_{mk} \overline{v}_k^I \cdot (\overline{v}_k - \overline{v}_m) + \sum_{m=1}^{M} \mu_{mk} p_k^I (p_k - p_m) \tag{2.3}$$

$k = 1, ..., N\ ;\ m\ extended\ to\ M\ species\ in\ contact\ with\ species\ k$

$\overline{v}_k^I \equiv Velocity\ of\ species\ k\ at\ the\ interface$

$\mu_{mk} \equiv Pressure\ Relaxation\ Coefficient\ relative\ to\ species\ m\ and\ k$

- **Volume Fraction Advection**

$$\frac{\partial z_k}{\partial t} + \overline{v}_k^I \nabla z_k = \sum_{m=1}^{M} \mu_{mk} (p_k - p_m) \tag{2.4}$$

$k = 1, ..., N-1\ ;\ m\ extended\ to\ M\ species\ in\ contact\ with\ species\ k$

$$\sum_{k=1}^{N} z_k = 1$$

Where E is the total energy, z is the volume fraction and μ_{mk} is the Pressure Relaxation Coefficient relative to species m and k, also called Compaction Viscosity. Note that without any loss of generality, diffusion and source terms are not considered in the formulation. It must be said that pressure and velocity at the interface may be different from those values far from it if the phases in contact are not in instantaneous equilibrium.

The 7-Equation model as posed above is the more general form of the system that deals with multifluid environments. Therefore, it is suitable for situations where the fast perturbations altering the equilibrium at the interface are rather important. The non-equilibrium at the interface of two phases is mainly evidenced, for instance, in problems where highly perturbing phenomena propagate in two phases with different inertia. Indeed, following Baer and Nunziato [18] experiments with granular explosives, when gas and solid particles (treated as fluid with negligible compressibility) are put together and subjected to intense pressure waves, the difference in the propagation velocity creates areas where pressure (and velocity) are not in equilibrium (see the sketch in Figure 2.4). Although this situation is of course transient, with the system evolving towards equilibrium conditions, the effects of such relaxation process on the thermodynamic properties are not negligible at all, making the consideration of all terms in system (2.1)-(2.4) necessary for an accurate modelisation.

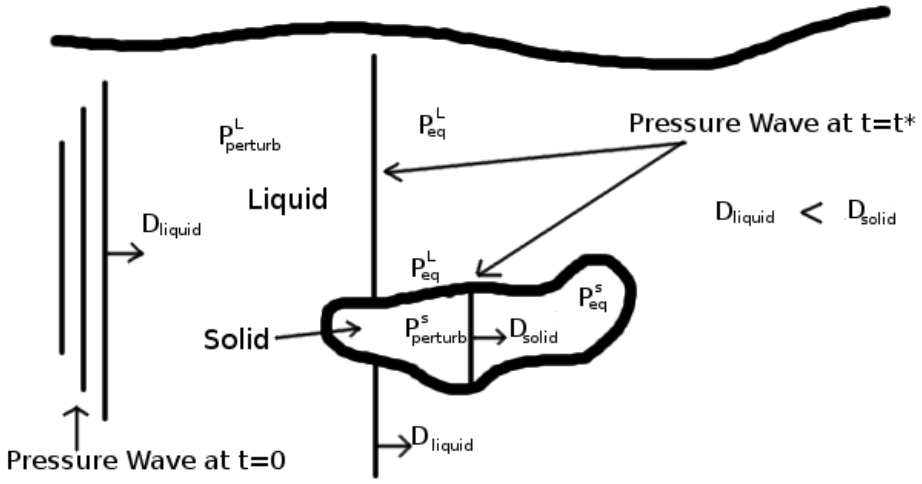

Figure 2.4: Non-equilibrium condition at t=t*. P^S_{eq} and P^L_{eq} are the pressure of the solid and liquid in equilibrium respectively. $P^S_{perturb}$ and $P^L_{perturb}$ are the pressure of the solid and liquid after the perturbation

For problems where the intensity of the transient perturbations or the disparity in the inertia associated with the fluids is not critically large, an assumption of quasi-equilibrium is completely reasonable. As mentioned, the velocity relaxation coefficient, λ, and the pressure relaxation coefficient or compaction viscosity, μ, are two parameters that measure how strongly the system opposes to be perturbed. In this way, high values of λ and μ represent a stiff system where equilibrium in velocity and pressure respectively is rapidly achieved, $\varepsilon \to 0$ (ε relaxation time). In the limit $\lambda \to \infty$, $\mu \to \infty$, equilibrium at the interface is instantaneously recovered, $\overline{v}_{k_1} = \overline{v}_{k_2}$, $p_{k_1} = p_{k_2}$ at the interface, cancelling out the last terms in equations (2.2), (2.3) and (2.4). It should be said that making $\lambda \to \infty$ implies, among other effects, the inability of taking into account drag forces, so it is only suitable for problems where both phases move with the same velocities at the contact surface (i.e. gas bubbles embedded in a liquid medium, etc.).

Since the present work and related tools are intended to deal with problems falling within the limits defined by the quasi-equilibrium condition, it seems reasonable to adopt such simplification. After some algebraic manipulations, the 7-Equation Multifluid Model is transformed into the 5-Equation Reduced Model, as presented by Murrone et al. [20]. From this system, Allaire et al. [21] obtained the 5-Equation Transport Model straightforwardly for initially separated multiphase flows, as

- **Mass Conservation**

$$\frac{\partial (z_k \rho_k)}{\partial t} + \nabla \cdot (z_k \rho_k \overline{v}_k) = 0 \quad k = 1, ..., N \tag{2.5}$$

- **Momentum Conservation**

$$\frac{\partial(\rho\overline{v})}{\partial t} + \nabla\cdot(\rho\overline{v}\overline{v}) + \nabla p = 0 \tag{2.6}$$

- **Energy Conservation**

$$\frac{\partial(\rho E)}{\partial t} + \nabla\cdot(\rho E\overline{v}) + \nabla(p\overline{v}) = 0 \tag{2.7}$$

- **Volume Fraction Advection**

$$\frac{\partial z_k}{\partial t} + \overline{v}\cdot\nabla z_k = 0 \quad ; \quad k = 1,...,N-1 \tag{2.8}$$

$$\sum_{k=1}^{N} z_k = 1 \tag{2.9}$$

where E, ρ, $\overline{v}$ and p are Total Energy, density, velocity and pressure at each point of the fluid domain, respectively. Note that these values may refer either to a pure fluid or to the mixture. This 5-Equation Transport Model for Compressible Flows represents the underlying mathematical method of the present work. For all derivations regarding this model, the reader is referred to Appendix A.

2.3 Mixture model

According to results shown in Appendix A, the transference from the 7-Equation Multifluid Model to the 5-Equation Transport Model has an essential consequence: the capacity to deal with mixtures is suppressed. Indeed, as mentioned above, a necessary assumption to derive the 5-Equation Transport Model is to consider only one fluid at a given point in time and space. Mathematically speaking, this issue would of course limit the applicability of the model to immiscible fluids. However, numerically, the result is completely different. When the transport equation (2.8) is solved numerically without any interface sharpening or interface reconstruction method (which are actually necessary if physically immiscible fluids are addressed), numerical diffusion appears, introducing a similar effect to that produced by physical diffusion. As a consequence, small regions where different phases coexist at a given point in space and time develop, leading to a multispecies-like behaviour. As an example, let consider the numerical discretisation of

(2.8) in 1D using a simple Explicit Euler scheme in time, first order downwind in space

$$\frac{z_k^{n+1}\big|_i - z_k^n\big|_i}{\Delta t} + v_i^n \frac{z_k^n\big|_i - z_k^n\big|_{i-1}}{\Delta x} = \underbrace{o(\Delta t) + o(\Delta x)}_{\substack{Numerical\ Error \\ = \\ Numerical\ Diffusion}} \tag{2.10}$$

Now considered a 1D interface moving at speed v and

$$t = 0 \quad \begin{cases} z_k = 0 & x > 0 \\ z_k = 1 & x \leq 0 \end{cases} \rightarrow \begin{matrix} z_k^0\big|_i = 0 & i > 0 \\ z_k^0\big|_i = 1 & i \leq 0 \end{matrix} \quad ; \; x_0 = 0 \tag{2.11}$$

If, for example, the interface moves one grid point per time step, the exact mathematical result is

$$\begin{matrix} z_k^1\big|_i = 0 & i > 1 \\ z_k^1\big|_i = 1 & i \leq 1 \end{matrix} \quad ; \quad z_k^1\big|_1 = 1 \tag{2.12}$$

but the numerical result is

$$z_k^1\big|_i = z_k^0\big|_i - \frac{\Delta t}{\Delta x} v_i^0 \left(z_k^0\big|_i - z_k^0\big|_{i-1} \right) \rightarrow z_k^1\big|_1 = z_k^0\big|_1 - \frac{\Delta t}{\Delta x} v_1^0 \left(z_k^0\big|_1 - z_k^0\big|_0 \right) = \frac{\Delta t}{\Delta x} v_1^0 < 1 \tag{2.13}$$

Since

$$z_k^1\big|_1^{Physical} = 1 = z_k^1\big|_1^{Numerical} + o(\Delta t) + o(\Delta x) = \frac{\Delta t}{\Delta x} v_1^0 + o(\Delta t) + o(\Delta x) \tag{2.14}$$

In light of this result, it is clear that at $t = \Delta t$ the interface has been smeared at x_1, since this position, which was supposed to be fully occupied by one phase ($z_k^1\big|_1^{Physical} = 1$), is actually filled with two or more phases ($z_k^1\big|_1^{Numerical} = \frac{\Delta t}{\Delta x} v_1^0 \; ; \sum z_{m \neq k}^1 \Big|_1^{Numerical} = 1 - \frac{\Delta t}{\Delta x} v_1^0$). To deal with this situation, a mixture model must be defined to represent mathematically those regions where several species are present.

The mathematical definition of the mixture model used in the present work is that proposed by Allaire et al. [21]. In their study, they define the mixture as a weighted composition where the weights are volume fractions, as shown in system (2.15). Note that following results given by Allaire et al. [21] and validated in Aguado [8], the isobaric closure (all partial pressures are equal between them and equal to the mixture pressure) is employed here to produce results free of spurious oscillations. Indeed, since it is the volume fraction averaging of either partial pressures, temperatures or densities to compose a mixture value which creates overshoots, and provided that the isobaric closure does not require this sort of averaging, the problem is mathematically and numerically overcome (it can easily be seen that if the isothermal closure is utilised instead, Dalton's Law for pressure is necessary, forcing the volume averaging of this quantity). Finally, it

must be mentioned that since the relevant thermodynamic variables are those representing the mixture, this mathematical artifice does not have different physical implications from those yielded by the isothermal closure.

$$
\begin{aligned}
& z_k = \tfrac{V_k}{V_{mixt.}} && Y_k = \tfrac{z_k \rho_k}{\rho_{mixt.}} \\
& \rho_{mix.} = \sum_{k=1}^{N_{species}} z_k \rho_k \\
& \rho_{mix.} \varepsilon_{mix.} = \sum_{k=1}^{N_{species}} z_k \rho_k \varepsilon_k && \rho_{mix.} h_{mix.} = \sum_{k=1}^{N_{species}} z_k \rho_k h_k \\
& \varepsilon_k = EOS(p_k, \rho_k) && \varepsilon_k = c_{v_k}(T_k)\, T_k \\
& R_{mix.} = \sum_{k=1}^{N_{species}} R_k Y_k \\
& \gamma_{mix.} = 1 + \tfrac{1}{\sum_{k=1}^{N.Spcs} \frac{z_i}{\gamma_k - 1}} && \gamma_k = 1 + \tfrac{R_k}{C_{v_k}} \\
& p_{mix.} = p_k \\
& T_{mix.} = \tfrac{\varepsilon_{mix.}}{C_{v_{mix,}}} && C_{v_{mix,}} = \tfrac{R_{mix.}}{\gamma_{mix.} - 1}
\end{aligned}
\tag{2.15}
$$

In terms of a closed mathematical problem, it is clear that system (2.5)-(2.9) together with equations (2.15) define a well-posed formulation. In this way, variables $z_k \rho_k$ and z_k for all species, $\rho_{mix.} \overline{v}$ and $\rho_{mix.} E$ from (2.5)-(2.9) can be used to compute first the mixture density, then the internal energy as

$$
\rho_{mix.} \varepsilon_{mix.} = \rho_{mix.} E - \frac{1}{2} \frac{(\rho_{mix.} \overline{v} \cdot \rho_{mix.} \overline{v})}{\rho_{mix.}} \tag{2.16}
$$

and finally $p_{mix.}$, $R_{mix.}$, $\gamma_{mix.}$ and $T_{mix.}$. From now onwards, the subscript "mix." is suppressed for simplicity, writing the variable alone when referring to the mixture and with the appropriate subscript when referring to a given species.

Chapter 3

Numerical Methods

3.1 Unsplit Finite Volume Godunov-Type Methods

The mathematical model proposed in the previous chapter must be resolved with a suitable numerical algorithm. For compressible flows where acoustic phenomena may have relevant influence on the unsteady development of physical structures, Finite-Volume formulations have shown to perform really well, preserving the characteristic conserved variables, holding pressure waves throughout the domain and facilitating the imposition of boundary conditions. As for the numerical scheme, although Unsplit Godunov-Type methods in curvilinear grids are documented in the literature as very accurate, structured algorithms for unsteady flows (see for example Brown [22], Kreiss [23]), their numerical definition is rather complex. However, by using suitable curvilinear transformations, as is the case in the present work, the formulation can be simplified to generate a model numerically affordable (see Thomas and Lombard [24] and Aguado [8] for the transformation applied in FLAMENCO). Therefore, in this study an Unsplit Finite-Volume Godunov method is employed as the baseline scheme.

For simplicity, a detailed analysis of the properties and behaviour of this approach is omitted here. However, exhaustive rationales are undertaken in Toro [25], Godunov [26], Zabrodine [27] or LeVeque [28]. The exact underlying formulation implemented in FLAMENCO is described in [8] extensively, so here only final discretisations are written.

The Unsplit Finite Volume Godunov-Type scheme with curvilinear transformations implemented in FLAMENCO reads

$$\overline{U}^{n+1}_{i,j,k} = \overline{U}^{n}_{i,j,k} + \frac{\Delta t}{\Delta \xi}(\overline{F}^{n}_{i-\frac{1}{2},j,k} - \overline{F}^{n}_{i+\frac{1}{2},j,k}) + \frac{\Delta t}{\Delta \eta}(\overline{G}^{n}_{i,j-\frac{1}{2},k} - \overline{G}^{n}_{i,j+\frac{1}{2},k}) + \frac{\Delta t}{\Delta \zeta}(\overline{H}^{n}_{i,j,k-\frac{1}{2}} - \overline{H}^{n}_{i,j,k+\frac{1}{2}}) \quad (3.1)$$

where $\overline{F}$, $\overline{G}$ and $\overline{H}$ are the 3D fluxes in each independent direction and $\overline{U}$ is the vector of conserved variables. Note that here ξ, η and ζ are transformed variables in the Cartesian space (curvilinear x, y, z $\rightarrow$ Cartesian ξ, η, ζ). This is the most basic form of the discretisation, and is the base for more sophisticated integrations in time. Finally, it must be said that turbulence, which is an essential feature of the Dry Low NOx GTU combustor problem, is accounted using Implicit Large-Eddie Simulation. Again, complete definition of this approach is presented in [8].

3D fluxes $\overline{F}$, $\overline{G}$ and $\overline{H}$ account for inviscid, viscous and heat fluxes through cell faces associated with ξ, η and ζ directions respectively,

$$\begin{aligned} \overline{F} &= \overline{F}^{Inviscid} + \overline{F}^{Viscous} + \overline{F}^{Heat} \\ \overline{G} &= \overline{G}^{Inviscid} + \overline{G}^{Viscous} + G^{Heat} \\ \overline{H} &= \overline{H}^{Inviscid} + \overline{H}^{Viscous} + \overline{H}^{Heat} \end{aligned} \tag{3.2}$$

which must be obtained using different methods. The explicit advection used in FLAMENCO allows decoupling the operators in equation (3.2), basing the calculation of each flux in the available solution vector obtained in the previous time step. This way of proceeding has been extensively tested in Shimada et al. [29] and Thornber et al. [30] yielding precise results.

3.1.1 Convective Fluxes

The finite volume discretisation selected requires numerical fluxes at cell interfaces. In order to obtain these fluxes, additional hypothesis must be incorporated regarding the way physical properties distribute along the flow field. Since finite volume methods discretise the physical domain into a finite number of cells, storing numerical values at each cell centre, it is necessary to have suitable models in order to reconstruct the whole flow field in a continuous fashion. For this purpose, the existence of discontinuities in the fluid may or may not be presumed, leading to different perspectives in the treatment of the problem. If no discontinuities are considered, viscous terms balance the convective ones in regions subjected to high gradients, enabling the thermodynamic state reconstruction at any point of the domain from simple (or complex) averaging of the neighbouring cells. Within this framework, which is broadly used for incompressible fluids, the accuracy of the reconstruction will of course depend on the order of the numerical scheme. On the other hand, if discontinuities are allowed, it is implicitly assumed that they appear because the viscous terms are not able to balance the convective ones in regions where high gradients develop. In this case the reconstruction is more complex because it must be assumed that discontinuities may exist at any point, forcing the resolution of a discontinuous problem at every point in space, namely a Local Riemann Problem (see [25]). From a physical point of view, this approach is suitable for highly compressible flows, especially when shock waves are dominant flow phenomena.

Inside the Dry Low NOx GTU combustor the characteristic velocities are below the speed of sound (M$\sim$0.2) and thus no relevant discontinuities are expected. However, as mentioned in Section 2.1, the coupling between turbulence and acoustic perturbations, although weak, is not negligible at all. Therefore, in order not only to predict such interactions, but also to be able to define coarse grids in the thin viscous layers where thermodynamic properties change in a continuous way, a compressible model is chosen for FLAMENCO.

The general form of the inviscid fluxes can be expressed as

$$\begin{aligned}
\overline{F}^{Inviscid}_{i+\frac{1}{2},j,k} &= \overline{F}^{Inviscid}_{i+\frac{1}{2},j,k}\left(\overline{U}_{i+\frac{1}{2},j,k}\right) \\
\overline{G}^{Inviscid}_{i+\frac{1}{2},j,k} &= \overline{G}^{Inviscid}_{i+\frac{1}{2},j,k}\left(\overline{U}_{i+\frac{1}{2},j,k}\right) \\
\overline{H}^{Inviscid}_{i+\frac{1}{2},j,k} &= \overline{H}^{Inviscid}_{i+\frac{1}{2},j,k}\left(\overline{U}_{i+\frac{1}{2},j,k}\right)
\end{aligned} \tag{3.3}$$

for the interface $i+\frac{1}{2},j,k$. Firstly, the vector of conserved variables must be obtained at the cell interface as a function of the reconstructed left and right states $\overline{U}_L$, $\overline{U}_R$ by solving the Local Riemann Problem posed at the cell interface

$$\overline{U}_{i+\frac{1}{2},j,k} = \textit{Local Riemann Problem}\left(\overline{U}_L, \overline{U}_R\right) \tag{3.4}$$

where $\overline{U}_L$, $\overline{U}_R$ depend on the reconstruction scheme (see Section 3.2). In the Local Riemann Problem sketched in Figure 3.1 five characteristic speeds (eigenvalues of the system) appear, namely $\lambda_1 = u-a$, $\lambda_2 = \lambda_3 = \lambda_4 = u$, $\lambda_5 = u+a$, with u the flow velocity and a the speed of sound. As a consequence, three waves with different characteristic velocities (left, contact and right waves) propagate from the cell interface.

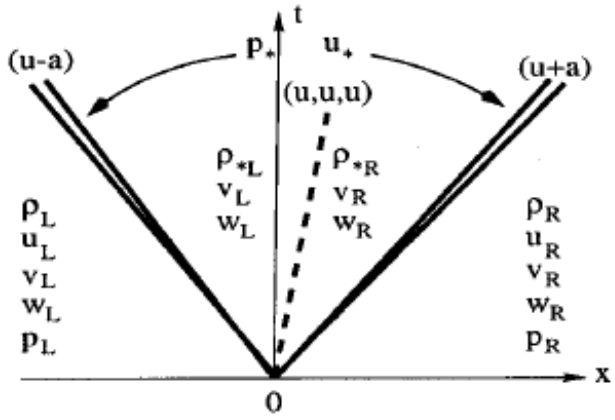

Figure 3.1: Local Riemann Problem. Reproduced from [25].

Assuming that the unitary normal vector to the cell interface is of the form $\overrightarrow{n} = \left(n_\xi, n_\eta, n_\zeta\right)$ and that Hugoniot formula (3.5) holds true through discontinuities

$$\overline{F}\left(\overline{U}_2\right) - \overline{F}\left(\overline{U}_1\right) = S\left(\overline{U}_2 - \overline{U}_1\right) \tag{3.5}$$

with states 2 and 1 referring to "after" and "before" the jump and S the velocity of the

discontinuity, the state $\overline{U}_{i+\frac{1}{2},j,k}$ at the interface can be expressed, for multispecies, as

$$\overline{U}_{i+\frac{1}{2},j,k} = \begin{cases} \overline{U}_L & if\ S_L > 0 \\ \overline{U}_L^* & if\ S_L \leqslant 0 < S_* \\ \overline{U}_R^* & if\ S_* \leqslant 0 < S_R \\ \overline{U}_R & if\ S_R < 0 \end{cases} \tag{3.6}$$

where S_L, S_* and S_R are the speeds of the left, contact and right waves respectively.and

$$\overline{U}_p = \begin{pmatrix} (z_1\rho_1)_p \\ \vdots \\ (z_N\rho_N)_p \\ (\rho u)_p \\ (\rho v)_p \\ (\rho w)_p \\ e_p \end{pmatrix} \ ; \ \overline{U}_p^* = \begin{pmatrix} (z_1\rho_1)_p^* \\ \vdots \\ (z_N\rho_N)_p^* \\ (\rho u)_p^* \\ (\rho v)_p^* \\ (\rho w)_p^* \\ e_k^* \end{pmatrix} = \frac{1}{S_p - S_*} \begin{pmatrix} \rho_k \left(S_p - V_p^\perp\right) \\ \rho u_p \left(S_p - V_p^\perp\right) + (p^* - p_p) n_\xi \\ \rho v_p \left(S_p - V_p^\perp\right) + (p^* - p_p) n_\eta \\ \rho w_p \left(S_p - V_p^\perp\right) + (p^* - p_p) n_\zeta \\ e_p \left(S_p - V_p^\perp\right) + p^* S_p - p_p V_p^\perp \end{pmatrix}$$

$$p = L, R \tag{3.7}$$

are the states at the interface for subsonic flows. Note that in eq. (3.7) the velocity perpendicular to the interface is

$$V_p^\perp = \overline{v}_p \cdot \overrightarrow{n} = u_p n_\xi + v_p n_\eta + w_p n_\zeta \ \ ; \ \ p = L, R \tag{3.8}$$

and the values of S_L, S_R are given in Einfeldt [31, 32]. As for the velocity at the interface, it can be written as

$$S_* = \frac{\rho_R V_R^\perp \left(S_R - V_R^\perp\right) - \rho_L V_L^\perp \left(S_L - V_L^\perp\right) + p_L - p_R}{\rho_R \left(S_R - V_R^\perp\right) - \rho_L \left(S_L - V_L^\perp\right)} \tag{3.9}$$

as defined in Batten et al. [33], and pressure at the interface

$$p^* = \rho_L \left(V_L^\perp - S_L\right)\left(V_L^\perp - S_*\right) + p_L = \rho_R \left(V_R^\perp - S_R\right)\left(V_R^\perp - S_*\right) + p_R \tag{3.10}$$

For a Step-by-Step derivation of above formulas the reader is referred to Drikakis [34]. In the present work, the HLLC approximate flux from Toro [25] is employed. Without any loss of generality, such flux can be described as

$$\bar{F}_{i+\frac{1}{2},j,k}^{HLLC} = \begin{cases} \overline{F}_L & if\ S_L > 0 \\ \overline{F}_{*L} & if\ S_L \leqslant 0 < S_* \\ \overline{F}_{*R} & if\ S_* \leqslant 0 < S_R \\ \overline{F}_R & if\ S_R < 0 \end{cases} \tag{3.11}$$

with

$$\overline{F}_p = \begin{pmatrix} (z_1\rho_1)_p V_p^{\perp} \\ \vdots \\ (z_N\rho_N)_p V_p^{\perp} \\ (\rho u)_p V_p^{\perp} + p_p n_\xi \\ (\rho v)_p V_p^{\perp} + p_p n_\eta \\ (\rho w)_p V_p^{\perp} + p_p n_\zeta \\ (e_p + p_p) V_p^{\perp} \end{pmatrix} \; ; \; \overline{F}_p^* = \begin{pmatrix} (z_1\rho_1)_p^* S_* \\ \vdots \\ (z_N\rho_N)_p^* S_* \\ (\rho u)_p^* S_* + p^* n_\xi \\ (\rho v)_p^* S_* + p^* n_\eta \\ (\rho w)_p^* S_* + p^* n_\zeta \\ \left(\rho_p^* + p^*\right) S_* \end{pmatrix} \quad p = L, R \tag{3.12}$$

Finally, the flux must be rescaled according to the curvilinear transformation in the form

$$\overline{F}^{Inviscid}_{i+\frac{1}{2},j,k} = \bar{F}^{HLLC}_{i+\frac{1}{2},j,k} \beta_{i+\frac{1}{2},j,k} \tag{3.13}$$

where $\beta_{i+\frac{1}{2},j,k}$ is the Face Jacobian of the cell interface $i+\frac{1}{2}, j, k$ yielded by

$$\beta_{i+\frac{1}{2},j,k} = \sqrt{\left(\frac{\partial y}{\partial \eta}\frac{\partial z}{\partial \zeta}\Big|_{i+\frac{1}{2},j,k} - \frac{\partial y}{\partial \zeta}\frac{\partial z}{\partial \eta}\Big|_{i+\frac{1}{2},j,k} \right)^2 + \left(\frac{\partial x}{\partial \zeta}\frac{\partial z}{\partial \eta}\Big|_{i+\frac{1}{2},j,k} - \frac{\partial x}{\partial \eta}\frac{\partial z}{\partial \zeta}\Big|_{i+\frac{1}{2},j,k} \right)^2 + \left(\frac{\partial x}{\partial \eta}\frac{\partial y}{\partial \zeta}\Big|_{i+\frac{1}{2},j,k} - \frac{\partial x}{\partial \zeta}\frac{\partial y}{\partial \eta}\Big|_{i+\frac{1}{2},j,k} \right)^2} \tag{3.14}$$

Note that interface normal vector components are

$$\begin{aligned} n_\xi\big|_{i+\frac{1}{2},j,k} &= \frac{\frac{\partial y}{\partial \eta}\frac{\partial z}{\partial \zeta}\Big|_{i+\frac{1}{2},j,k} - \frac{\partial y}{\partial \zeta}\frac{\partial z}{\partial \eta}\Big|_{i+\frac{1}{2},j,k}}{\beta_{i+\frac{1}{2},j,k}} \\ n_\eta\big|_{i+\frac{1}{2},j,k} &= \frac{\frac{\partial x}{\partial \zeta}\frac{\partial z}{\partial \eta}\Big|_{i+\frac{1}{2},j,k} - \frac{\partial x}{\partial \eta}\frac{\partial z}{\partial \zeta}\Big|_{i+\frac{1}{2},j,k}}{\beta_{i+\frac{1}{2},j,k}} \\ n_\zeta\big|_{i+\frac{1}{2},j,k} &= \frac{\frac{\partial x}{\partial \eta}\frac{\partial y}{\partial \zeta}\Big|_{i+\frac{1}{2},j,k} - \frac{\partial x}{\partial \zeta}\frac{\partial y}{\partial \eta}\Big|_{i+\frac{1}{2},j,k}}{\beta_{i+\frac{1}{2},j,k}} \end{aligned} \tag{3.15}$$

3.1.2 Diffusion Terms

The calculation of diffusion terms in FLAMENCO is decoupled from the computation of inviscid fluxes, basing their values on the last available state. The general expression for these fluxes is

$$\begin{aligned} \overline{F}^{Diffusion} &= \overline{F}^{Viscous} + \overline{F}^{Heat} \\ \overline{G}^{Diffusion} &= \overline{G}^{Viscous} + \overline{G}^{Heat} \\ \overline{H}^{Diffusion} &= \overline{H}^{Viscous} + \overline{H}^{Heat} \end{aligned} \tag{3.16}$$

Focusing on the diffusive flux in the first independent direction, $\overline{F}^{Diffusion}$, the viscous flux at cell interface $i+\frac{1}{2},j,k$ is defined as

$$\overline{F}^{Viscous}_{i+\frac{1}{2},j,k} = \beta_{i+\frac{1}{2},j,k} \begin{pmatrix} N \begin{cases} 0 \\ 0 \\ \vdots \\ 0 \end{cases} \\ n_\xi \tau_{11} + n_\eta \tau_{12} + n_\zeta \tau_{13} \\ n_\xi \tau_{21} + n_\eta \tau_{22} + n_\zeta \tau_{23} \\ n_\xi \tau_{31} + n_\eta \tau_{32} + n_\zeta \tau_{33} \\ n_\xi \left(\overline{u}\cdot\overline{\overline{\tau}}\right)\big|_1 + n_\eta \left(\overline{u}\cdot\overline{\overline{\tau}}\right)\big|_2 + n_\zeta \left(\overline{u}\cdot\overline{\overline{\tau}}\right)\big|_3 \end{pmatrix}_{i+\frac{1}{2},j,k} \tag{3.17}$$

where $\beta_{i+\frac{1}{2},j,k}$ is shown in (3.14) and $\overline{\overline{\tau}}$ is the viscous stress tensor given by

$$\overline{\overline{\tau}} = \begin{pmatrix} \tau_{11} & \tau_{12} & \tau_{13} \\ \tau_{21} & \tau_{22} & \tau_{23} \\ \tau_{31} & \tau_{32} & \tau_{33} \end{pmatrix} =$$

$$= \mu \begin{pmatrix} -\frac{2}{3}\left(\frac{\partial v}{\partial y}+\frac{\partial w}{\partial z}\right)+\frac{4}{3}\frac{\partial u}{\partial x} & \frac{\partial u}{\partial y}+\frac{\partial v}{\partial x} & \frac{\partial u}{\partial z}+\frac{\partial w}{\partial x} \\ \frac{\partial u}{\partial y}+\frac{\partial v}{\partial x} & -\frac{2}{3}\left(\frac{\partial u}{\partial x}+\frac{\partial w}{\partial z}\right)+\frac{4}{3}\frac{\partial v}{\partial y} & \frac{\partial v}{\partial z}+\frac{\partial w}{\partial y} \\ \frac{\partial u}{\partial z}+\frac{\partial w}{\partial x} & \frac{\partial v}{\partial z}+\frac{\partial w}{\partial y} & -\frac{2}{3}\left(\frac{\partial u}{\partial x}+\frac{\partial v}{\partial y}\right)+\frac{4}{3}\frac{\partial w}{\partial z} \end{pmatrix} \tag{3.18}$$

Velocity derivatives in the curvilinear space x, y , z are transformed into the Cartesian domain using

$$\begin{pmatrix} \frac{\partial u}{\partial x} & \frac{\partial u}{\partial y} & \frac{\partial u}{\partial z} \\ \frac{\partial v}{\partial x} & \frac{\partial v}{\partial y} & \frac{\partial v}{\partial z} \\ \frac{\partial w}{\partial x} & \frac{\partial w}{\partial y} & \frac{\partial w}{\partial z} \end{pmatrix} = \begin{pmatrix} \frac{\partial u}{\partial \xi} & \frac{\partial u}{\partial \eta} & \frac{\partial u}{\partial \zeta} \\ \frac{\partial v}{\partial \xi} & \frac{\partial v}{\partial \eta} & \frac{\partial v}{\partial \zeta} \\ \frac{\partial w}{\partial \xi} & \frac{\partial w}{\partial \eta} & \frac{\partial w}{\partial \zeta} \end{pmatrix} \overline{\overline{J}}^{-1} \tag{3.19}$$

$$\overline{\overline{J}}^{-1} = \frac{\begin{pmatrix} \frac{\partial y}{\partial \eta}\frac{\partial z}{\partial \zeta}-\frac{\partial y}{\partial \zeta}\frac{\partial z}{\partial \eta} & -\left(\frac{\partial x}{\partial \eta}\frac{\partial z}{\partial \zeta}-\frac{\partial x}{\partial \zeta}\frac{\partial z}{\partial \eta}\right) & \frac{\partial x}{\partial \eta}\frac{\partial y}{\partial \zeta}-\frac{\partial x}{\partial \zeta}\frac{\partial y}{\partial \eta} \\ -\left(\frac{\partial y}{\partial \xi}\frac{\partial z}{\partial \zeta}-\frac{\partial y}{\partial \zeta}\frac{\partial z}{\partial \xi}\right) & \frac{\partial x}{\partial \xi}\frac{\partial z}{\partial \zeta}-\frac{\partial x}{\partial \zeta}\frac{\partial z}{\partial \xi} & -\left(\frac{\partial x}{\partial \xi}\frac{\partial y}{\partial \zeta}-\frac{\partial x}{\partial \zeta}\frac{\partial y}{\partial \xi}\right) \\ \frac{\partial y}{\partial \xi}\frac{\partial z}{\partial \eta}-\frac{\partial y}{\partial \eta}\frac{\partial z}{\partial \xi} & -\left(\frac{\partial x}{\partial \xi}\frac{\partial z}{\partial \eta}-\frac{\partial x}{\partial \eta}\frac{\partial z}{\partial \xi}\right) & \frac{\partial x}{\partial \xi}\frac{\partial y}{\partial \eta}-\frac{\partial x}{\partial \eta}\frac{\partial y}{\partial \xi} \end{pmatrix}}{Jac^{-1}} \tag{3.20}$$

with the Jacobian at the cell face

$$Jac = \frac{1}{Jac^{-1}} = \frac{\partial x}{\partial \xi}\left(\frac{\partial y}{\partial \eta}\frac{\partial z}{\partial \zeta}-\frac{\partial y}{\partial \zeta}\frac{\partial z}{\partial \eta}\right)+\frac{\partial x}{\partial \eta}\left(\frac{\partial y}{\partial \zeta}\frac{\partial z}{\partial \xi}-\frac{\partial y}{\partial \xi}\frac{\partial z}{\partial \zeta}\right)+\frac{\partial x}{\partial \zeta}\left(\frac{\partial y}{\partial \xi}\frac{\partial z}{\partial \eta}-\frac{\partial y}{\partial \eta}\frac{\partial z}{\partial \xi}\right) \tag{3.21}$$

The discretisation scheme used in FLAMENCO is a 2^{nd} Order Central Differences, broadly used in the industry and reported to be very accurate and stable. In this way,

a general variable ϕ can be discretised at cell interface $i+\frac{1}{2}, j, k$ as

$$\begin{aligned}
\left.\frac{\partial \phi}{\partial \xi}\right|_{i+\frac{1}{2},j,k} &= \frac{\phi_{i+1,j,k}-\phi_{i,j,k}}{\Delta\xi} \\
\left.\frac{\partial \phi}{\partial \eta}\right|_{i+\frac{1}{2},j,k} &= \frac{\frac{(\phi_{i+1,j+1,k}+\phi_{i,j+1,k})}{2} - \frac{(\phi_{i+1,j-1,k}+\phi_{i,j-1,k})}{2}}{2\Delta\eta} \\
\left.\frac{\partial \phi}{\partial \zeta}\right|_{i+\frac{1}{2},j,k} &= \frac{\frac{(\phi_{i+1,j,k+1}+\phi_{i,j,k+1})}{2} - \frac{(\phi_{i+1,j,k-1}+\phi_{i,j,k-1})}{2}}{2\Delta\zeta}
\end{aligned} \tag{3.22}$$

Finally, viscous heat dissipation is obtained through

$$\begin{aligned}
(\overline{u}\cdot\overline{\overline{\tau}})\big|_1 &= u\tau_{11}+v\tau_{12}+w\tau_{13} \\
(\overline{u}\cdot\overline{\overline{\tau}})\big|_2 &= u\tau_{21}+v\tau_{22}+w\tau_{23} \\
(\overline{u}\cdot\overline{\overline{\tau}})\big|_3 &= u\tau_{31}+v\tau_{32}+w\tau_{33}
\end{aligned} \tag{3.23}$$

Heat diffusivity follows the same structure as viscous fluxes. In this case, it can be expressed as

$$\overline{F}^{Heat}_{i+\frac{1}{2},j,k} = \beta_{i+\frac{1}{2},j,k} \begin{pmatrix} & \left.\begin{matrix}0\\0\\\vdots\\0\end{matrix}\right\} N \\ & \left.\begin{matrix}0\\0\\0\end{matrix}\right\} Momentum \\ n_\xi q_1 + n_\eta q_2 + n_\zeta q_3 & \end{pmatrix}_{i+\frac{1}{2},j,k} \tag{3.24}$$

$$\begin{aligned}
q_1 &= K\cdot\frac{\partial T}{\partial x} \\
q_2 &= K\cdot\frac{\partial T}{\partial y} \\
q_3 &= K\cdot\frac{\partial T}{\partial z}
\end{aligned} \tag{3.25}$$

with $\frac{\partial T}{\partial x}$, $\frac{\partial T}{\partial y}$, $\frac{\partial T}{\partial z}$ obtained through substitution, for example, of T for u in (3.19).

3.1.3 Volume Fraction Advection

The last equation in system (2.5)-(2.8), volume fraction advection, cannot be expressed in conservative form. However, following suggestions from [21], it is possible to rewrite (2.8) as

$$\frac{\partial z_k}{\partial t} + \overline{v}\cdot\nabla z_k = \frac{\partial z_k}{\partial t} + \nabla\cdot(z_k\overline{v}) - z_k\nabla\cdot\overline{v} = 0 \quad ; \quad k = 1,...,N-1 \tag{3.26}$$

Now, equation (3.26) admits segregation into a convective term $\nabla \cdot (z_k \overline{v})$ and a dissipation term $z_k \nabla \cdot \overline{v}$. On the one hand, the convective term can be calculated by means of a Local Riemann Problem similarly to convective fluxes in (3.13). On the other hand, the dissipation term $z_k \nabla \cdot \overline{v}$ can be averaged and computed taking into account velocities derived from the Local Riemann Problem. Following these guidelines, the Volume Fraction equation integrated in time as

$$z_k|_{i,j,k}^{n+1} = TI\left(F\left(z_k|_{i,j,k}^{n}\right)\right) \tag{3.27}$$

can be expressed without any loss of generality, for the first independent direction, ξ, as

$$F\left(z_k|_{i,j,k}^{n}\right) = \left(z_k|_{i+\frac{1}{2},j,k}^{n} - z_k|_{i,j,k}^{n}\right) S_*|_{i+\frac{1}{2},j,k}^{n} \beta|_{i+\frac{1}{2},j,k} - \left(z_k|_{i-\frac{1}{2},j,k}^{n} - z_k|_{i,j,k}^{n}\right) S_*|_{i-\frac{1}{2},j,k}^{n} \beta|_{i-\frac{1}{2},j,k} \tag{3.28}$$

where TI stands for the time integration scheme, S_* is the velocity normal to the wall given in (3.9) and $\beta|_{i+\frac{1}{2},j,k}$ is the interface Jacobian provided by (3.14). Note that this scheme is of the order of the reconstruction method employed. As it will be discussed subsequently, the main drawback of this mathematical and numerical description is the restrictive stability in time.

3.1.4 Integration in time

The time integration stage is crucial not only because of the accuracy, but also because of the stability of the numerics. Although misbehaviour of unstable schemes is often easily detected (computation crashes, sporadic peaks in numerical variables, unphysical phenomena, etc.), it is not always like that. In this way, situations where uncontrolled but bounded (or masked) instabilities arise are a major concern in CFD. The only way of producing reliable results is to select a time integration scheme that ensures an accurate and fully stable performance. Following this idea, FLAMENCO is equipped with Explicit 2^{nd} Order Runge-Kutta and Explicit 2^{nd} Order 4-Stages Runge-Kutta schemes.

The general form of both explicit time integration schemes is

$$\overline{U}|_{i,j,k}^{n+1} = TI\left(\overline{U}|_{i,j,k}^{n}\right) \tag{3.29}$$

The TI operator for the 2^{nd} Order Runge-Kutta algorithm is given by

$$TI_{2RK}\left(\overline{U}|_{i,j,k}^{n}\right) \rightarrow \begin{cases} \overline{U}_{i,j,k}^{n+\frac{1}{2}} = \overline{U}_{i,j,k}^{n} - \frac{\Delta t}{J_{i,j,k}} \overline{F}_{i,j,k}^{Total}\left(\overline{U}_{i,j,k}^{n}\right) \\ TI_{2RK}\left(\overline{U}|_{i,j,k}^{n}\right) = \overline{U}_{i,j,k}^{n+1} = \frac{1}{2}\left(\overline{U}_{i,j,k}^{n+\frac{1}{2}} + \overline{U}_{i,j,k}^{n} - \frac{\Delta t}{J_{i,j,k}} \overline{F}_{i,j,k}^{Total}\left(\overline{U}_{i,j,k}^{n+\frac{1}{2}}\right)\right) \end{cases} \tag{3.30}$$

and for the 2^{nd} Order 4-Stages Runge-Kutta

$$TI_{2RK4S}\left(\overline{U}|^{n}_{i,j,k}\right) \rightarrow \begin{cases} \overline{U}^{n+\frac{1}{4}}_{i,j,k} = \overline{U}^{n}_{i,j,k} - \frac{1}{3}\frac{\Delta t}{J_{i,j,k}}\overline{F}^{Total}_{i,j,k}\left(\overline{U}^{n}_{i,j,k}\right) \\ \overline{U}^{n+\frac{2}{4}}_{i,j,k} = \overline{U}^{n+\frac{1}{4}}_{i,j,k} - \frac{1}{3}\frac{\Delta t}{J_{i,j,k}}\overline{F}^{Total}_{i,j,k}\left(\overline{U}^{n+\frac{1}{4}}_{i,j,k}\right) \\ \overline{U}^{n+\frac{3}{4}}_{i,j,k} = \overline{U}^{n+\frac{2}{4}}_{i,j,k} - \frac{1}{3}\frac{\Delta t}{J_{i,j,k}}\overline{F}^{Total}_{i,j,k}\left(\overline{U}^{n+\frac{2}{4}}_{i,j,k}\right) \\ TI_{2RK4S}\left(\overline{U}|^{n}_{i,j,k}\right) = \overline{U}^{n+1}_{i,j,k} = \frac{1}{4}\overline{U}^{n+\frac{2}{4}}_{i,j,k} + \frac{3}{4}\overline{U}^{n+\frac{3}{4}}_{i,j,k} - \frac{1}{4}\frac{\Delta t}{J_{i,j,k}}\overline{F}^{Total}_{i,j,k}\left(\overline{U}^{n+\frac{3}{4}}_{i,j,k}\right) \end{cases} \tag{3.31}$$

From above expressions, $J_{i,j,k}$ is the Jacobian of the curvilinear transformation defined as

$$J_{i,j,k} = \begin{vmatrix} \frac{\partial x}{\partial \xi} & \frac{\partial x}{\partial \eta} & \frac{\partial x}{\partial \zeta} \\ \frac{\partial y}{\partial \xi} & \frac{\partial y}{\partial \eta} & \frac{\partial y}{\partial \zeta} \\ \frac{\partial z}{\partial \xi} & \frac{\partial z}{\partial \eta} & \frac{\partial z}{\partial \zeta} \end{vmatrix} \tag{3.32}$$

The theoretical stability condition for both schemes is, for single species fluids,

$$CFL \leq 1 \longrightarrow 2^{nd}\ Order\ RK$$

$$CFL \leq 3 \longrightarrow 2^{nd}\ Order\ 4-Stages\ RK$$

However, as explained below, for multispecies problems such condition is sensitively restricted.

Enhanced Explicit Runge-Kutta for Multispecies Flows

For Multispecies problems, affordable computations in FLAMENCO are only feasible if essential modifications are introduced in the conceptual formulation of the Runge-Kutta scheme above. This issue is a direct consequence of the numerical discretisation of the Volume Fraction Equation (2.8) using expression (3.28) in Section 3.1.3 above. Indeed, several computational tests were conducted using Runge-Kutta algorithms (3.30) and (3.31) to find out that the actual maximum CFL numbers ensuring stability are $CFL \approx 0.01$ and $CFL \approx 0.04$ respectively. These low values are completely determined by the explicit advection of the volume fraction, whose characteristic time step is much lower than that of other phenomena. Consequently, a modified algorithm is proposed here, aiming to increase the effective time step in both situations.

If the CFL number is slightly above those restricted values mentioned, instabilities are initially seeded by small negative values ($\sim -10^{-15}$) of volume fraction provided by equation (3.28). If these perturbations occur in other thermodynamic or kinetic properties such as pressure, density, energy or velocity, their effects are quickly absorbed by the numerical error, damping and ultimately suppressing any negative effect other than

negligible inaccuracies. However, if they occur in any volume fraction, which of course is only defined in the interval $[0,1]$, the consequences are rather catastrophic. To overcome this problem, a mathematically supported control of volume fraction advection seems to be the best solution, enabling larger and stable time steps without impacting sensitively on the overall accuracy. Hence, variables z_k are tracked, ensuring that their values always fall within physical limits. In terms of the implementation in FLAMENCO, a threshold is established, forcing the algorithm to readapt itself if forbidden values are generated (and recomputing the dependent variable z_N to make alterations consistent).

$$
\begin{array}{l}
\textit{Solving Flow Time step } n \\
\quad\downarrow \\
\quad\quad\textit{Variable reconstruction} \\
\quad\quad\quad\downarrow \\
\quad\quad\quad \overline{U}_L, \overline{U}_R \\
\quad\quad\quad If \;\; z_k|_L \left\{ \begin{array}{l} < Threshold_b \\ > Threshold_a \end{array} \right. \Longrightarrow z_k|_L = \left\{ \begin{array}{ll} 0 & \\ 1 & \end{array} \right. \quad k = 1,...,N-1 \\
\quad\quad\quad If \;\; z_k|_R \left\{ \begin{array}{l} < Threshold_b \\ > Threshold_a \end{array} \right. \Longrightarrow z_k|_R = \left\{ \begin{array}{ll} 0 & \\ 1 & \end{array} \right. \quad k = 1,...,N-1 \\
\quad\quad\quad z_N|_L = 1 - \sum_{k=1}^{N-1} z_k|_L \\
\quad\quad\quad z_N|_R = 1 - \sum_{k=1}^{N-1} z_k|_R \\
\quad\quad\quad\downarrow \\
\quad\quad\quad \bullet \\
\quad\quad\quad \bullet \\
\quad\quad\quad \bullet \\
\quad\quad\quad\downarrow \\
\quad\quad\textit{Time Integration} \\
\quad\quad\quad\downarrow \\
\quad\quad\quad \overline{U}|_{i,j,k}^{n+1} = TI\left(\overline{U}|_{i,j,k}^{n}\right) \\
\quad\quad\quad If \;\; z_k|_{i,j,k}^{n+1} \left\{ \begin{array}{l} < Threshold_b \\ > Threshold_a \end{array} \right. \Longrightarrow z_k|_{i,j,k}^{n+1} = \left\{ \begin{array}{ll} 0 & \\ 1 & \end{array} \right. \quad k = 1,...,N-1 \\
\quad\quad\quad z_N|_{i,j,k}^{n+1} = 1 - \sum_{k=1}^{N-1} z_k|_{i,j,k}^{n+1} \\
\quad\quad\quad\downarrow
\end{array}
\tag{3.33}
$$

As seen, the control loop analyses the values of z_k at the reconstruction and time integration stages, resetting unphysical values to corrected ones. Although it could be initially thought that this artifice alters the natural development of the algorithm, a simple mathematical analysis reveals that all inaccuracies derived from this process are loaded into the volume fraction associated with species N, but do not affect the set of thermodynamic properties at all. This correction is similar to that forced in the Robin Hood algorithm proposed by Amsdem et al. [35] for the KIVA-II code, with the difference that errors here only penalise the cell under consideration rather than all the surrounding ones. Indeed, whereas KIVA-II deals with negative partial density of a given species in a computational volume by transferring mass from the neighbouring cells with an excess of that species (in an artificial-diffusion like mechanism), here one species is rather "transformed" into the other. As in KIVA-II, this process is strictly mass-conservative, so the Finite-Volume approach retains this advantage. From a physical point of view, this operation can be seen as a species transformation that forces volume fractions to lie within

$[0, 1]$ by introducing an error. Since the error is non-accumulative (at the end of each time step it is spread to other thermodynamic variables whose field of definition will not be violated) and the values for $Threshold_b$, $Threshold_a$ are calibrated in this study as -10^{-15} and 1+10^{-15} respectively, the method provides a consistent way of increasing stability. In particular, it was found that the maximum stable CFL number rises up to 0.4 for the 2^{nd} Order Runge-Kutta and to 1.0 for the 2^{nd} Order 4-Stages Runge-Kutta with an associated relative error smaller than 10^{-10}. CFL numbers used in final computations are, however, smaller since errors induced by these corrections decrease rapidly with time step size. Finally, another important feature of this procedure is the reconstruction independence provided in terms of stability. In this way, high-order reconstruction schemes which are not completely monotone are made compatible with the model, as demonstrated in Section 4.3.

3.2 High-Order High Resolution Schemes

The main objective of this research is to develop a computationally efficient and accurate tool capable of simulating complex physical problems. Although the expression "computationally efficient" encompasses a broad range of qualities, here it refers to the possibility of predicting the main flow features of a given problem by minimising the grid resolution. To achieve this, one of the most important issues to take into account is the reconstruction methodology employed for the convective terms. Bearing in mind this binomial Coarse discretisation-Very good resolution, it seems clear that High-Order High-Resolution schemes need to be considered.

There are many studies in the literature about High-Order High-Resolution methods, showing the benefits of their implementation and mentioning some issues to bear in mind when dealing with them. For example, van Leer [36, 37, 38, 39, 40] produced some in-depth studies on stability of High-Order methods. In his work, the oscillatory behaviour of high-order schemes near discontinuities, as expected according to Godunov's Theorem [26], was analysed, developing novel limiting functions that suppress such oscillatory behaviour by reducing the reconstruction order locally, but without decreasing the general order of the problem. These functions fall within the framework of Total Variation Diminishing schemes (TVD), which ensures that a given variable has a monotonic behaviour regardless of the proximity to discontinuities, thus avoiding spurious numerical oscillations. In this field of application, Harten [41], Sweby [42] and Roe [43, 44] have deeply contributed to the understanding of the fundamentals that cause this unwanted behaviour. In addition, other authors like Osher [45] present numerical and thermodynamic analogies to rationally explain solution architecture.

Another well known and broadly extended series of methods for high-order high-resolution reconstruction is the Essentially Non-Oscillatory (ENO) family. Regarding their evolution in particular, the Weighted Essentially Non-Oscillatory

(WENO) schemes are comparable in terms of accuracy, efficiency, computational cost and stability to the most novel TVD models developed up to date. Contrary to what happens in ENO reconstruction, where the locally smoothest "candidate" from a series of polynomials is used to interpolate near discontinuities (see Casper [46] and Harten [47]), in WENO methods all local "candidates" are rather considered, weighting their contribution to the final interpolation in such a way that in smooth regions the scheme has maximum order of accuracy, while near discontinuities the contribution of the polynomials assigned to the stencils containing discontinuities is minimised. As a consequence, an adaptive scheme able to take advantage of the full potential of polynomial reconstruction is built.

Many authors have investigated the numerical properties and performance of WENO methods, digging into the mathematical definition that makes them suitable for compressible gases. For instance, Grasso et al. [48] developed in their work a non-staggered two-dimensional WENO scheme for aeroacoustic problems. Additional revisions, improvements and generalisations of existing WENO schemes were performed by Johnsen et al. [49] and Burger et al. [50] by developing both variants of typical WENO schemes to deal with multispecies flows in a stable manner. For its part, Hu et al. [51] derived a novel methodology to apply WENO reconstruction to Unstructured triangular grids, overcoming some of the main problems associated with these typical meshes. As for the optimisation of advanced WENO methods, Jiang et al. [52] analysed, tested, modified and improved typical WENO implementations. They proposed a novel way of measuring the smoothness of the solution, deriving a model with enhanced resolution at larger regions than conventional WENO algorithms. Finally, comparison between TVD and ENO/WENO family has been extensively done, encompassing from the level of accuracy achieved to the stability of the model. The reader is referred to works from Shu [53] and Mikhailovet al. [54] for TVD vs ENO/WENO performance and to Shu [55] for a more recent comparison between TVD, WENO and Galerkin methods.

3.2.1 Weighted Essentially Non-Oscillatory schemes

The 3D dimension-by-dimension WENO scheme for multispecies compressible flows from Titarev et al. [56] has been implemented in FLAMENCO in order to have a well known model with contrasted accuracy and validity to compare with. Following guidelines written in Shi et al. [57] and [56], the reconstruction of any thermodynamic property in the three-dimensional space can be performed by partial reconstructions on each independent direction. In this way, given the property $\phi = \phi(\xi, \eta, \zeta)$ physically defined in the whole domain but numerically available only at cell centres so that at cell

i,j,k is

$$\phi_{i,j,k} = \frac{1}{\Delta\xi}\frac{1}{\Delta\eta}\frac{1}{\Delta\zeta}\int_{\xi_{i-\frac{1}{2},j,k}}^{\xi_{i+\frac{1}{2},j,k}}\int_{\eta_{i,j+\frac{1}{2},k}}^{\eta_{i,j+\frac{1}{2},k}}\int_{\zeta_{i,j,k-\frac{1}{2}}}^{\zeta_{i,j,k+\frac{1}{2}}}\phi(\xi,\eta,\zeta)\,d\xi d\eta d\zeta \tag{3.34}$$

is satisfied, the three-dimensional reconstruction at cell interface $i-\frac{1}{2},j,k$ for independent Cartesian directions (ξ,η,ζ) can be split into three stages

$$\begin{aligned}
&Step\ 1: Reconstruction\ in\ \xi \quad \begin{cases} \phi^L_{j,k} = \frac{1}{\Delta\eta}\frac{1}{\Delta\zeta}\int_{\eta_{i,j+\frac{1}{2},k}}^{\eta_{i,j+\frac{1}{2},k}}\int_{\zeta_{i,j,k-\frac{1}{2}}}^{\zeta_{i,j,k+\frac{1}{2}}}\phi\left(\xi^L_{i-\frac{1}{2},j,k},\eta,\zeta\right)d\eta d\zeta \\ \phi^R_{j,k} = \frac{1}{\Delta\eta}\frac{1}{\Delta\zeta}\int_{\eta_{i,j+\frac{1}{2},k}}^{\eta_{i,j+\frac{1}{2},k}}\int_{\zeta_{i,j,k-\frac{1}{2}}}^{\zeta_{i,j,k+\frac{1}{2}}}\phi\left(\xi^R_{i-\frac{1}{2},j,k},\eta,\zeta\right)d\eta d\zeta \end{cases} \\
&Step\ 2: Reconstruction\ in\ \eta \quad \begin{cases} \phi^L_{k} = \frac{1}{\Delta\zeta}\int_{\zeta_{i,j,k-\frac{1}{2}}}^{\zeta_{i,j,k+\frac{1}{2}}}\phi\left(\xi^L_{i-\frac{1}{2},j,k},\eta_\alpha,\zeta\right)d\zeta \\ \phi^R_{k} = \frac{1}{\Delta\zeta}\int_{\zeta_{i,j,k-\frac{1}{2}}}^{\zeta_{i,j,k+\frac{1}{2}}}\phi\left(\xi^R_{i-\frac{1}{2},j,k},\eta_\alpha,\zeta\right)d\zeta \end{cases} \\
&Step\ 3: Reconstruction\ in\ \zeta \quad \begin{cases} \phi^L = \phi\left(\xi^L_{i-\frac{1}{2},j,k},\eta_\alpha,\zeta_\beta\right) \\ \phi^R = \phi\left(\xi^R_{i-\frac{1}{2},j,k},\eta_\alpha,\zeta_\beta\right) \end{cases}
\end{aligned} \tag{3.35}$$

giving the final reconstructed values at the cell interface

$$\begin{aligned}
\phi^L &= \phi\left(\xi^L_{i-\frac{1}{2},j,k},\eta_\alpha,\zeta_\beta\right) \\
\phi^R &= \phi\left(\xi^R_{i-\frac{1}{2},j,k},\eta_\alpha,\zeta_\beta\right)
\end{aligned} \tag{3.36}$$

Parameters η_α and ζ_β depend on the Gaussian Integration Points used to approximate the general integral

$$\int_{S_{i-\frac{1}{2}}}^{S_{i+\frac{1}{2}}}\phi(\varepsilon)\,d\varepsilon \tag{3.37}$$

In this study, the optimum approximation for two Gaussian Integration Points suggested by [56] is employed, so

$$\int_{S_{i-\frac{1}{2}}}^{S_{i+\frac{1}{2}}} \phi(\varepsilon)\, d\varepsilon = \frac{\Delta\varepsilon}{2}\left(\phi \underbrace{\left(S_i - \frac{\Delta\varepsilon}{2\sqrt{3}}\right)}_{\substack{1^{st}\ Gaussian \\ Int.\ Point}} + \phi \underbrace{\left(S_i + \frac{\Delta\varepsilon}{2\sqrt{3}}\right)}_{\substack{2^{nd}\ Gaussian \\ Int.\ Point}} \right) \tag{3.38}$$

and therefore

$$\begin{aligned}
\phi^p\left(\xi^p_{i-\frac{1}{2},j,k}, \eta_\alpha, \zeta\right) &= \frac{1}{2}\left(\phi\left(\xi^p_{i-\frac{1}{2},j,k}, \eta_{i-\frac{1}{2},j,k} - \frac{\Delta\eta}{2\sqrt{3}}, \zeta\right) + \phi\left(\xi^p_{i-\frac{1}{2},j,k}, \eta_{i-\frac{1}{2},j,k} + \frac{\Delta\eta}{2\sqrt{3}}, \zeta\right)\right) \\
\phi^p\left(\xi^p_{i-\frac{1}{2},j,k}, \eta_\alpha, \zeta_\beta\right) &= \frac{\phi\left(\xi^p_{i-\frac{1}{2},j,k}, \eta_{i-\frac{1}{2},j,k} - \frac{\Delta\eta}{2\sqrt{3}}, \zeta_{i-\frac{1}{2},j,k} - \frac{\Delta\zeta}{2\sqrt{3}}\right) + \phi\left(\xi^p_{i-\frac{1}{2},j,k}, \eta_{i-\frac{1}{2},j,k} - \frac{\Delta\eta}{2\sqrt{3}}, \zeta_{i-\frac{1}{2},j,k} + \frac{\Delta\zeta}{2\sqrt{3}}\right)}{4} \\
&\quad + \frac{\phi\left(\xi^p_{i-\frac{1}{2},j,k}, \eta_{i-\frac{1}{2},j,k} + \frac{\Delta\eta}{2\sqrt{3}}, \zeta_{i-\frac{1}{2},j,k} - \frac{\Delta\zeta}{2\sqrt{3}}\right) + \phi\left(\xi^p_{i-\frac{1}{2},j,k}, \eta_{i-\frac{1}{2},j,k} + \frac{\Delta\eta}{2\sqrt{3}}, \zeta_{i-\frac{1}{2},j,k} + \frac{\Delta\zeta}{2\sqrt{3}}\right)}{4}
\end{aligned} \tag{3.39}$$

with p = L, R. For 5^{th} Order reconstruction, left and right states at the interface $i-\frac{1}{2},j,k$ (note that for cell interface $i+\frac{1}{2},j,k$ the derivation is analogous) require a 6-point stencil (5 points for each state with only 4-overlapped values) in ξ and 5-point stencils in both η and ζ. A representation of the stencils is presented in Figure 3.2.

Finally after some algebra (see Appendix B) and taking $\Delta\xi = 1$, $\Delta\eta = 1$, $\Delta\zeta = 1$, it is possible to write the convective fluxes as

$$\begin{aligned}
F^{3D\,WENO}_{i-\frac{1}{2},j,k} = \frac{\beta|_{i-\frac{1}{2},j,k}}{4}\Big(&F\left\{\overline{U}^L\left(\bar{I}_{\alpha_1\beta_1}\right), \overline{U}^R\left(\bar{I}_{\alpha_1\beta_1}\right)\right\} + F\left\{\overline{U}^L\left(\bar{I}_{\alpha_1\beta_2}\right), \overline{U}^R\left(\bar{I}_{\alpha_1\beta_2}\right)\right\} \\
&+ F\left\{\overline{U}^L\left(\bar{I}_{\alpha_2\beta_1}\right), \overline{U}^R\left(\bar{I}_{\alpha_2\beta_1}\right)\right\} + F\left\{\overline{U}^L\left(\bar{I}_{\alpha_2\beta_2}\right), \overline{U}^R\left(\bar{I}_{\alpha_2\beta_2}\right)\right\}\Big)
\end{aligned} \tag{3.40}$$

$$\begin{aligned}
\bar{I}_{\alpha_1\beta_1} &= \left(\xi_{i-\frac{1}{2},j,k}, \eta_{i-\frac{1}{2},j,k} - \frac{1}{2\sqrt{3}}, \zeta_{i-\frac{1}{2},j,k} - \frac{1}{2\sqrt{3}}\right) \\
\bar{I}_{\alpha_1\beta_2} &= \left(\xi_{i-\frac{1}{2},j,k}, \eta_{i-\frac{1}{2},j,k} - \frac{1}{2\sqrt{3}}, \zeta_{i-\frac{1}{2},j,k} + \frac{1}{2\sqrt{3}}\right) \\
\bar{I}_{\alpha_2\beta_1} &= \left(\xi_{i-\frac{1}{2},j,k}, \eta_{i-\frac{1}{2},j,k} + \frac{1}{2\sqrt{3}}, \zeta_{i-\frac{1}{2},j,k} - \frac{1}{2\sqrt{3}}\right) \\
\bar{I}_{\alpha_2\beta_2} &= \left(\xi_{i-\frac{1}{2},j,k}, \eta_{i-\frac{1}{2},j,k} + \frac{1}{2\sqrt{3}}, \zeta_{i-\frac{1}{2},j,k} + \frac{1}{2\sqrt{3}}\right)
\end{aligned} \tag{3.41}$$

The exact definition of one-dimensional WENO reconstruction that allows obtaining $\overline{U}^L, \overline{U}^R$ at all Integration Points is also shown in Appendix B.

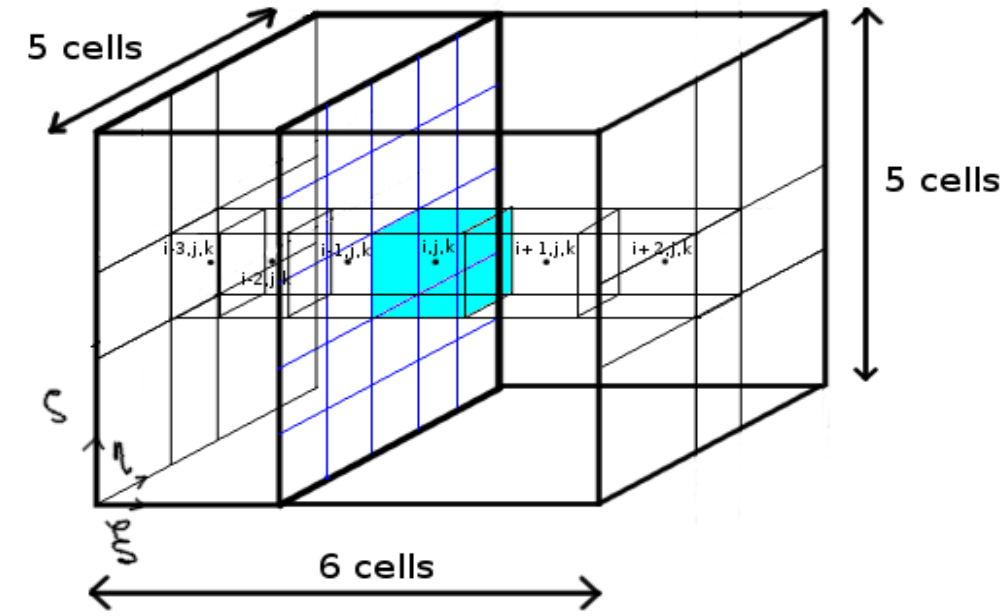

(a) 3D stencil for WENO reconstruction

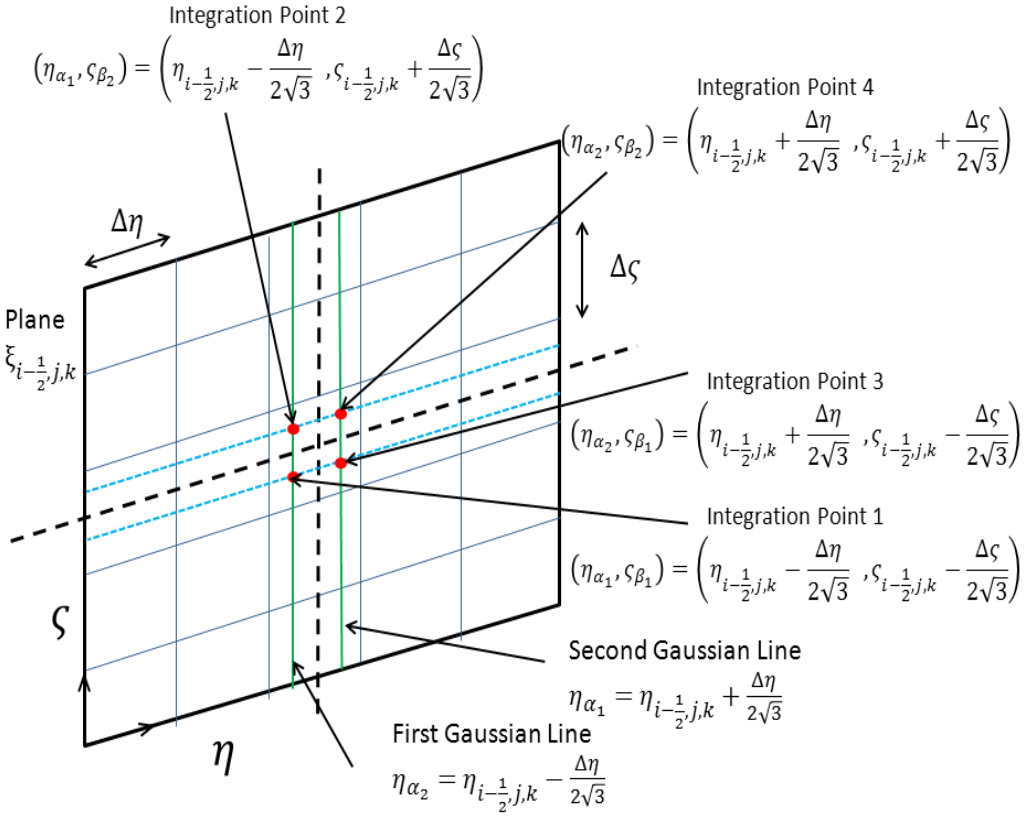

(b) Definition of the 4 integration points

Figure 3.2: Stencil for WENO scheme and reconstruction points

Simplified WENO for efficient computations

As will be shown later in Section 4.3.3, the computational cost of the implementation (3.40)-(3.41) in FLAMENCO is too high to allow its application to large domains with many computational cells (>100000 cells). Hence, a simplified version of the WENO algorithm is used to simulate the Dry Low NOx GTU Combustor. This simplification consists of lowering the order of accuracy when integrating at the cell interface, equation (3.35). In this way, the integral is no longer approximated with expression (3.38) but with

$$\int_{S_{i-\frac{1}{2}}}^{S_{i+\frac{1}{2}}} \phi(\varepsilon)\, d\varepsilon = \left(S_{i+\frac{1}{2}} - S_{i-\frac{1}{2}}\right) \phi\left(\frac{S_{i+\frac{1}{2}} + S_{i-\frac{1}{2}}}{2}\right) \tag{3.42}$$

and equation (3.40) becomes

$$F^{3D\,WENO}_{i-\frac{1}{2},j,k} = \beta|_{i-\frac{1}{2},j,k} F^{HLLC}_{i-\frac{1}{2},j,k}\left(\overline{U}^{L}_{WENO\,1D}, \overline{U}^{R}_{WENO\,1D}\right) \tag{3.43}$$

where $\overline{U}^{L}_{WENO\,1D}, \overline{U}^{R}_{WENO\,1D}$ are obtained using reconstructed variables according to

$$\phi^{p}_{i-\frac{1}{2},j,k} = \phi_{i-1} + \omega_{0_p} v_{0_p} + \omega_{1_p} v_{1_p} + \omega_{2_p} v_{2_p} \quad p = L, R \tag{3.44}$$

with

$$\begin{array}{ll} \omega_{0_p} = \frac{\alpha_{0_p}}{\alpha_{0_p}+\alpha_{p_L}+\alpha_{2_p}} & \alpha_{0_p} = \frac{0.3}{\left(\varepsilon+\beta_{0_p}\right)^2} \\ \omega_{1_p} = \frac{\alpha_{1_p}}{\alpha_{0_p}+\alpha_{p_L}+\alpha_{2_p}} & \alpha_{1_p} = \frac{0.6}{\left(\varepsilon+\beta_{1_p}\right)^2} \quad p = L, R \\ \omega_{2_p} = \frac{\alpha_{2_p}}{\alpha_{0_p}+\alpha_{p_L}+\alpha_{2_p}} & \alpha_{2_p} = \frac{0.1}{\left(\varepsilon+\beta_{2_p}\right)^2} \end{array} \tag{3.45}$$

$$\begin{array}{l} \beta_{0_L} = \frac{13}{12}\left(\phi_{i-1} - 2\phi_i + \phi_{i+1}\right)^2 + \frac{1}{4}\left(3\phi_{i-1} - 4\phi_i + \phi_{i+1}\right)^2 \\ \beta_{1_L} = \frac{13}{12}\left(\phi_{i-2} - 2\phi_{i-1} + \phi_i\right)^2 + \frac{1}{4}\left(\phi_{i-2} - \phi_i\right)^2 \\ \beta_{2_L} = \frac{13}{12}\left(\phi_{i-3} - 2\phi_{i-2} + \phi_{i-1}\right)^2 + \frac{1}{4}\left(\phi_{i-3} - 4\phi_{i-2} + 3\phi_{i-1}\right)^2 \\ \\ \beta_{0_R} = \frac{13}{12}\left(\phi_i - 2\phi_{i-1} + \phi_{i-2}\right)^2 + \frac{1}{4}\left(3\phi_i - 4\phi_{i-1} + \phi_{i-2}\right)^2 \\ \beta_{1_R} = \frac{13}{12}\left(\phi_{i+1} - 2\phi_i + \phi_{i-1}\right)^2 + \frac{1}{4}\left(\phi_{i+1} - \phi_{i-1}\right)^2 \\ \beta_{2_R} = \frac{13}{12}\left(\phi_{i+2} - 2\phi_{i+1} + \phi_i\right)^2 + \frac{1}{4}\left(\phi_{i+2} - 4\phi_{i+1} + 3\phi_i\right)^2 \end{array} \tag{3.46}$$

and

$$\begin{array}{ll} v_{0_L} = \frac{1}{6}\left(-4\phi_{i-1} + 5\phi_i - \phi_{i+1}\right) & v_{0_R} = \frac{1}{6}\left(-4\phi_i + 5\phi_{i-1} - \phi_{i-2}\right) \\ v_{1_L} = \frac{1}{6}\left(-\phi_{i-2} - \phi_{i-1} + 2\phi_i\right) & v_{1_R} = \frac{1}{6}\left(-\phi_{i+1} - \phi_i + 2\phi_{i-1}\right) \\ v_{2_L} = \frac{1}{6}\left(-2\phi_{i-3} - 7\phi_{i-2} + 5\phi_{i-1}\right) & v_{2_R} = \frac{1}{6}\left(-2\phi_{i+2} - 7\phi_{i+1} + 5\phi_i\right) \end{array} \tag{3.47}$$

where ϕ stands for a generic physical variable. The residual coefficient ε can be taken $\varepsilon = 10^{-15}$ for a double precision machine, since its only purpose is to avoid zero values

in the denominator from (3.45). Although less accurate, this way of proceeding allows expensive simulations (>100000 cells) in FLAMENCO, which otherwise would not have been possible with the resources available.

3.2.2 Total Variation Diminishing schemes

Total Variation Diminishing methods are represented in this work by the 2^{nd} Order Minmod Limited and 5^{th} Order MLP (Multi-dimensional Limiting Process) schemes. As seen, whereas the first one is really stable but the accuracy is totally insufficient for the Dry Low NOx GTU combustor simulation, the latter is both highly stable and accurate, making of it a perfect candidate to be used in FLAMENCO

2nd Order Minmod

This 2^{nd} Order scheme limited with the Minmod algorithm (see Harten et al. [58] and Kurganov et al. [59]) can be formulated as

$$F^{2^{nd}\,Minmod}_{i-\frac{1}{2},j,k} = \beta|_{i-\frac{1}{2},j,k} F^{HLLC}_{i-\frac{1}{2},j,k}\left(\overline{U}^{L}_{2^{nd}\,Minmod}, \overline{U}^{R}_{2^{nd}\,Minmod}\right) \tag{3.48}$$

with the vector of conserved variables at left and right states composed by reconstructed magnitudes as

$$\begin{aligned}
\phi^{L}_{2^{nd}\,Minmod} &= \phi_{i-1} + \tfrac{1}{2}(\phi_{i-1} - \phi_{i-2}) \max\left(0, \min\left(1, \tfrac{(\phi_i - \phi_{i-1})}{(\phi_{i-1} - \phi_{i-2})}\right)\right) \\
\phi^{R}_{2^{nd}\,Minmod} &= \phi_{i} - \tfrac{1}{2}(\phi_{i+1} - \phi_{i}) \max\left(0, \min\left(1, \tfrac{(\phi_i - \phi_{i-1})}{(\phi_{i+1} - \phi_{i})}\right)\right)
\end{aligned} \tag{3.49}$$

5th Order MLP scheme

The relatively new 5^{th} Order MLP scheme introduced by Kim et al. [60, 61] represents an accurate and very stable way of reconstructing physical variables at interfaces. Additionally, its simple formulation and good behaviour in three-dimensional problems provides a robust numerical structure to be introduced in FLAMENCO. The definition of this approach is exactly the same as in equation (3.48), but now the reconstruction stage reads

$$\begin{aligned}
\phi^{L}_{MLP} &= \phi_{i-1} + \tfrac{1}{2}(\phi_{i-1} - \phi_{i-2}) \cdot \max\left(0, \min\left(2, 2\left(\tfrac{\phi_i - \phi_{i-1}}{\phi_{i-1} - \phi_{i-2}}\right)\psi_L\right)\right) \\
\phi^{R}_{MLP} &= \phi_{i} - \tfrac{1}{2}(\phi_{i+1} - \phi_{i}) \cdot \max\left(0, \min\left(2, 2\left(\tfrac{\phi_i - \phi_{i-1}}{\phi_{i+1} - \phi_{i}}\right)\psi_R\right)\right)
\end{aligned} \tag{3.50}$$

with limiting functions

$$\begin{aligned}\psi_L &= \left(-2\left(\frac{\phi_{i-2}-\phi_{i-3}}{\phi_{i-1}-\phi_{i-2}}\right)+11+\frac{1}{30}\left(\frac{\phi_i-\phi_{i-1}}{\phi_{i-1}-\phi_{i-2}}\right)\left(24-\frac{3(\phi_{i+1}-\phi_i)}{\phi_i-\phi_{i-1}}\right)\right)\\ \psi_R &= \left(-2\left(\frac{\phi_{i+2}-\phi_{i+1}}{\phi_{i+1}-\phi_i}\right)+11+\frac{1}{30}\left(\frac{\phi_i-\phi_{i-1}}{\phi_{i+1}-\phi_i}\right)\left(24-\frac{3(\phi_{i-1}-\phi_{i-2})}{\phi_i-\phi_{i-1}}\right)\right)\end{aligned} \tag{3.51}$$

3.3 Thermodynamic Closures

Once all physical and mathematical models are posed and numerical methods are selected, the problem must be thermodynamically closed. At this point two closures are possible, the isothermal and isobaric closures. As mentioned before, although isothermal closure is more "physically" accurate, since it considers only one temperature at each point of the domain, its applicability in conjunction with high-order schemes may cause spurious oscillations near discontinuities (see Karni [62] and Abgrall [63]). To overcome this issue, Allaire et al. [21] proposed the isobaric closure, asserting that if the same pressure at each point of the domain is considered instead of the same temperature, spurious oscillations are completely removed. Furthermore, since the mixture is defined at every point of the domain where more than one species exists, from a macroscopic perspective there is only one temperature per spatial point, so the "physical" consistency of the model remains unaltered.

3.3.1 Equation Of State

The mathematical problem requires an equation of the type

$$\varepsilon = EOS(p,\rho) \tag{3.52}$$

to relate the thermodynamic variables and keep consistent the flow field. Although FLAMENCO has three models (EOS for perfect gas, ideal gas with variable specific heat capacity ratio and van der Waals gas), the relevant choice for the problem under consideration here is the EOS for perfect gas, which can be summarised as

$$\begin{aligned}&\varepsilon = \frac{1}{\gamma-1}\frac{p}{\rho}\\ &\varepsilon = C_v T \qquad\qquad C_v \equiv Const.\\ &\gamma = \frac{C_p}{C_v} \qquad\qquad C_p \equiv Const.\end{aligned} \tag{3.53}$$

3.3.2 Iso-Baric Closure

The isobaric closure is a numerical artefact that, without impacting on the general consistency of the physical model, allows avoiding spurious numerical oscillations in multispecies flows near discontinuities. Using this approach, the mixture is defined as

$$
\begin{aligned}
1 &= \sum_{k=1}^{N_{species}} z_k \\
\rho &= \sum_{k=1}^{N_{species}} z_k \rho_k \\
\rho\varepsilon &= \sum_{k=1}^{N_{species}} z_k \rho_k \varepsilon_k \\
\rho\varepsilon &= \sum_{k=1}^{N_{species}} \frac{z_k}{\gamma_k - 1} p_k = p \sum_{k=1}^{N_{species}} \frac{z_k}{\gamma_k - 1} \longrightarrow p = \frac{\rho\varepsilon}{\sum_{k=1}^{N_{species}} \frac{z_k}{\gamma_k - 1}} \\
R &= \sum_{k=1}^{N_{species}} R_k \frac{z_k \rho_k}{\rho} \\
T &= \frac{p}{\rho R} \\
\gamma &= 1 + \frac{1}{\sum_{k=1}^{N_{species}} \frac{z_i}{\gamma_k - 1}}
\end{aligned}
\tag{3.54}
$$

System above yields all necessary variables as a function of the conserved variables obtained from the numerical scheme. Thus, this closure procedure is performed after numerical integration of the conserved variables, and is sufficient to update the flow field to continue with the next time step.

Chapter 4

Analysis of the model and validation

4.1 Main features of the numerical approach with FLAMENCO

As mentioned in the introduction, FLAMENCO is a numerical algorithm devised to deal with and derived according to the following elements

- **Compressible** →Solution of the Local Riemann Problem at each cell interface
- **Turbulent** → Modelisation using Implicit Large-Eddie Simulation
- **3D** → Unsplit fluxes with 3D reconstruction and 1D-by-1D reconstruction. Curvilinear grids considered and transformed into Cartesian coordinates.
- **Unsteady** → 2^{nd} Order Explicit Runge-Kutta and 2^{nd} Order Explicit 4-Stages Runge-Kutta for stable computations. Enhanced time integration scheme for multispecies models.
- **Multispecies** → 5-Equation Transport Model with iso-baric closure for the mixture region
- **High-Order, High-Resolution** → 5^{th} Order WENO and MLP reconstruction schemes
- **Viscous** → 2^{nd} Order Central differences for viscous discretisation
- **Perfect gas** → Perfect gas Equation of State

This algorithm performs well in many situations, even when some of them set with critical conditions (geometrically and physically speaking). In particular, when applied to the Dry Low NOx GTU Combustor, the combination of small cells, low numerical dissipation due to the high-order scheme and energy production at boundaries creates, within the jet duct, bounded numerical instabilities. Although limited, such instabilities induce unphysical values of pressure, which ends up corrupting the final solution of the problem. This error has already been pointed out by Pulliam [64] for High-Order schemes with extremely low or zero viscosity. As mentioned in Chapter 1, several strategies have been followed in order to overcome this particular problem, resulting in the implementation of several features.

Firstly, a number of boundary conditions following different principles (Non-reflecting, Partially Non-Reflecting and Nozzle-type subsonic inflows) were used. Secondly, locally high-dissipative schemes were employed at certain regions of the domain. Thirdly, instead of reconstruction from conserved variables, reconstruction from primitive variables (including volume fraction) was employed to minimise numerical oscillations. Finally, small grid modifications were introduced, making sure that the effect of such deviation from the actual problem was not relevant at all. More on this last point in Section 5.2.

4.2 Strategies to balance low dissipation

4.2.1 Boundary Conditions

The main objective of the subsonic inflows introduced is to evacuate as much energy as possible from the interior of the jet injector while keeping the expected specifications (Reynolds and Swirl numbers). In the same way, the outflow has been defined to minimise wave reflections inside the combustion chamber. Finally, changes have been made at the walls of the jet injector, in order to damp as much as possible the propagation of transversally-bouncing acoustic waves.

Non-reflecting Subsonic Inflow and Outflow

This subsonic boundary condition is based on enabling free transit of characteristic waves. Hence, the subsonic inflow evacuates one outcoming wave with no reflection at all, introducing 4+N incoming waves, and the subsonic outflow evacuates 4+N outcoming waves with no reflection, introducing one incoming wave into the computational domain (N stands for number of species). Considering the one-dimensional system of conservation laws as

$$\frac{\partial \overline{U}(t,\overline{x})}{\partial t} + \frac{\partial \overline{F}(\overline{U}(t,\overline{x}))}{\partial x} = 0 \rightarrow \frac{\partial \overline{U}(t,\overline{x})}{\partial t} + \frac{\partial \overline{F}(\overline{U}(t,\overline{x}))}{\partial \overline{U}(t,\overline{x})} \frac{\partial \overline{U}(t,\overline{x})}{\partial x} = 0 \tag{4.1}$$

where

$$\overline{U} = \begin{pmatrix} z_1\rho_1 \\ z_2\rho_2 \\ \vdots \\ z_N\rho_N \\ \rho u \\ \rho v \\ \rho w \\ E \end{pmatrix}, \ \overline{F} = \begin{pmatrix} z_1\rho_1 u \\ z_2\rho_2 u \\ \vdots \\ z_N\rho_N u \\ \rho u^2 + p \\ \rho uv \\ \rho uw \\ u(E+p) \end{pmatrix} \tag{4.2}$$

the eigenvalues of the system

$$\left| \frac{\partial \overline{F}(\overline{U}(t,\bar{x}))}{\partial \overline{U}(t,\bar{x})} - \lambda \bar{\bar{I}} \right| = 0 \tag{4.3}$$

are $\lambda_1 = u - a$, $\lambda_2 = \lambda_3 = ... = \lambda_{M-1} = u$, $\lambda_M = u + a$, where a is the speed of sound. In the domain illustrated in Figure 4.1, the configuration of incoming and outcoming waves at each boundary is depicted for a single species problem.

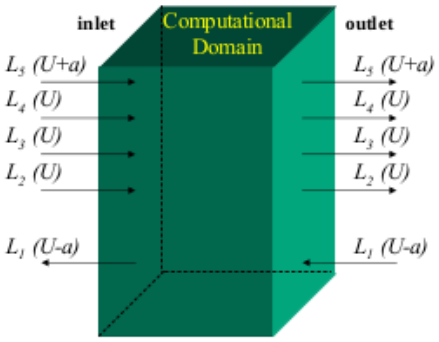

Figure 4.1: Incoming and outcoming waves at the boundary. Reproduced from [65]

According to Blazek [66], this configuration can be mathematically expressed as

$$\textbf{Subsonic Inflow} \begin{cases} p_b = \frac{1}{2}\left[p_a + p_d - \rho_0 a_0 \left(n_x (u_a - u_d) + n_y (v_a - v_d) + n_z (w_a - w_d)\right)\right] \\ \rho_b = \rho_a + \frac{(p_b - p_a)}{a_0^2} \\ u_b = u_a - \frac{n_x (p_a - p_b)}{\rho_0 a_0} \\ v_b = v_a - \frac{n_y (p_a - p_b)}{\rho_0 a_0} \\ w_b = w_a - \frac{n_z (p_a - p_b)}{\rho_0 a_0} \end{cases}$$

$$\textbf{Subsonic Outflow} \begin{cases} p_b = p_a \\ \rho_b = \rho_d + \frac{(p_b - p_d)}{a_0^2} \\ u_b = u_d - \frac{n_x (p_d - p_b)}{\rho_0 a_0} \\ v_b = v_d - \frac{n_y (p_d - p_b)}{\rho_0 a_0} \\ w_b = w_d - \frac{n_z (p_d - p_b)}{\rho_0 a_0} \end{cases} \tag{4.4}$$

where n_x, n_y, n_z are the components of the unitary vector normal to the boundary, a refers to the target value, b to the real value at the boundary and d to the first cell within the domain next to the boundary. Note that reference values ρ_0, a_0 are typically taken as close as possible to the boundary (in the present work, $\rho_0 = \rho_d$; $a_0 = a_d$). Numerically speaking, equations in (4.4) are simply a relaxation process where the conditions at the interface, "target conditions", are smoothly achieved in time. In the same way, once the specified magnitudes are achieved, any deviation from them is not instantaneously killed, but is "redirected" towards the proper value by introducing opposite perturbations in the fluid.

Partially Non-reflecting Subsonic Inflow

This method is based on the idea of relaxing the conditions at the inflow so the reflection of each outgoing wave can be damped at the expense of the information introduced. A relaxation factor is included and adapted to achieve proper equilibrium between the conditions imposed and the intensity of the wave reflected. The formulation in this case is a variation of the model proposed by [67] according to suggestions made by Thomson [68] and can be expressed as

$$L_5 = \sigma \rho a^2 \frac{U_z - U_z^\infty}{L} \tag{4.5}$$

$$L_2 = \frac{\gamma - 1}{2}(L_1 + L_5) + \frac{\rho a^2}{T}\frac{\partial T}{\partial t} \tag{4.6}$$

$$\frac{\partial U_z}{\partial t} = \frac{L_1 - L_5}{2\rho a} \tag{4.7}$$

where σ is the relaxation factor, U_z^∞ is the target velocity normal to the boundary, U_z is the actual velocity normal to the boundary and L is the characteristic longitude of the jet injector tube. Note that ρ is obtained by solving as many continuity equations as species are in the problem, and the wave temporal amplitude of the first wave L_1 is computed from inside the domain as

$$L_1 = (U_z - a)\left(\frac{\partial p}{\partial z} - \rho a \frac{\partial U_z}{\partial z}\right) \tag{4.8}$$

Having computed L_1 and L_5, the wave temporal amplitude L_2 can be obtained from (4.6) and used to compute temperature, pressure, etc., at the boundary. Then, equation (4.7) provides the normal velocity to the boundary (note that the gradient is at the boundary).

Nozzle-type Inflow

The nozzle type subsonic inflow consists of setting constant total pressure and temperature, extrapolating Mach number from the interior of the domain. Magnitudes such as volume fractions or volume fraction times partial densities are imposed at the boundaries. Using equations (4.9) and (4.10), density can be computed using the equation of state of the fluid, which in this case is perfect gas. Then, the normal velocity is easily calculated through (4.11). Note that this inflow was developed for only one non-zero velocity component, as it is the case under consideration (normal to the boundary). The outcome of this boundary condition is practically the same as the Non-reflecting one in equation (4.4). However, this method is asymptotically slower than the other one, so not only it takes more time to reach the operating conditions, but is also less stiff, which implies slower responses to eventual deviations from the target values.

$$P = P_0 \left(1 + \frac{\gamma - 1}{2} M^2\right)^{-\frac{\gamma}{\gamma - 1}} \tag{4.9}$$

$$T = T_0 \left(1 + \frac{\gamma - 1}{2} M^2\right) \tag{4.10}$$

$$U = M^2 \frac{\gamma P}{\rho} \tag{4.11}$$

4.2.2 Reconstruction from Primitive Variables

Reconstruction from primitive variables instead of conserved variables is a broadly extended procedure to calculate convective fluxes. Here, it is not only advisable but necessary if controllable dissipation is desired. Furthermore, reconstruction from primitive variables in high-order schemes avoids spreading non-linear errors derived from conserved variable reconstruction (where the product of two variables, i.e., momentum, is reconstructed). Table 4.1 shows both reconstruction methodologies for a two species flow, indicating which variables are reconstructed and which are computed from them.

Primitive variable reconstruction followed in FLAMENCO is presented in system (4.12). As seen, a sequential methodology allows calculating all variables in a consistent way

	Reconstruction Methodology	
	Conserved Variables	**Primitive Variables**
$\rho_1 z_1$	Reconstructed	Reconstructed
$\rho_2 z_2$	Reconstructed	Reconstructed
z_1	Reconstructed	Reconstructed
z_2	Computed	Computed
u	Computed	Reconstructed
v	Computed	Reconstructed
w	Computed	Reconstructed
ρu	Reconstructed	Computed
ρv	Reconstructed	Computed
ρw	Reconstructed	Computed
ρE	Reconstructed	Computed
$\rho \varepsilon$	Computed	Computed
p	Computed	Reconstructed
T	Computed	Computed
ρ	Computed	Computed

Table 4.1: Reconstruction methodologies

$$
\textit{FLAMENCO SOLVER} \downarrow
\begin{cases}
\rho|_{Comp.} = \rho_1 z_1|_{Recnst.} + \rho_2 z_2|_{Recnst.} \\
z_2|_{Comp.} = 1 - z_1|_{Recnst.} \\
\rho u|_{Comp.} = \rho|_{Comp.}\, u|_{Recnst.} \\
\rho v|_{Comp.} = \rho|_{Comp.}\, v|_{Recnst.} \\
\rho w|_{Comp.} = \rho|_{Comp.}\, w|_{Recnst.} \\
\rho E|_{Comp.} = \dfrac{z_1|_{Recnst.} + z_2|_{Comp.}}{\gamma_{Comp.} - 1}\, p|_{Recnst.} \\
\qquad\qquad + \frac{1}{2}\, \rho|_{Comp.} \left(u|^2_{Recnst.} + v|^2_{Recnst.} + w|^2_{Recnst.} \right) \\
T|_{Comp.} = \dfrac{p|_{Recnst.}}{R\, \rho|_{Recnst.}}
\end{cases}
\tag{4.12}
$$

4.2.3 Reconstruction Schemes

The final strategy is the Adaptive Reconstruction Scheme. As mentioned in the Chapter 1, the evolution of acoustic waves within the jet injector leads to a complex configuration with transversal pressure waves bouncing on the walls while increasing their intensity. In particular, their interaction with expansion waves coming from the outlet of the duct produces large confined packages of energy close to the walls. In an attempt to decrease the intensity of this phenomenon, a dissipative Adaptive Reconstruction Scheme acting

on the last three cells of the domain is employed only at the walls. There are three main reasons leading to this way of proceeding. Firstly, dissipation can be incremented in a natural way by decreasing the reconstruction order. Secondly, lowering the order implies using less halo cells, so the error associated with fictitious grid points is minimised. Thirdly, the impact on the boundary layer must be minimised not only by involving as few cells as possible, but also by implementing changes in a smooth fashion. At this point, is important to remark that this method is specific for this problem and is restricted to a very small region of the computational domain. Its utilisation in other cases must be explored carefully, paying special attention to the accuracy required for the boundary layer.

The idea behind the Adaptive Reconstruction Scheme is basically to switch gradually from the 5^{th} Order reconstruction to a 1^{st} Order scheme passing through a 2^{nd} Order method, as explained in system (4.13). This strategy satisfies the above mentioned criteria, yielding small errors if the first three cells are defined sufficiently close to the wall.

Adaptive Reconstruction Scheme

$$
\begin{array}{cll}
 & 1^{st}\ Cell & 1^{st}\ Order\ Reconstruction \begin{cases} \overline{U}^{L}_{i-\frac{1}{2}} = \overline{U}_{i-1} \\ \overline{U}^{R}_{i-\frac{1}{2}} = \overline{U}_{i} \end{cases} \\
Distance & & \\
to & 2^{nd}\ Cell & 2^{nd}\ Order\ Minmod \\
Wall & & \\
 & 3^{rd}\ Cell & 5^{th}\ Order\ Reconstruction\ (WENO/MLP) \\
\downarrow & &
\end{array}
\tag{4.13}
$$

4.3 TVD vs WENO reconstruction

4.3.1 Reconstruction features

This section is dedicated, on the one hand, to demonstrate the contribution of the Adaptive Reconstruction Scheme to enhance acoustic wave dissipation at the walls, and on the other hand, to show the effect of the Enhanced Explicit Runge-Kutta scheme when applied in conjunction with the reconstruction method.

In order to show the performance and impact of the Adaptive Reconstruction Scheme, let consider the jet injector tube of the Dry Low NOx GTU combustor defined between X = -0.0258 m and X = 0 m with a radius equal to 0.0027 m. When this approach is applied at the walls, an additional error is introduced, acting as a source of dissipation. In this way, the energy associated with the transversal bouncing waves is not completely transferred to reflected waves, but rather partially dissipated. To illustrate this idea, Figure 4.2 shows a

small portion of the tube close to the wall where the difference between radial convective fluxes obtained with and without the Adaptive Scheme are depicted. In particular, the magnitude considered in both cases to compute the difference is the radial convective flux through cell interfaces parallel to the wall. Since this magnitude is representative of the intensity of bouncing acoustic waves (it includes both momentum and pressure), and high values are associated with high values of pressure, the Adaptive Scheme should decrease such intensity. Indeed, as seen in Figure 4.2, the transported flux is significantly reduced by using the Adaptive Scheme (note that a net difference of 10^{-5} in this case is approximately 5% of the absolute transported flux), supporting the idea that the new approach works as expected.

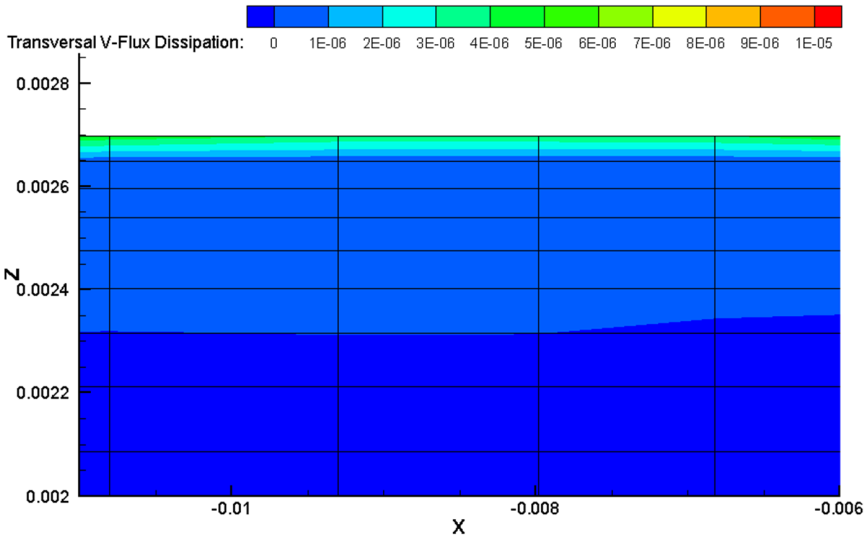

Figure 4.2: Difference between radial convective flux through cell interfaces parallel to the wall computed with and without Adaptive Reconstruction Scheme

As could not be otherwise, the fact that 5^{th} Order reconstruction is not always employed if the Adaptive Scheme is used has implications on the accuracy close to the wall, particularly in the boundary layer. According to Figure 4.3, where axial velocity profiles obtained with and without the Adaptive Scheme are shown close to the upper wall, there is a significant difference in accuracy when capturing the boundary layer, mainly in cells where the reconstruction scheme differs. As expected, the Adaptive Scheme case where 1^{st}, 2^{nd}, and 5^{th} Order are employed produces more dissipation, leading to a greater effective viscosity. To associate this idea with what is represented in Figure 4.3, just consider the incompressible 2D mass and momentum equations close to the wall

$$\frac{\partial u}{\partial x}+\frac{\partial v}{\partial z}=0 \tag{4.14}$$

$$u\frac{\partial u}{\partial x}+v\frac{\partial u}{\partial z}\approx-\frac{1}{\rho}\frac{\partial p}{\partial x}+\frac{\mu}{\rho}\frac{\partial^2 u}{\partial z^2} \tag{4.15}$$

At very small distances, in can be approximate

$$\frac{\partial u}{\partial x}+\frac{\partial v}{\partial z}=0 \longrightarrow \frac{\Delta u}{\Delta x}\sim\frac{\Delta v}{\Delta z}\longrightarrow \Delta v\sim\frac{\Delta z}{\Delta x}\Delta u \tag{4.16}$$

$$u\frac{\Delta u}{\Delta x}\sim u\frac{\Delta v}{\Delta z}\longrightarrow u\frac{\partial u}{\partial x}\sim v\frac{\partial u}{\partial z} \tag{4.17}$$

and both terms in the left hand side of equation (4.15) are of the same order of magnitude. Now, bearing in mind that the Adaptive Reconstruction Scheme only affects the reconstruction in the z coordinate, the second term of the LHS of (4.15) can be approximate by 1^{st} Order reconstruction as

$$v\left.\frac{\partial u}{\partial z}\right|_{z-\Delta z}\approx v\left(\left.\frac{\partial u}{\partial z}\right|_{z}-\left.\frac{\partial^2 u}{\partial z^2}\right|_{z}\Delta z+o\left(\Delta z^2\right)\right) \tag{4.18}$$

Introducing this last expression in a discretised form of (4.15)

$$u\left.\frac{\partial u}{\partial x}\right|_{z}+v\left.\frac{\partial u}{\partial z}\right|_{z}\approx-\frac{1}{\rho}\left.\frac{\partial p}{\partial x}\right|_{z}+\left(\frac{\mu}{\rho}+v\Delta z\right)\left.\frac{\partial^2 u}{\partial z^2}\right|_{z}+o\left(\Delta z^2\right) \tag{4.19}$$

and therefore viscosity is effectively incremented, yielding a lower peak velocity with the distribution shown in Figure 4.3. It should be noted that this analysis is valid only for laminar flows, but gives a rough idea of the causes behind such behaviour. Obviously, for finer meshes the algorithm will see accuracy increased.

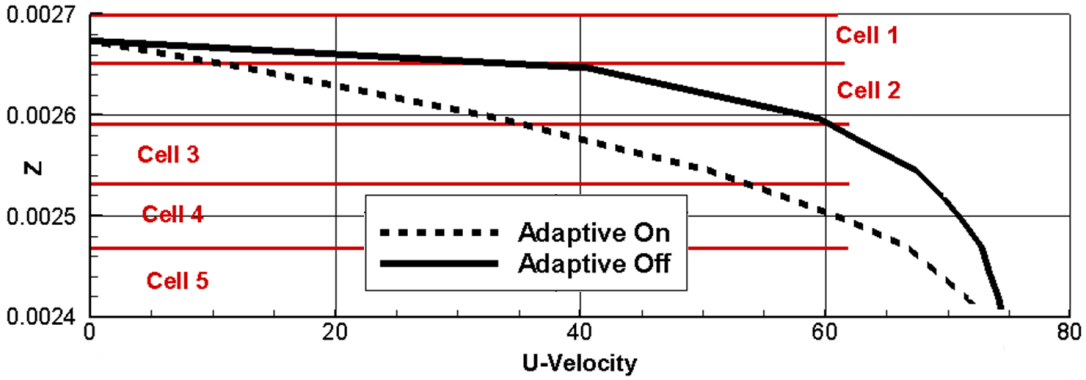

Figure 4.3: Axial velocity profiles at the wall for computations set with and without the Adaptive Reconstruction Scheme. Cells 1 to 5 are indicated in red

The Adaptive Reconstruction Scheme has a collateral benefit that, while not relevant for the Dry Low NOx GTU combustor case where viscosity is accounted, is extremely important in problems where only convective flows are considered. Indeed, if reconstruction at an inviscid wall is performed using any of the 5^{th} Order schemes alone, a non-zero velocity normal to the interface appears, introducing non-zero mass fluxes.

However, if the Adaptive Reconstruction Scheme is employed instead, such velocity is 0 and so are the fluxes, yielding a physically consistent algorithm. To proof this assertion, first consider WENO and MLP formulations from systems (3.43)-(3.47) and (3.50)-(3.51) respectively. If above schemes are applied to a cylindrical geometry like the one represented in Figure 4.4 with inviscid walls, an unphysical reconstruction is produced. Let considered the values shown in Table 4.2 for the involved variables. Note that Rev. indicates that the component is reversed from the associated one inside the domain, Param. that it is taken as variable parameter and n_x, n_y and n_z are the components of the unitary normal to the wall.

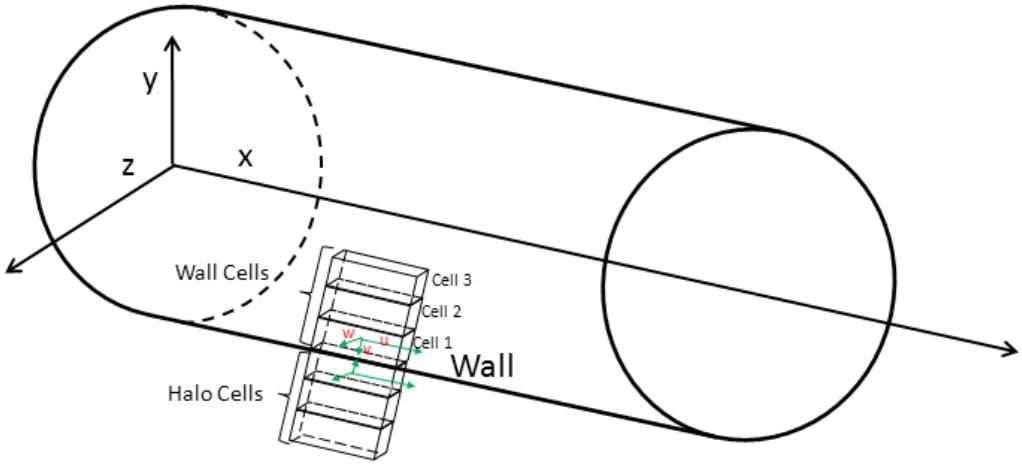

Figure 4.4: Cylindrical tube. Walls are "inviscid" (only normal component of velocity is reversed)

	Cell 1	**Cell 2**	**Cell 3**	**Halo 1**	**Halo 2**	**Halo 3**		
u	70 m/s	70 m/s	70 m/s	70 m/s	70 m/s	70 m/s	$\mathbf{n_x}$	0
v	Param.	Param.	0.2 m/s	Rev. Cell 1	Rev. Cell 2	Rev. Cell 3	$\mathbf{n_y}$	$\frac{1}{\sqrt{2}}$
w	0	0	0	Rev. Cell 1	Rev. Cell 2	Rev. Cell 3	$\mathbf{n_z}$	$\frac{1}{\sqrt{2}}$

Table 4.2: Characteristic values for reconstruction near the inviscid wall

To get zero mass fluxes through the wall, both Left and Right reconstructed velocity values normal to it must have the same absolute value with opposite sign, as deduced from the solution of the Local Riemann Problem (to get zero mass flux we need zero normal velocity at the wall, which can only be achieved if Left and Right values are equal in magnitude but opposite in sign). For the values above, Left and Right reconstructed normal velocities in the TVD-MLP and WENO cases are plot in Figure 4.5 (note that the Right state is represented with changed sign). As seen, for small variations of the perpendicular velocity (between 0.1 and 0.5 m/s), Left and Right values not only are different, but the disparity is of the order of the velocity itself.

In the case of having axial velocity only (v = 0, w = 0) the reconstruction provides the correct values. However, as soon as external perturbations introduce transversal velocity components (i.e. numerical diffusion, conditions at the tube exit, etc.), the reconstruction method will effectively produce non-zero fluxes. This is corrected with the Adaptive Reconstruction Scheme expressed in (4.13), and therefore its use remains justified.

In another issue, the Enhanced Explicit Runge-Kutta is necessary to prevent unphysical values of volume fraction. This is clearly visible in Figures 4.6 - 4.10, where volume fraction reconstruction has been represented for Left and Right states of both schemes (MLP-Left, MLP-Right, WENO-Left, WENO-Right). Figure 4.6 shows volume fraction at a discontinuity. The values are stored by cells ranging from $i-3$ to $i+2$, so the reconstruction can be performed at interface $i-\frac{1}{2}$. As seen, both methods agree in reconstructing Left and Right states (WENO scheme introduces a negligible deviation from 0, showing that it is not completely "non-oscillatory") and consistent physical magnitudes are yielded.

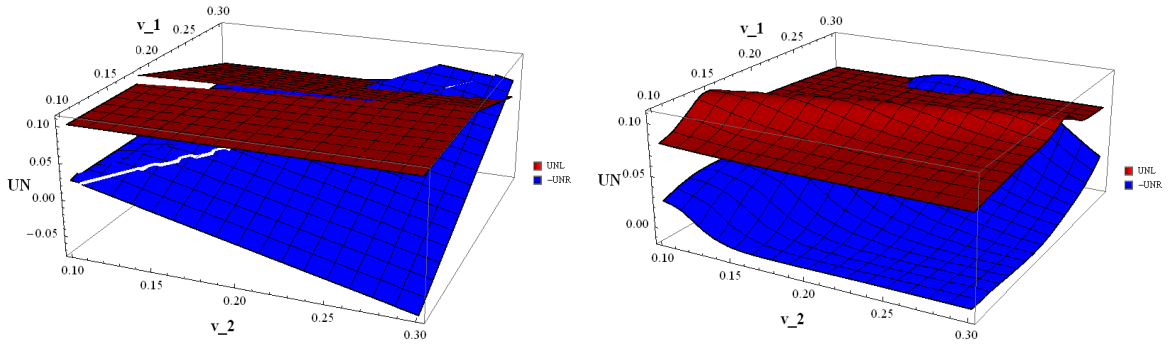

(a) TVD-MLP Reconstruction **(b)** WENO Reconstruction

Figure 4.5: Reconstruction of velocity perpendicular to the wall. v_1 and v_2 refer to cell 1 and cell 2 respectively

However, Figure 4.7 evidences the above mentioned idea that it is possible for both schemes to take forbidden values of volume fraction. This figure was composed similarly to the previous one, where a discontinuity is present at $i-\frac{1}{2}$ (i.e. two fluids initially separated, or a pure species moving towards another species). If a small perturbation, say a numerical error, alters the distribution in the same fashion as shown in Figure 4.7 (not necessarily such values, but the one stored in cell $i+1$ needs to be lower than the ones stored in cells i and $i+2$ to provide erroneous reconstruction), then Right WENO and TVD-MLP states go slightly above 1, which is completely unphysical. At this point, if volume fraction equal 1 is taken instead, which is exactly what the Enhanced Explicit Runge-Kutta does, the process becomes physically and numerically consistent without sensitively decreasing the order of accuracy. In the same way, Figures 4.8 and 4.9 show two situations where, either the TVD-MLP or WENO scheme produces unphysical magnitudes of both Left and Right states at the same time, thus leading to unaccepted actual values at the interface (note that if only one state is unphysical, the flux

TVD-MLP Left	0.
TVD-MLP Right	1.
WENO Left	1.305×10^{-30}
WENO Right	1.

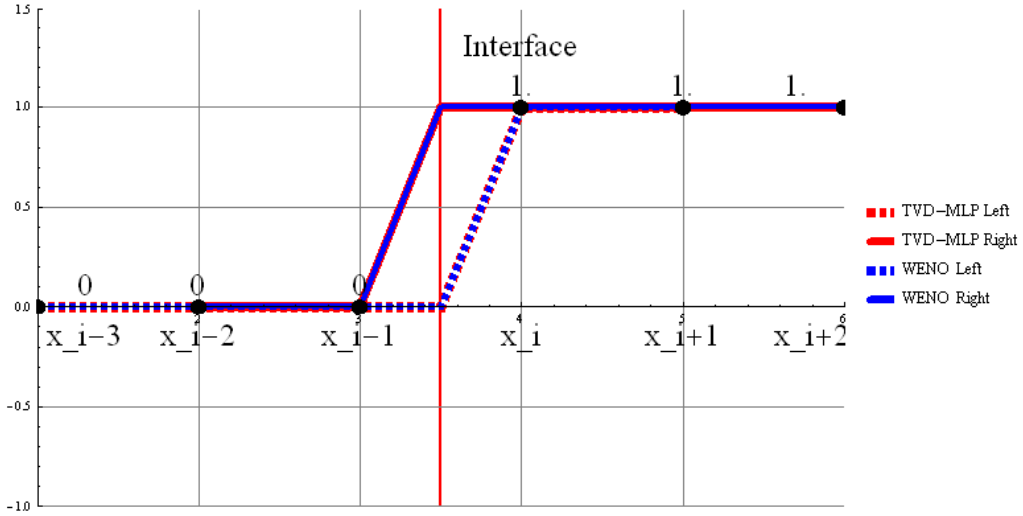

Figure 4.6: Initial volume fraction values at a discontinuity

at the interface may be based on valid magnitudes). As seen, whereas Figure 4.8 shows that the TVD-MLP scheme has the capacity of providing wrong output even in smooth regions, Figure 4.9 suggests that the WENO method may behave erroneously in areas where discontinuities appear (this may be very dangerous, since even small perturbations can be considered "discontinuities" for this matter). Finally, it should be remarked as well that the situation where TVD-MLP or WENO produce wrong reconstructions may be completely different. Indeed, Figure 4.10 represents a particular case where a small perturbation affects the value stored at cell $i-2$ by increasing it. Here, only the Left WENO state is wrong, since it goes below 0. Since the same situation but with changed agents may occur, it is indispensable to prevent such behaviour in a general way.

TVD-MLP Left	0.
TVD-MLP Right	1.03
WENO Left	1.29483×10^{-30}
WENO Right	1.03493

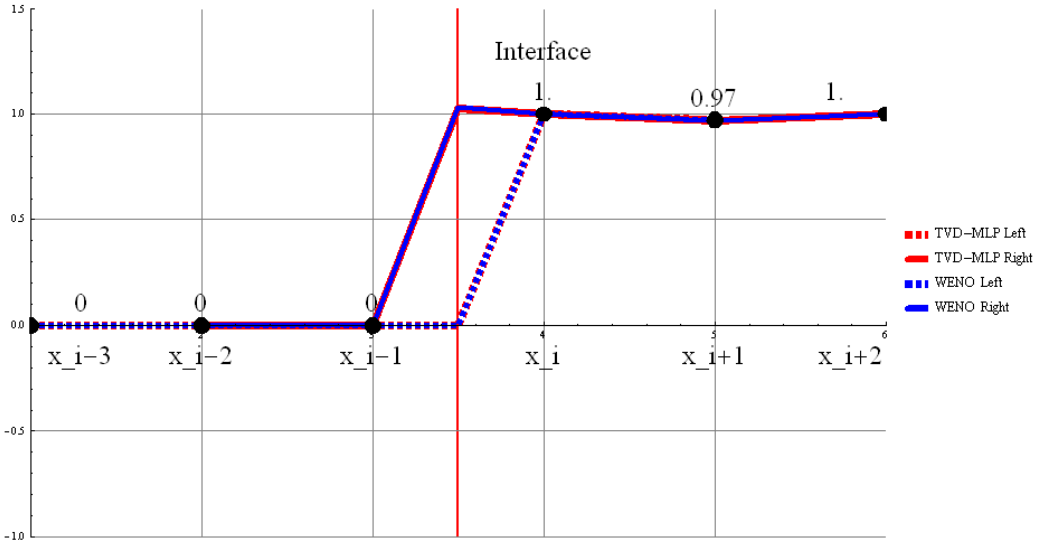

Figure 4.7: Volume Fraction reconstruction showing forbidden values for small perturbations

TVD-MLP Left	-0.132
TVD-MLP Right	-0.26
WENO Left	0.130313
WENO Right	0.134759

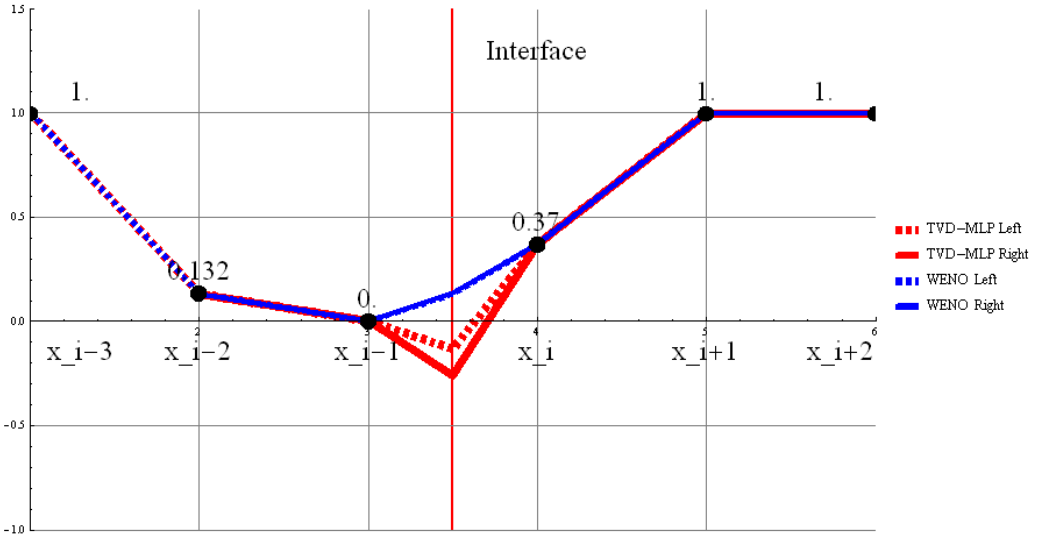

Figure 4.8: Unphysical volume fraction values reconstructed by both Right and Left states of the TVD-MLP scheme

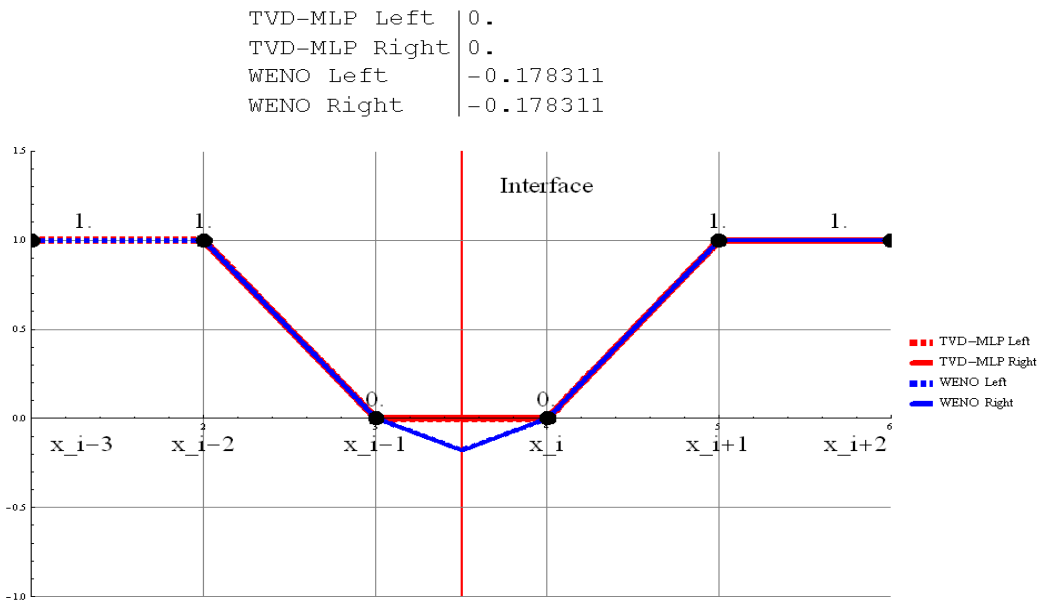

Figure 4.9: Unphysical volume fraction values reconstructed by both Right and Left states of the WENO scheme

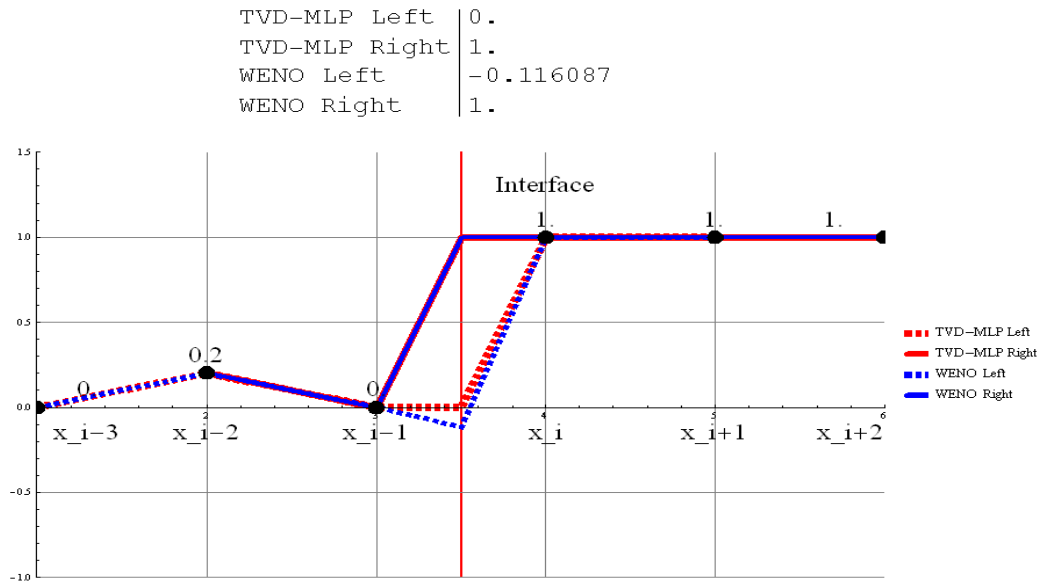

Figure 4.10: Case where only WENO Reconstruction provides wrong results

In all cases above, it is clear that the corrected reconstructions and subsequent time integration control proposed by the Enhanced Explicit Runge-Kutta keep the problem physically and numerically consistent without altering in any way the order of accuracy of the whole model. Therefore, the use of this method is considered essential to produce realistic simulations.

4.3.2 Validation and accuracy

The validation of both reconstruction strategies working in conjunction with the Enhanced Explicit Runge-Kutta scheme must be validated prior to further applications. From a general point of view, the methodology employed to include viscous and source terms has been deeply validated in Pulliam et al. [69] (and references therein). Hence, only inviscid flows are considered for the validation in this research.

In order to cover a broad range of situations, six test cases have been taken for comparison, namely the Stationary Contact Wave, Moving Contact Wave, Shock Tube, Kelvin-Helmholtz Instability and 2D and 3D Explosion Problems. With this selection, unsteady and steady features in all dimensions are tested. Additionally, theoretical solutions are available for 5 out of the six cases. In the Kelvin-Helmholtz Instability problem, contrasted numerical data is taken to compare with.

Stationary Contact Wave

The Stationary Contact Wave problem, as presented here for multispecies flows, consists of two different fluids initially separated by a shared interface. These fluids, referred as Left and Right flows, have different properties and are set with different thermodynamic conditions in order to create a contact wave at the interface. Table 4.3 describes the initial set up for this problem, the numerical conditions (i.e. grid resolution, type of grid, etc.) and the output time. In this case, the expected behaviour is a stationary evolution, forcing the contact wave to remain in the same position without any variation in time.

Features	- 2^{nd} Order Minmod, 5^{th} Order WENO, 5^{th} Order TVD-MLP			
	- 2^{nd} Order 4-Stages Enhanced Explicit Runge-Kutta			
Initial Set-up	**Left**	$p_L = 101325\ Pa$	$\rho_L = 0.2\ Kg/m^3$	$\gamma_L = 1.4$
		$u_L = 0\ m/s$	$v_L = 0\ m/s$	$w_L = 0\ m/s$
	Right	$p_R = 101325\ Pa$	$\rho_R = 1.225\ Kg/m^3$	$\gamma_R = 1.2$
		$u_R = 0\ m/s$	$v_R = 0\ m/s$	$w_R = 0\ m/s$
Sim. Config.	**CFL**	2^{nd} Order Minmod	0.4	
		5^{th} Order WENO	1.0	
		5^{th} Order TVD-MLP	0.4	
Grid	**Desc.**	- Prism geometry. All BC set as Inviscid Walls		
	Size	100x3x3 Cells		
Output	**Time**	$5.937 \cdot 10^{-3}$ s		

Table 4.3: Stationary Contact Surface test case

This benchmark problem not only tests the ability of the reconstruction scheme to deal with static discontinuities in the flow, but it also checks the behaviour of the HLLC Approximate Riemann solver and its capacity to deal with contact waves. Additionally,

the control of numerical diffusion is analysed, since the interfaces must not be smeared in time, leaving a mixture region with constant thickness. Essentially, it can be fairly said that the Stationary Contact Wave tests the behaviour of the convective and time integration solvers and the capacity to minimise and bound numerical errors.

Figure 4.11 shows four characteristic variables at the output time indicated in Table 4.3 above, which is considered large enough to allow numerical perturbations if the model was not well posed. In all plots, results generated with the 2^{nd} Order Minmod, 5^{th} Order TVD-MLP and 5^{th} Order WENO are compared with the theoretical solution. As seen in Figure 4.11a, Pressure is kept perfectly constant through the discontinuity, which evidences the effect of the isobaric closure. In the same way, velocity is also kept constant supporting this idea. As for density and volume fraction 1, the ability of the HLLC Approximate Riemann solver selected to capture contact discontinuities is clearly visible, indicating proper implementation of the approach. Finally, all models perform well in this case, since the interface is not smeared at all. This result was expected, since advection (velocities) are null.

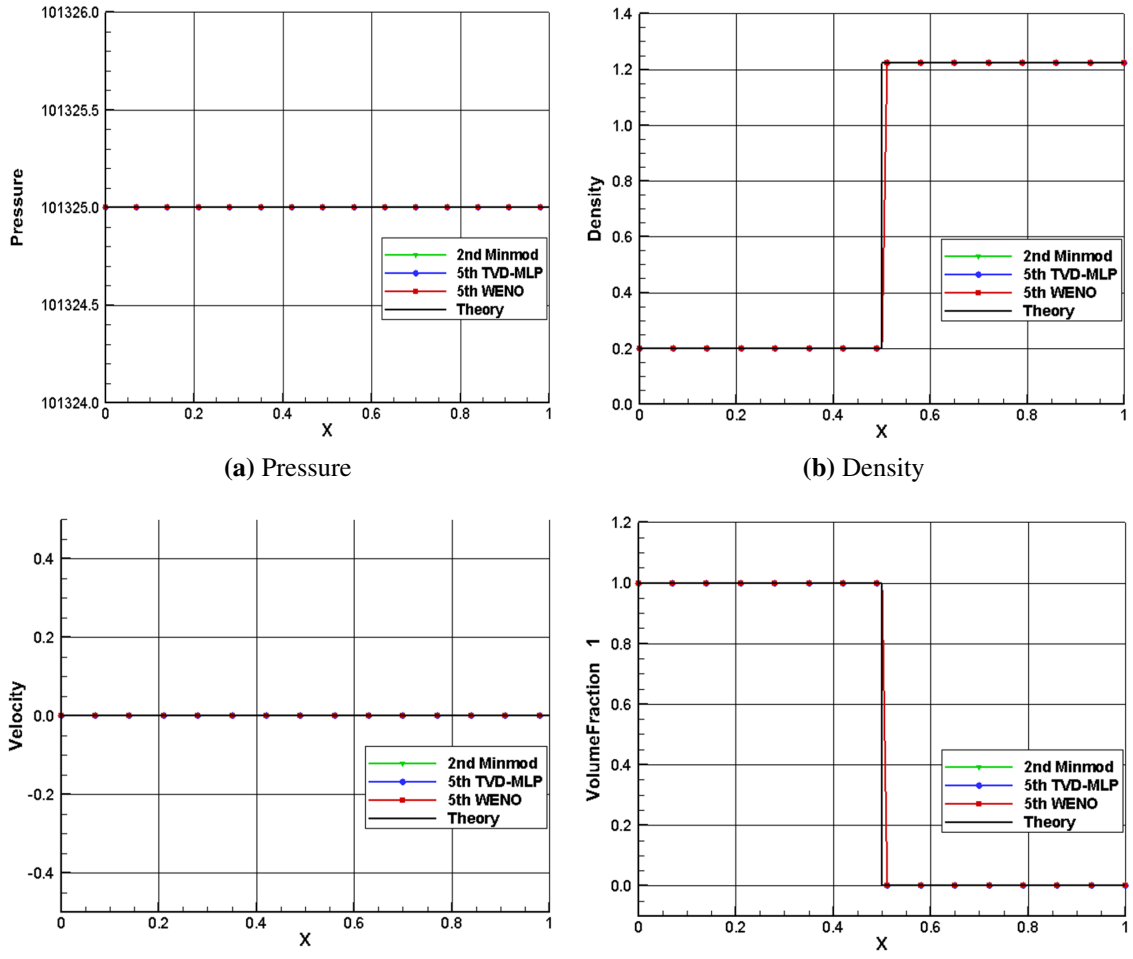

(a) Pressure

(b) Density

(c) Velocity

(d) Volume Fraction 1

Figure 4.11: Characteristic variables of the Stationary Contact Wave problem

Moving Contact Wave

This case is quite similar to the previous one, with the difference that here both flows are initially set with equal velocity. This problem is useful to test both convective and diffusion terms, since the initial configuration must be advected but not smeared (note that the small layer generated by numerical diffusion is treated as a mixture layer). Although the HLLC solver is fully validated only if sonic and supersonic cases are performed, here just the supersonic case is considered here for simplicity. However, it must be mentioned that the subsonic case was also analysed during the developing process of FLAMENCO. The initial set-up of the Moving Contact Wave problem is indicated in Table 4.4. As seen, four output times have been selected in order to show the evolution of the contact discontinuity and how it is capture by all schemes

Features	- 2^{nd} Order Minmod, 5^{th} Order WENO, 5^{th} Order TVD-MLP			
	- 2^{nd} Order 4-Stages Enhanced Explicit Runge-Kutta			
Initial Set-up	**Left**	$p_L = 101325\ Pa$	$\rho_L = 0.2\ Kg/m^3$	$\gamma_L = 1.4$
		$u_L = 700\ m/s$	$v_L = 0\ m/s$	$w_L = 0\ m/s$
	Right	$p_R = 101325\ Pa$	$\rho_R = 1.225\ Kg/m^3$	$\gamma_R = 1.2$
		$u_R = 700\ m/s$	$v_R = 0\ m/s$	$w_R = 0\ m/s$
Sim. Config.	**CFL**	2^{nd} Order Minmod	0.4	
		5^{th} Order WENO	1.0	
		5^{th} Order TVD-MLP	0.4	
Grid	**Desc.**	- Prism geometry. Supersonic Inlet and Outlet Remaining BC set as Inviscid Walls		
	Size	100x3x3 Cells		
Output	**Time**	$1.6211 \cdot 10^{-4}$ s		
		$3.2422 \cdot 10^{-4}$ s		
		$4.8633 \cdot 10^{-4}$ s		
		$6.4843 \cdot 10^{-4}$ s		

Table 4.4: Moving Contact Surface test case

Figure 4.12 depicts again pressure, density, velocity and volume fraction at the output times indicated. Again, pressure and velocity are perfectly constant for all cases, denoting accurate and non-oscillatory behaviour for non-zero convective fluxes. Regarding density and volume fraction, here the performance of each scheme is well noted. Firstly, it draws attention the great temporal accuracy achieved by all methods, which highlights the potential of the 2^{nd} Order 4-Stages Runge-Kutta approach. Secondly, the outstanding precision shown during the whole evolution, where only the 2^{nd} Order Minmod reconstruction yields errors that increase slightly over time, suggests that both 5^{th} Order methods are not only extremely accurate, but also very stable and extremely low dissipative (in fact, this last feature is largely responsible for the Low Dissipation issue addressed in this work). A close view of all reconstructions is plotted in Figure 4.13, where the left and right sides of the discontinuity (boundaries of the mixture region) are

zoomed. Comparing with the exact solution (it is not totally exact, since it was produced using a 1^{st} Order scheme in a very fine mesh), it can inferred that the best results are provided by the 5^{th} Order TVD-MLP method, followed closely by the WENO one and quite far from those generated by the 2^{nd} Order Minmod. In light of these results, it can be fairly said that the TVD-MLP is the less dissipative scheme, reconstructing the flow field with high level of fidelity. Finally, although not as accurate, the theoretical curve is also well fitted by the WENO model, making of it a good candidate to be used in the Dry Low NOx GTU combustor case (an advantage here is the higher dissipation produced within the jet duct).

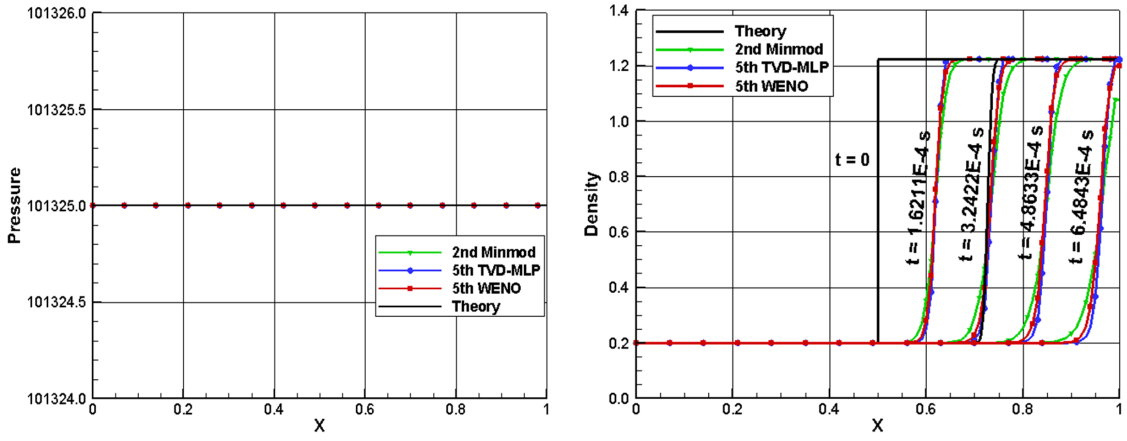

(a) Pressure

(b) Density

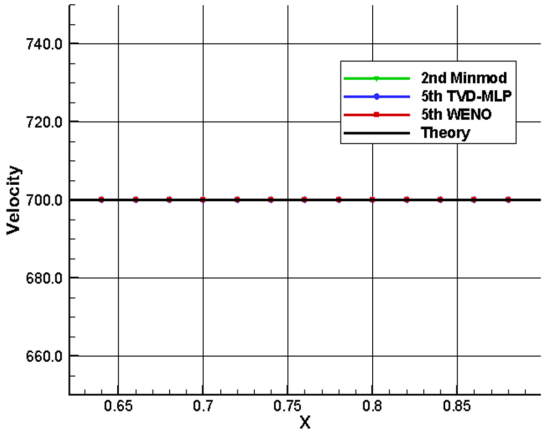

(c) Velocity

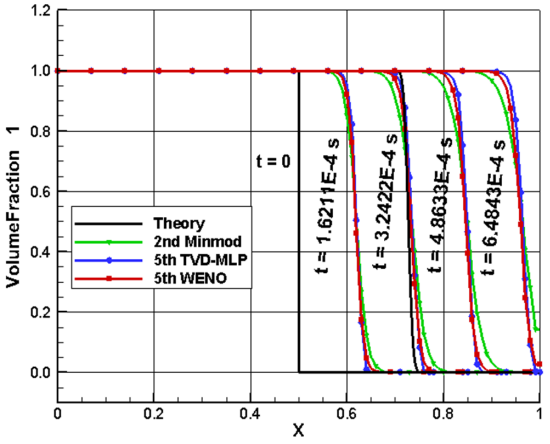

(d) Volume Fraction 1

Figure 4.12: Characteristic variables of the Moving Contact Wave problem at different output times

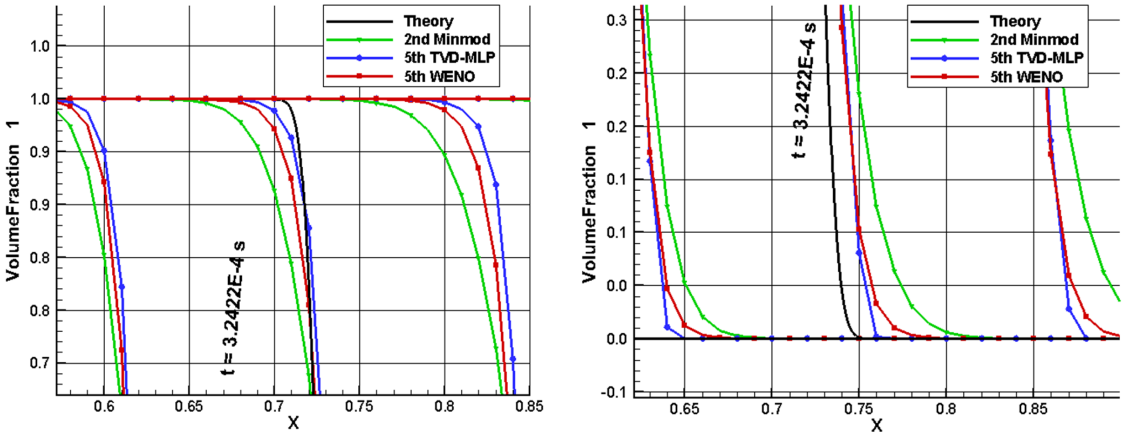

(a) Left side of the discontinuity

(b) Right side of the discontinuity

Figure 4.13: Close view of the contact discontinuity

Shock Tube

This benchmark problem is an extremely valuable test case for numerical validation of algorithms dealing with compressible flows. Its importance lies on the fact that all information waves present in the Local Riemann Problem developed at each point of the fluid domain (in the case of Finite Volume methods at each cell interface) are reproduced and tracked. Hence, the Shock Tube problem is defined in such a way that shock, rarefaction and contact waves depart from an initial unstable configuration. For this purpose, Table 4.5 indicates the initial values used here for subsonic evolution as well as some information about the set up.

Features	- 2^{nd} Order Minmod, 5^{th} Order WENO, 5^{th} Order TVD-MLP			
	- 2^{nd} Order 4-Stages Enhanced Explicit Runge-Kutta			
Initial Set-up	**Left**	$p_L = 1.0\ Pa$	$\rho_L = 1.0\ Kg/m^3$	$\gamma_L = 1.2$
		$u_L = 0\ m/s$	$v_L = 0\ m/s$	$w_L = 0\ m/s$
	Right	$p_R = 0.1\ Pa$	$\rho_R = 0.1225\ Kg/m^3$	$\gamma_R = 1.4$
		$u_R = 0\ m/s$	$v_R = 0\ m/s$	$w_R = 0\ m/s$
Sim. Config.	**CFL**	2^{nd} Order Minmod	0.4	
		5^{th} Order WENO	1.0	
		5^{th} Order TVD-MLP	0.4	
Grid	**Desc.**	- Prism geometry. All BC set as Inviscid Walls		
	Size	100x3x3 Cells		
Output	**Time**	0.1158 s		
		0.2317 s		

Table 4.5: Shock Tube test case

Due to the great utility of this simple test case, where all features possibly developed in

further applications are found, the Shock Tube problem has been extensively studied in the literature. For the sake of comparison, results from [7] are reproduced and compared, aiming to analyse the advantages and disadvantages of the models proposed. Although several set ups can be studied (supersonic waves, great disparity in the heat capacity ratio, etc.) the case selected here is general enough to be considered as representative of a real situation.

First of all, Figure 4.14 illustrates the flow field at t = 0.1158 s. It is interesting to see on the one hand how the left rarefaction wave, where the evolution is smooth, is perfectly captured by all approaches and on the other hand how both contact and shock waves are slightly smeared. In particular, the right shock wave is the one that seems to be more smeared, again with the TVD-MLP performing the best. Looking at the left end of the rarefaction wave, shown in detail in Figure 4.15a, both the TVD-MLP and WENO schemes have similar accuracy, significantly better than the one associated with the Minmod. It should be noted as well the high temporal accuracy achieved, consequence of the 2^{nd} Order time integration scheme.

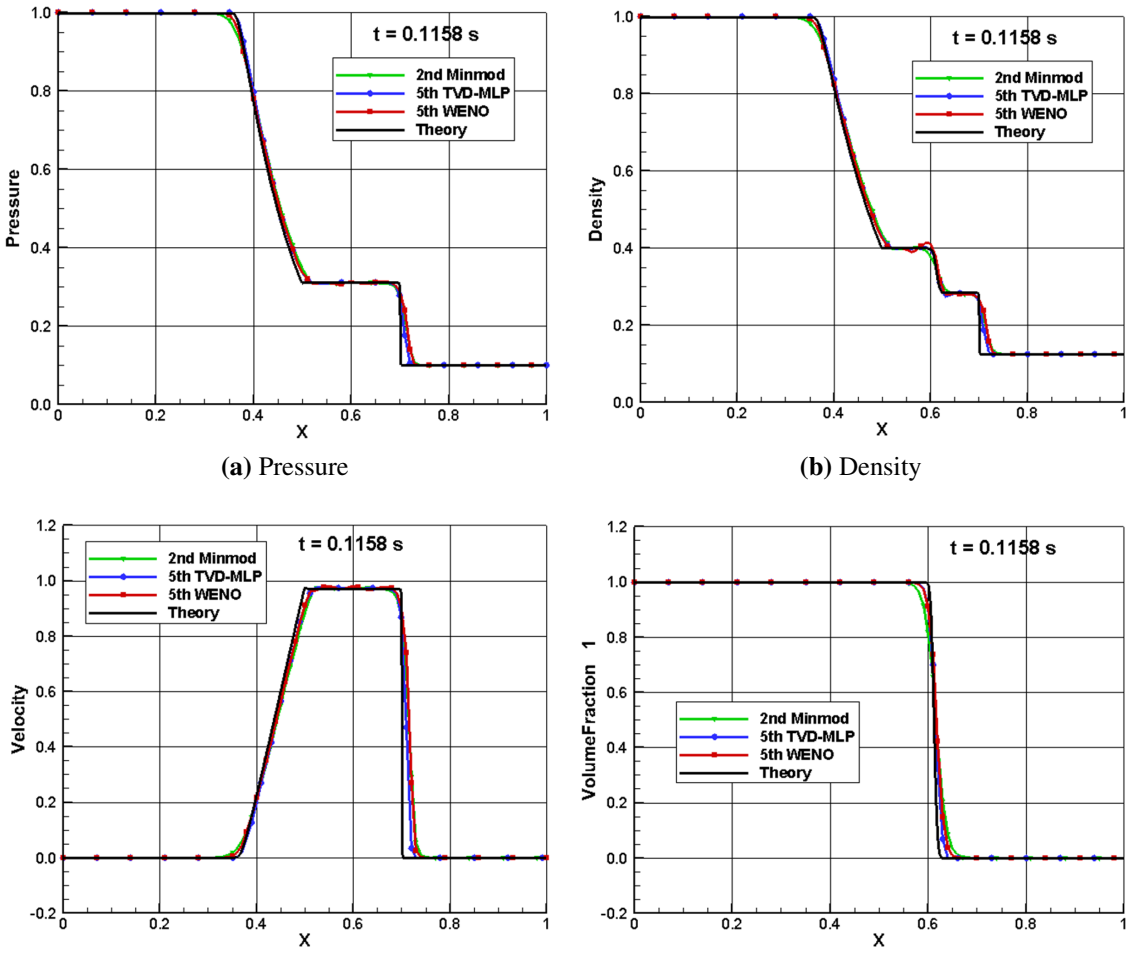

(a) Pressure

(b) Density

(c) Velocity

(d) Volume Fraction 1

Figure 4.14: Characteristic variables of the Shock Tube problem at t = 0.1108 s

It draws attention in Figure 4.14b, density plot, small oscillations in the WENO solution. Indeed, as depicted in Figure 4.15b, an oscillatory behaviour is mainly exhibited in the surroundings of the contact wave. This is a direct consequence of the mathematical definition pointed out in Section 4.3.1, where the slightly oscillatory performance of the WENO scheme was demonstrated. Although much less important, the TVD-MLP also presents a small undershot at the right end of the contact discontinuity. This unwanted behaviour is in both cases damped over time, as shown in Figure 4.16b and Figure 4.17.

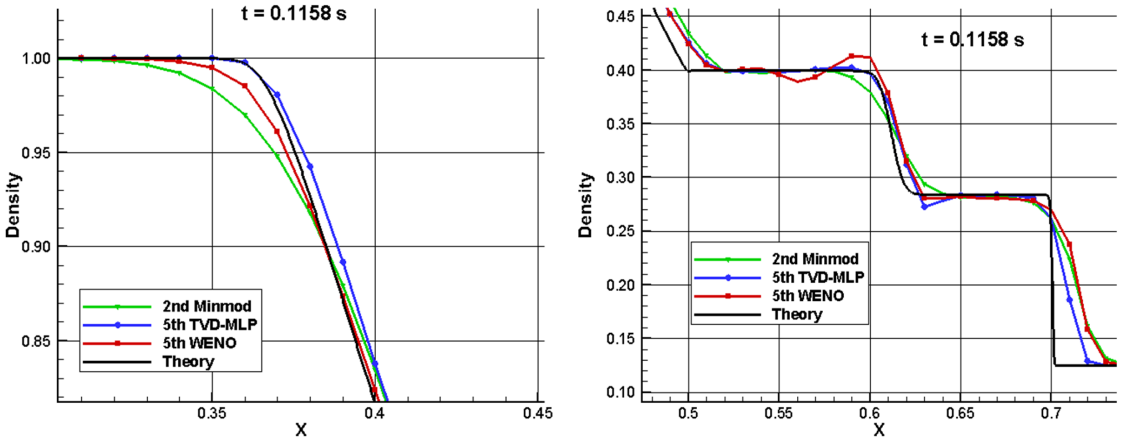

(a) Left end of the rarefaction wave

(b) Contact and shock wave in detail

Figure 4.15: Close view of the rarefaction, contact and shock wave in the Shock Tube test problem at t = 0.1158 s

Same variables are plotted in Figure 4.16 at t = 0.2317 s. At this point, the oscillations have been almost totally damped and the theoretical curve is well fitted at both discontinuities and at the rarefaction wave. Here, same trend is followed, with the TVD-MLP and WENO having similar accuracy and better than the Minmod scheme. Again, the TVD-MLP is slightly better than the WENO, specially in the shock wave vicinity. All these conclusions are visible in Figure 4.17, where a close view of both density discontinuities is represented. As stated, here the oscillations are almost damped and the solution is really accurate for such a coarse grid.

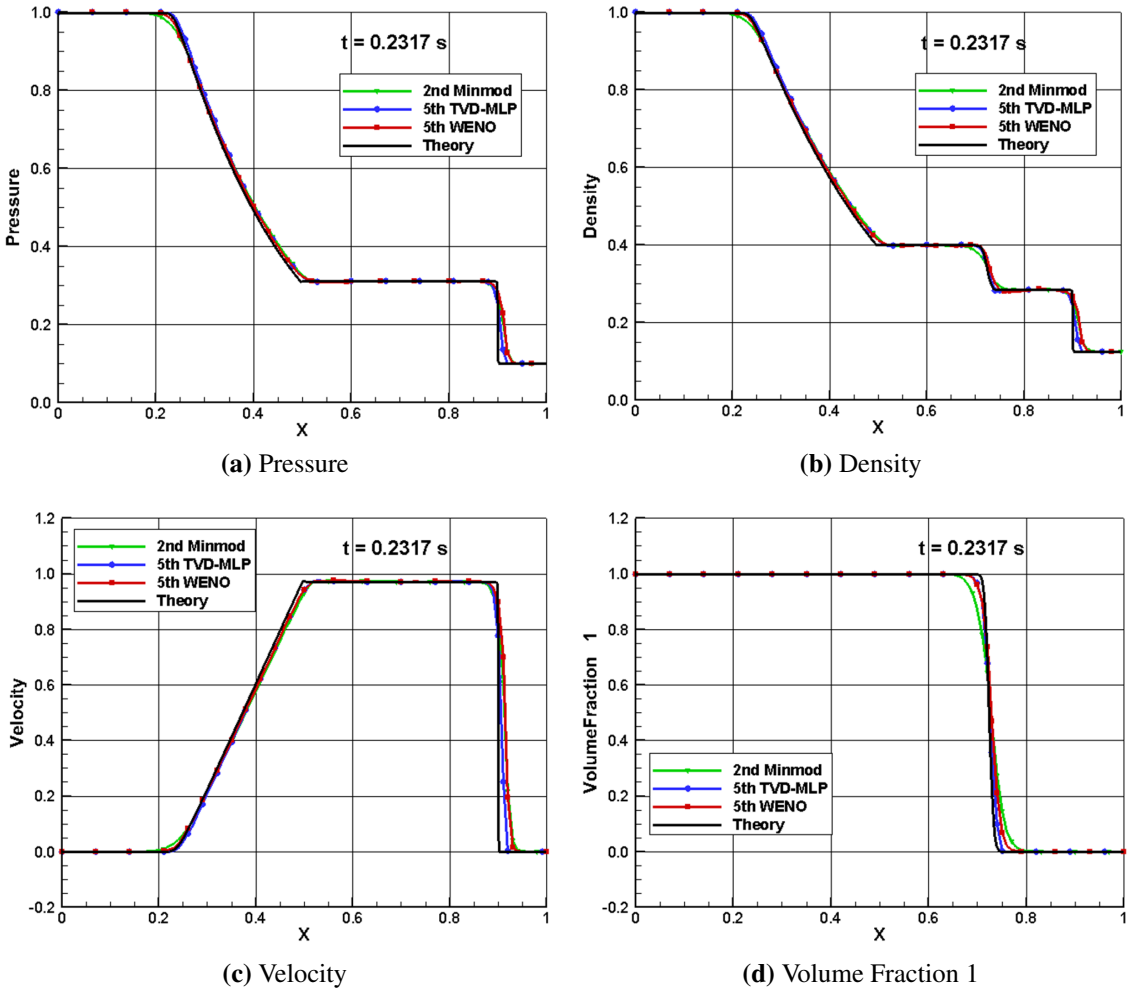

(a) Pressure

(b) Density

(c) Velocity

(d) Volume Fraction 1

Figure 4.16: Characteristic variables of the Shock Tube problem at t = 0.2317 s

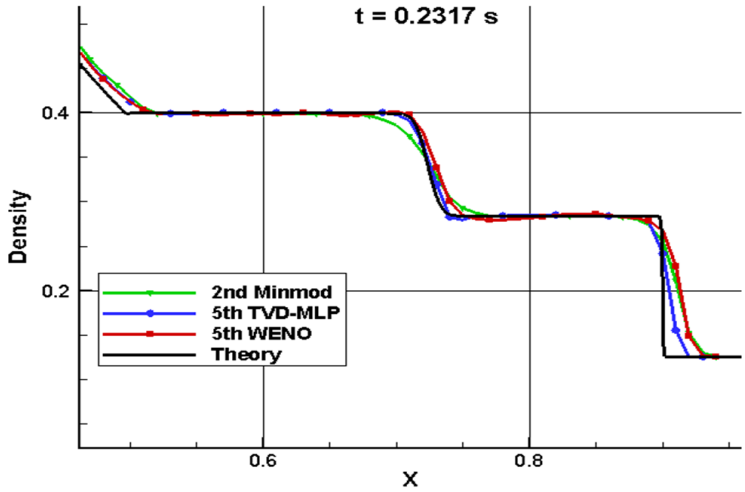

Figure 4.17: Close view of the contact and shock wave in the Shock Tube test problem at t = 0.2317 s

Kelvin-Helmholtz Instability

This well-know problem is chosen for two main reasons. Firstly, besides testing the convective fluxes again, it is very important to see the evolution of the mixture layer over time, produced as a consequence of the numerical error. This allows checking the performance in an extremely coarse grid of the mixture model implemented, which must provide sensible values in order to generate an accurate and stable solution. The second reason is related to the periodic conditions used, which has been included in FLAMENCO as an additional feature.

The Kelvin-Helmholtz Instability problem, as considered here, consists of two inviscid flows moving in opposite directions subjected to a central velocity perturbation (see Table 4.6 for the set up). As soon as the process begins, a central eddy is created, forcing the mixture of both fluids. The range of this eddy is increased over time, ultimately reaching the boundaries of the domain.

Features	- 2^{nd} Order Minmod, 5^{th} Order WENO, 5^{th} Order TVD-MLP			
	- 2^{nd} Order 4-Stages Enhanced Explicit Runge-Kutta			
Initial Set-up	**Left**	$M_L = 0.2$	$\rho_L = 1.0\ Kg/m^3$	$\gamma_L = \frac{5}{3}$
		$u_L = Asin(K \cdot y)\, exp(-K\lvert x\rvert)$		$A = 0.1\ K = 4\pi$
		$v_L = -U_0 - Acos(K \cdot y)\, exp(-K\lvert x\rvert)$		$U_0 = 0.5$
	Right	$M_R = 0.2$	$\rho_R = 1.0\ Kg/m^3$	$\gamma_R = \frac{5}{3}$
		$u_R = Asin(K \cdot y)\, exp(-K\lvert x\rvert)$		$A = 0.1\ K = 4\pi$
		$v_R = U_0 + Acos(K \cdot y)\, exp(-K\lvert x\rvert)$		$U_0 = 0.5$
Sim. Config.	**CFL**	2^{nd} Order Minmod	0.4	
		5^{th} Order WENO	1.0	
		5^{th} Order TVD-MLP	0.4	
Grid	**Desc.**	- Square geometry. Upper and lower BC periodic. Rest symmetry planes		
	Size	16x16x3 Cells		
Output	**Time**	3 s		

Table 4.6: Kelvin-Helmholtz test case

This benchmark case lacks of theoretical results, since its mathematical formation has no analytical solution. Thus, for the sake of comparison, results from [7] generated using a 5^{th} Order standard MUSCL approach with Low Mach correction enabled are collected. Figure 4.18 illustrates data provided by all methods at time t = 3 s. As expected, both 5^{th} Order reconstructions have larger range than the 2^{nd} Order one. At this output time, the former ones predict that both left and right flows have undergone stretching, folding over themselves in the characteristic central eddy. As for the 2^{nd} Order Minmod, the distortion has commenced but it is completely inaccurate quantitatively speaking, as concluded in light of the reference data presented in Figure 4.18a.

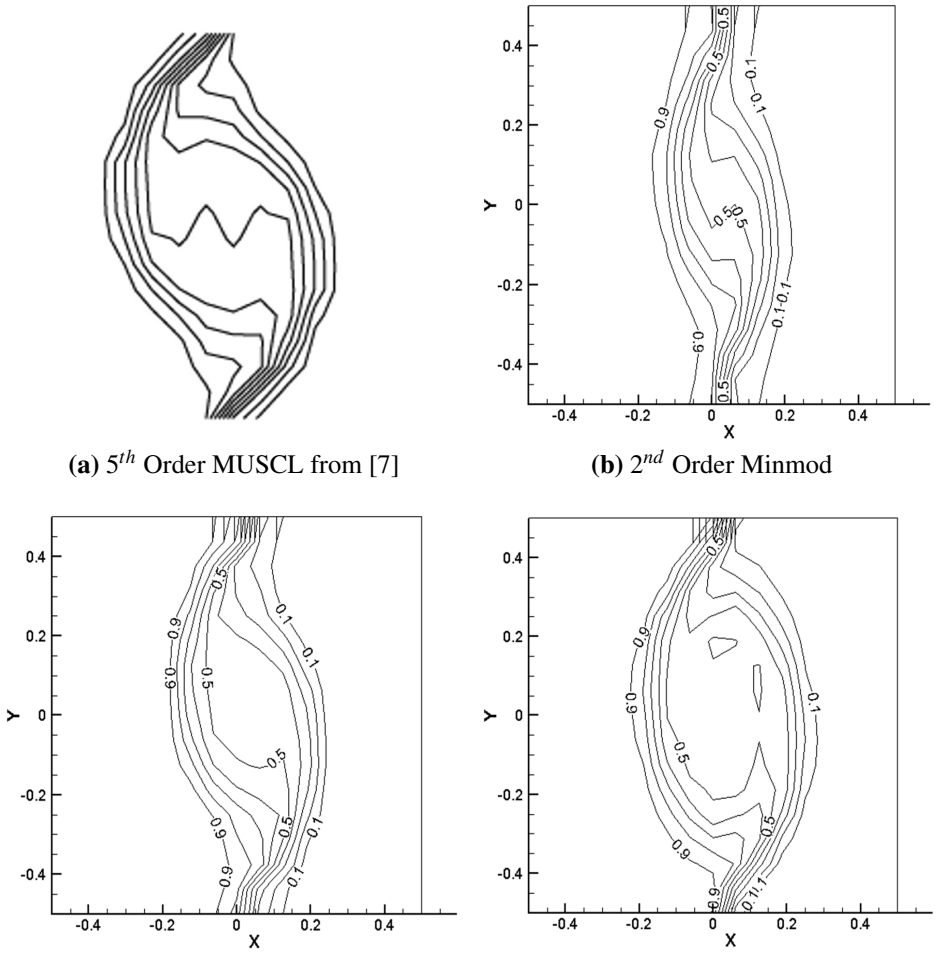

(a) 5^{th} Order MUSCL from [7]

(b) 2^{nd} Order Minmod

(c) 5^{th} Order TVD-MLP

(d) 5^{th} Order WENO

Figure 4.18: Kelvin-Helmholtz Instability results for different reconstruction schemes at t = 3 s

The mixture layer generated over time due to numerical diffusion agrees very well with previous validated data. This fact supports the idea that a well-posed mixture model with volume fraction-based quantities and iso-baric closure is suitable for convection-diffusion problems.

2D and 3D Explosion Problems

Although the 2D and 3D explosion test cases are formally similar to the Shock Tube, their ability to test two-dimensional and three-dimensional implementations simultaneously are too attractive to be ignored. In this way, an adequate performance in these problems, particularly in the 3D Explosion problem, will validate from a general point of view the implementation and methodology followed in FLAMENCO to solve convective terms. For this purpose, Table 4.7 shows the set-up in both problems.

The validation of the Unsplit Finite-Volume method with curvilinear coordinates

<table>
<tr><td rowspan="2">Features</td><td colspan="4">- 2^{nd} Order Minmod, 5^{th} Order WENO, 5^{th} Order TVD-MLP</td></tr>
<tr><td colspan="4">- 2^{nd} Order 4-Stages Enhanced Explicit Runge-Kutta</td></tr>
<tr><td rowspan="4">Initial Set-up
$r = x^2 + y^2$</td><td rowspan="2">$r \leq 0.4$</td><td>$p = 1.0\ Pa$</td><td>$\rho = 1.0\ Kg/m^3$</td><td>$\gamma = 1.4$</td></tr>
<tr><td>$u = 0\ m/s$</td><td>$v = 0\ m/s$</td><td>$w = 0\ m/s$</td></tr>
<tr><td rowspan="2">$r > 0.4$</td><td>$p = 0.1\ Pa$</td><td>$\rho = 0.125\ Kg/m^3$</td><td>$\gamma = 1.4$</td></tr>
<tr><td>$u = 0\ m/s$</td><td>$v = 0\ m/s$</td><td>$w = 0\ m/s$</td></tr>
<tr><td rowspan="4">Grid</td><td rowspan="2">Desc.</td><td>2D</td><td colspan="2">Square geometry. Inviscid Walls and Symmetry</td></tr>
<tr><td>3D</td><td colspan="2">Cubic geometry. Inviscid Walls and Symmetry</td></tr>
<tr><td rowspan="2">Size</td><td>2D</td><td colspan="2">200x200 Cells</td></tr>
<tr><td>3D</td><td colspan="2">200x200x200 Cells</td></tr>
<tr><td rowspan="3">Sim. Config.</td><td rowspan="3">CFL</td><td>2^{nd} Order Minmod</td><td colspan="2">0.4</td></tr>
<tr><td>5^{th} Order WENO</td><td colspan="2">1.0</td></tr>
<tr><td>5^{th} Order TVD-MLP</td><td colspan="2">0.4</td></tr>
<tr><td>Output</td><td>Time</td><td>0.2 s</td><td colspan="2"></td></tr>
</table>

Table 4.7: 2D and 3D test cases set-up

employed here is done through comparison with experimental data at t = 0.2 s. As seen in Table 4.7, a fine resolution has been used here (200x200 cells), so results will also be useful to determine the stability of the approach when dealing with high-order high-resolution methods in small cells. In terms of the configuration for multispecies, it must be said that the experimental data considered was obtained for a single-species fluid in the 2D-Cylindrical Explosion problem, so no volume fraction information is available. In the present analysis, however, both 2D and 3D cases were run considering an inner species and an external one. Since the expected behaviour is well known (the interface moves with the contact discontinuity), one has the capacity to evaluate the goodness of the approach.

Figure 4.19 plots pressure and density one-dimensional profiles at t = 0.2 s for all cases (data are taken uniformly throughout the radial direction X) in the 2D-Explosion case. Again, results are pretty much as accurate as in the Shock Tube case, with the TVD-MLP again being slightly better than the WENO and sensitively superior to the Minmod. The WENO scheme, for its part, presents small long-wavelength oscillations in the surroundings of the contact wave. Such oscillations are damped over time, as occurred in the Shock Tube case. As for the shock wave, its end is very well captured in time, yielding a small error towards the unperturbed flow. This error is of course rapidly decreased with finer grids, and does not drive the leading error in more complex computations.

Regarding the evolution of the inner species, Figure 4.20 displays, in a qualitative fashion, two 3D views where the vertical axis measures density and pressure and the contours indicate volume fraction. As seen in Figure 4.20a, the mixture layer remains strictly restricted to the contact discontinuity, moving with it and therefore with the flow speed

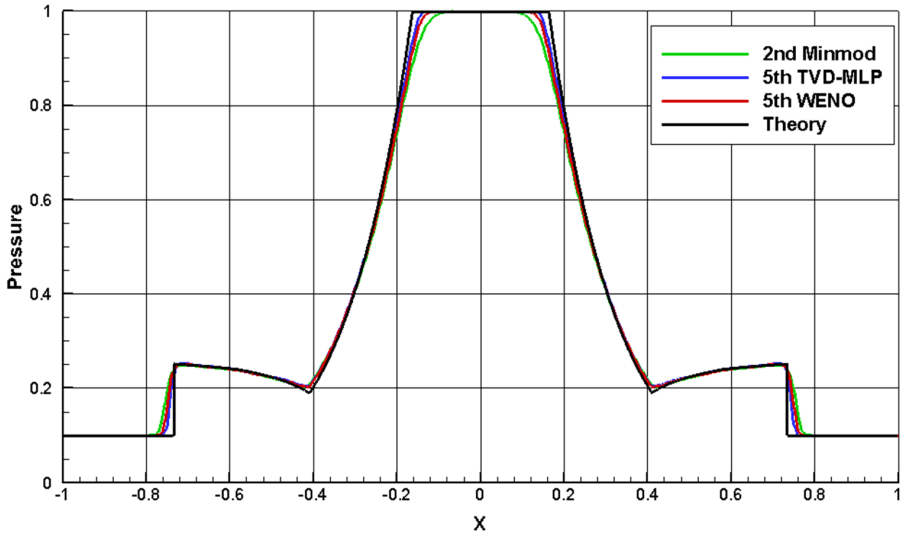

(a) Pressure

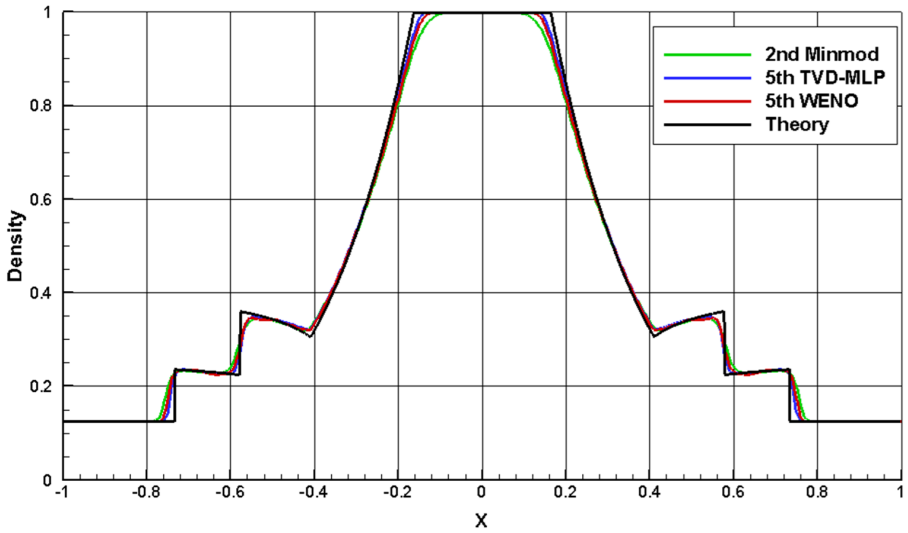

(b) Density

Figure 4.19: Pressure and density in the 2D Explosion problem at t = 0.2 s

after the shock wave. This fact is clearly visible in Figure 4.20b, where the smooth variation of volume fraction is depicted with different rainbow colours. This transition from inner pure fluid to outer pure fluid can be perfectly appreciate in this figure, noting the importance of the continuous mixture layer defined to deal with numerical diffusion.

Finally, the 3D Explosion problem was run in a much computationally expensive mesh (8 million cells) to evaluate the real performance of FLAMENCO in fully 3D problems with all characteristic waves taking place. Although experimental data are not available in this particular case, the expected solution is well known from a qualitatively point of view. Figure 4.21 compares again, for all reconstruction schemes, pressure and density at t = 0.2 s. The effect of high resolution grids is evidenced, since little difference exists between 2^{nd} and 5^{th} Order methods and no difference at all is appreciable between TVD-MLP and WENO (only close to the left end of the rarefaction wave small discrepancies arise). This

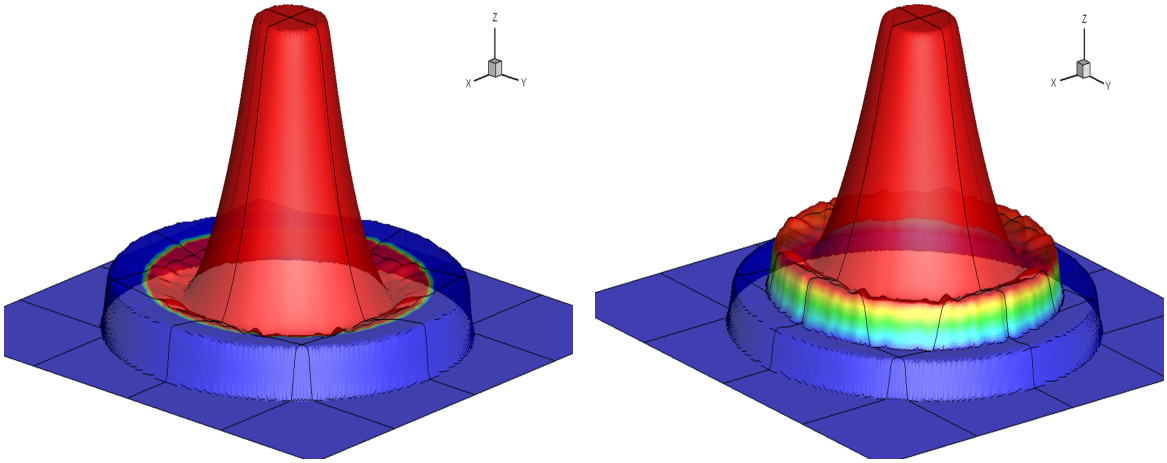

(a) Pressure and VF contours **(b)** Density and VF contours

Figure 4.20: 3D representations of pressure and density in the 2D Explosion problem at t = 0.2 s. Red contours indicate inner species volume fraction equal 1. Blue contours outer species volume fraction equal 1

result highlights the importance and advantages of high-resolution methods when used in coarse grids.

From a qualitatively point of view, the 3D-Explosion structure at t = 0.2 s can be observed by means of pressure and density iso-surfaces (Figure 4.22). In both images, the internal red core and external dark blue indicate unperturbed flow and the rainbow set of iso-surfaces represents the smooth transition in the rarefaction wave. As for the intermediate region in Figure 4.22b, it encompasses the contact wave and the near field. Finally, the shock wave lies between the last and second-to-last layers in both cases.

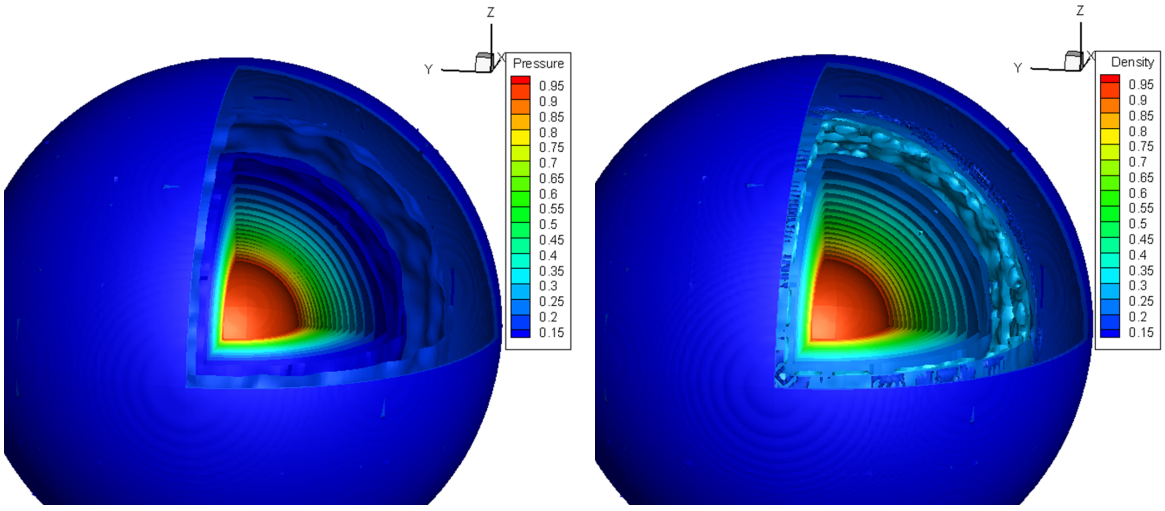

(a) Pressure **(b)** Density

Figure 4.22: Pressure and density iso-surfaces in the 3D Explosion problem at t = 0.2 s

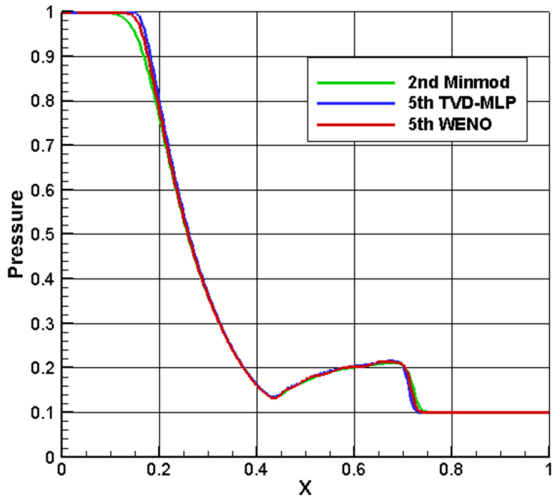

(a) Pressure

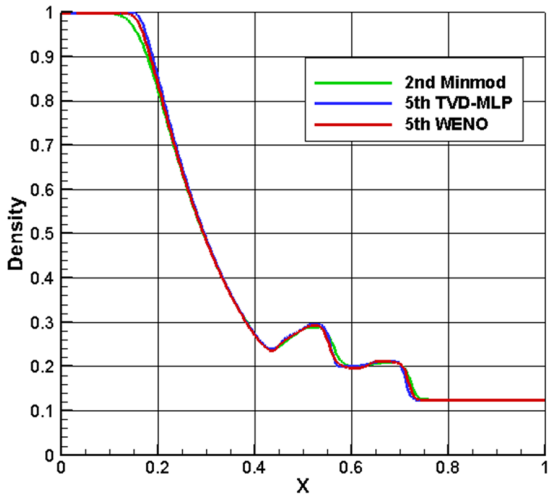

(b) Density

Figure 4.21: Pressure and density in the 3D Explosion problem at t = 0.2 s

4.3.3 Computational cost

A big effort was made in order to optimise FLAMENCO. A quick analysis revealed that more than 30% of the total computational time was spent in the reconstruction section of the code, pointing to this stage as the most restrictive one in the algorithm. As could not be otherwise, the 2^{nd} Order Minmod method performs the fastest, followed closely by the 5^{th} Order TVD-MLP and quite far from the 5^{th} Order WENO. This behaviour is obviously predicted from the mathematical definition itself, where each sub-time step requires four sub-iterations in the WENO case (and only one in the other schemes). As a consequence, special attention was paid to reconstruction boosting, keeping only strictly necessary calculations.

Figure 4.23 gives a good idea of the computational cost of test cases studied in Section 4.3.2. All simulations but the 2D and 3D Explosions were performed in single

processor with the 2^{nd} Order 4-Stages Runge-Kutta time integration scheme enabled in the Enhanced Explicit Runge-Kutta for Multispecies Flows framework. The 2D and 3D Explosions, while using the same time integration technique, were run with 4 processors in all cases but the WENO in the 3D Explosion, where 32 process were employed (and therefore this case is not comparable, indicated with ? in Figure 4.23). As expected, the 2^{nd} Order Minmod is the fastest, followed closely by the 5^{th} Order TVD-MLP and way from the 5^{th} Order WENO (note that computational time is expressed in logarithmic scale).

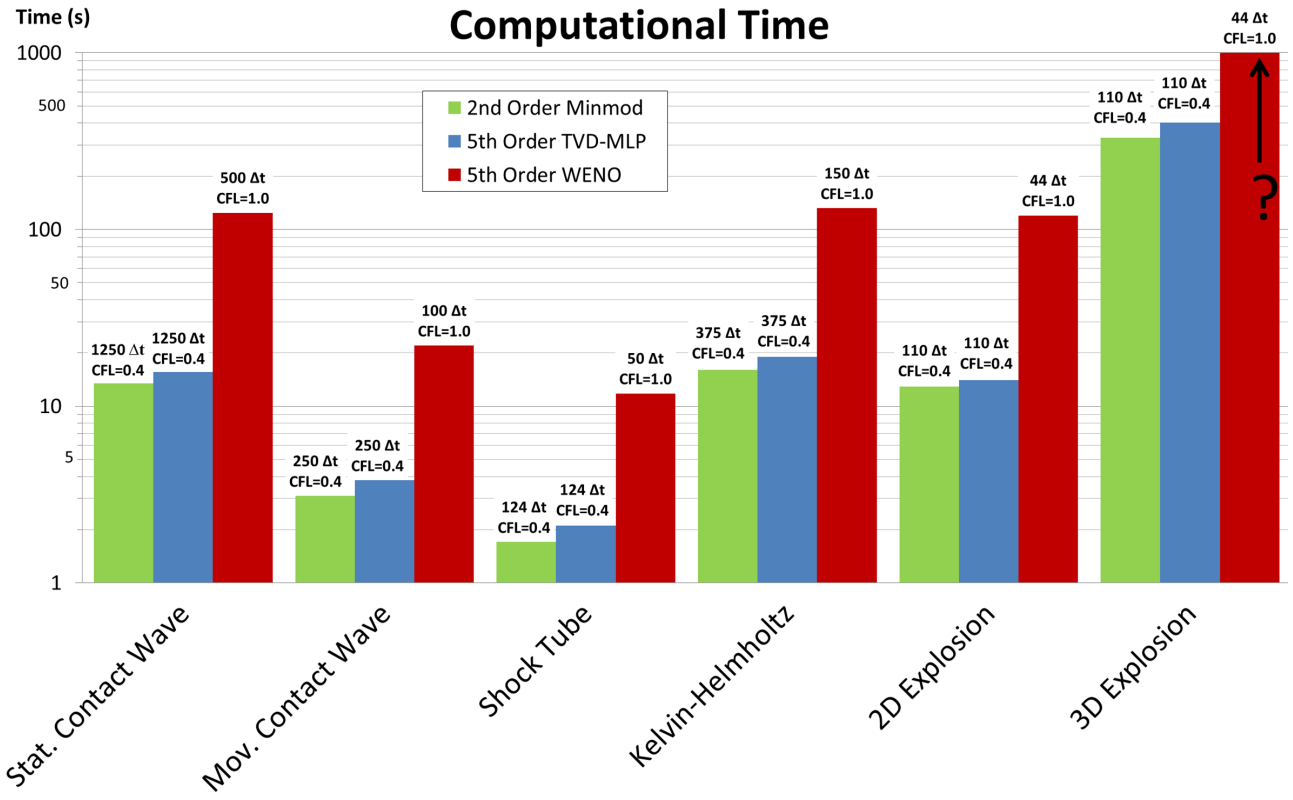

Figure 4.23: Computational times of each reconstruction scheme. Time is indicated in logarithmic scale. ? symbol stands for unknown time. Time steps and CFL numbers are indicated

In light of figure above, it can assertively be stated that the 5^{th} Order WENO scheme must be reviewed and reformulated if expensive simulations (more than 100000 cells and 10000 time steps) are aimed in FLAMENCO. Since the coarsest mesh considered in the modelisation of the Dry Low NOx GTU combustor has approximately 160000 cells and at least one million explicit time steps are needed, such modification becomes mandatory. The Simplified WENO for Efficient Computations scheme proposed in 3.2.1 emerges in response to that requirement, sacrificing accuracy for speed. As it will be shown later, the lost of accuracy is significant, but it still performs much better than the 2^{nd} Order Minmod reconstruction.

4.4 Validation of low dissipation strategies

Prior to any final simulation in the combustor geometry, it is essential to validate and assess Low Dissipation strategies implemented. For reliable results, and given that the problem and subsequent algorithm changes are restricted to the jet injector tube, the real inner tube geometry was employed. In particular, the validation grid consists of the actual jet injector with a reduced combustion chamber and without swirl duct. Based on it, two simulations were run up to 0.00223 s (approximately 10 characteristic times of 0.000215 s as corresponding to flow injected at 70 m/s in a channel 0.015 m long), which is more than enough to allow pressure divergence and wave bouncing. Both simulations were configured with the same general properties (i.e. viscous walls, 5^{th} Order TVD-MPL as general reconstruction scheme, nominal thermodynamic conditions, etc.) but with different inflow and outflow and treatment at the jet injector wall. Whereas the first computation was performed with typical subsonic inflow and outflow (i.e. extrapolation and specification of pressure respectively) and no modelling at the wall, as applied in previous versions of FLAMENCO, the second simulation was set up with Non-Reflecting Subsonic Inflow and Outflow and Adaptive Reconstruction Scheme at the jet injector wall.

Figure 4.24 shows pressure contours in a diametrical cut for both cases. As seen, important differences arise, not only within the jet injector duct, but also near the outflow. Looking at the inner tube, the first thing that draws attention is pressure inhomogeneity in Figure 4.24a compared to Figure 4.24b. Indeed, when Non-Reflecting Subsonic Inflow and Adaptive Reconstruction Scheme are not applied, numerical perturbations increase their magnitude due to continuous reflections and low dissipation. As a consequence, slightly non-axisymmetric features trigger the distribution shown in Figure 4.24a, which resembles the flow field within the jet injector depicted in the Introduction chapter (see Section 1.3). Obviously, the intensity of low and high pressure "bags" here is much lower than that generated when the whole problem is simulated (contour legend shows a range of 2000 Pa approx.), since additional actors such as the swirling flow, responsible for the creation of the the low pressure region at the injector's exit plane, are not present in this case. As for the outflow, reflected waves inside the domain induced by constant pressure at the boundary are clearly visible. This keeps pumping energy into the flow field, hampering global evacuation.

If Non-Reflecting Inflow and Outflow and Adaptive Reconstruction Scheme are used, the flow field becomes much more relaxed, as seen in Figure 4.24b. At this point, the expected smooth pressure distribution is achieved, yielding a maximum pressure range of 600 Pa. In the same way, development of transversal pressure waves is completely avoid, delivering one-dimensional distributions. Regarding the outflow, the fact that neither pressure nor density are fixed, but rather computed from incoming characteristic waves, leads to a homogeneous distribution within the chamber with no appreciable reflections. Hence, it remains demonstrated that the approach selected contributes to decreased the

level of stored energy.

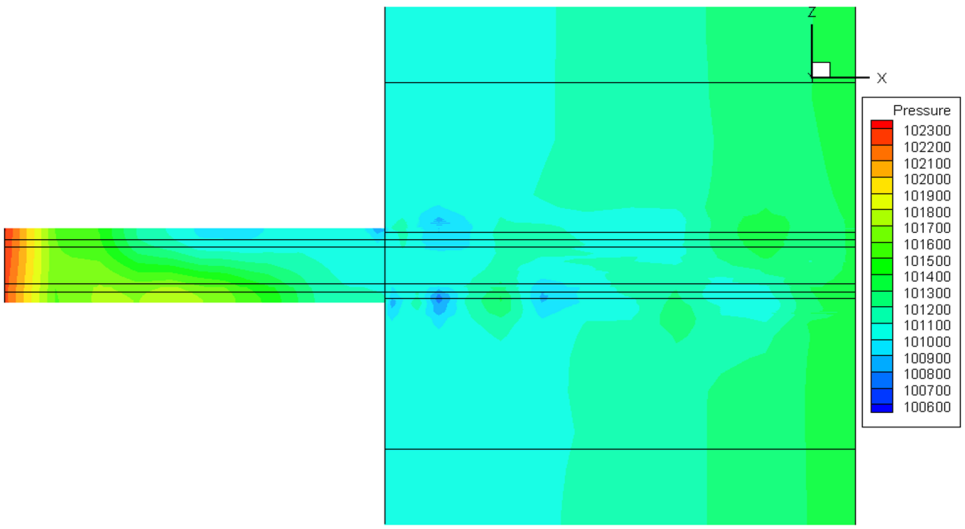

(a) Non-Reflecting BC and Adaptive Reconstruction NOT applied

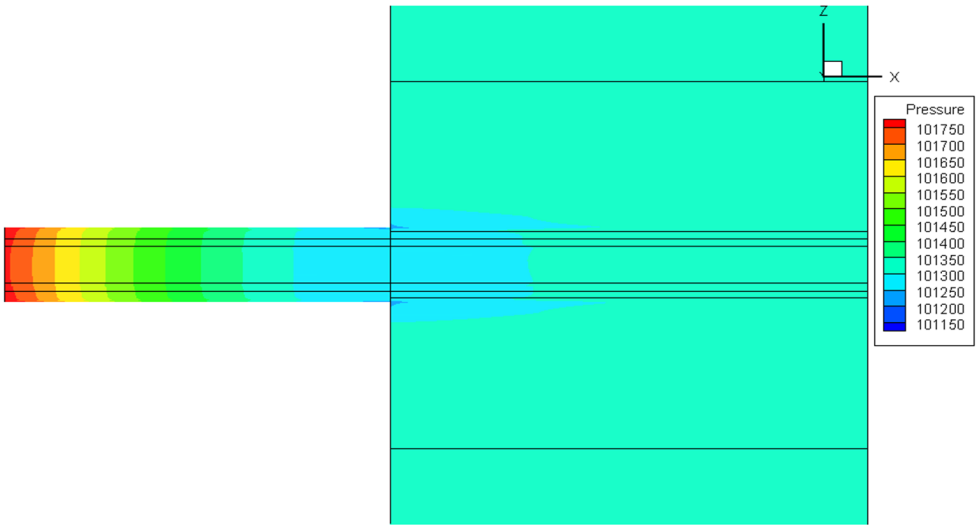

(b) Non-Reflecting BC and Adaptive Reconstruction applied

Figure 4.24: Pressure contours for simulations run with and without Non-Reflecting Boundary Conditions and Adaptive Reconstruction Scheme

Finally, for simplicity only results for Non-Reflecting Subsonic boundary conditions are shown here, since only this configuration will be used in the global combustor. However, it must be mentioned that all boundary conditions presented in Section 4.2.1 were tested, finding that whereas the Nozzle-type Inflow yields quite similar results (although in a much more computationally expensive process), the Partially Non-reflecting Subsonic Inflow is extremely problem-dependent and complex to calibrate.

Chapter 5

Results

5.1 Problem definition

The aim of this research project is to conduct an exhaustive analysis of the physics taking place within the Low Dry NOx GTU Combustor. To serve this purpose, FLAMENCO was configured so that the most accurate, reliable and stable potential results were acquired. After deep analisys. a combination of already mentioned Low Dissipation strategies was found to perform the best. In particular, the Non-Reflecting Subsonic Inflow and Outflow in conjunction with the Explicit 2^{nd} Order 4-Stages Runge-Kutta Enhanced for Multispecies Flows and Adaptive Reconstruction Scheme together with a slightly shorter jet duct yielded surprisingly good results even for extremely coarse grids.

Although there are many studies addressing Gas Turbine injection, mixing and combustion, the Low Dry NOx GTU Combustor case in particular has received less attention so far due to its newness as a cutting-edge method to meet increasingly restrictive pollutant emission regulations. Consequently, it was difficult to find reliable data obtained in realistic environments. There are, however, relevant experimental data produced using water instead of gas as working fluid, keeping all dimensionless parameters consistent with those defined in real operating conditions for self-similar results. Hence, the work carried out in Loughborough University by K. Midgley et al. [6] was chosen as the main source of information to compare with. Additionally, the numerical analysis performed by L. Cheng et al. [70] in the same conditions was used, whenever relevant, to assess the goodness of the approach proposed here. Last but not least, inaccurate results obtained with former versions of FLAMENCO in [8] were also incorporated to highlight the advantages of the new model proposed in the present study.

The conditions under which experimental data in [6] were obtained are somehow particular. Firstly, it has already been mentioned that instead of swirling air and axial methane flows, which are the working fluids in typical Dry Low NOx GTU combustors, they used water as both fuel and oxidant. This was achieved by splitting a previously pumped single water flow into two sub-flows, one for the inner jet injector duct and the other derived to the swirl duct. Then, whereas the inner flow was delivered with desired pressure and velocity conditions, the outer one fed a single radial swirler composed of

12 angled 30 degree slots (see Figure 1.5 in Section 1.3 for the experimental rig). The outcome of this configuration was nominal conditions shown in Table 5.1 at both the swirler and jet injector inlets, provided that all perturbations introduced by the swirl vanes were damped dowstream and way before the swirler inlet. In the same way, large heat-transfer characteristic times compared to the time of residence yielded a quasi iso-thermal problem.

	Property	Value	Additional Info.
Geometrical	D_J	5.40 mm	Jet Injector Diameter
	D_S	37.63 mm	Swirler Outer Diameter
	D_{S_0}	6.80 mm	Swirler Inner Diameter
	D_C	140 mm	Combustion chamber Diameter
	D_L	160 mm	Combustion chamber Length
Physical	Re_J	$2.63{\cdot}10^4$	Jet Injector Reynolds Number[1]
	Re_S	$8.0{\cdot}10^4$	Swirler Reynolds Number[2]
	S	0.74	Swirl Number[3]
	V_{x_J}	4.88 $\frac{m}{s}$	Axial Jet flow Velocity
	V_{x_S}	2.13 $\frac{m}{s}$	Axial Swirl flow Velocity
	V_{θ_S}	2.30 $\frac{m}{s}$	Tangential Swirl flow Velocity
	p	101325 Pa	Pressure
	ρ	1000 $\frac{kg}{m^3}$	Density
	μ	$1.003{\cdot}10^{-3}$ $\frac{kg}{m{\cdot}s}$	Viscosity

Table 5.1: Experimental set-up employed in K. Midgley et al. [6]

As said before, in addition to experimental results and numerical data from [70], the most accurate simulation run in [8] with the previous version of FLAMENCO is considered for comparison. Such simulation, referred in that text as "5thLID", corresponds to the 5^{th} Order TVD reconstruction case with Low Mach Correction enabled and jet injector with full length.

In terms of data availability, authors in [6] provide a full set of averaged and fluctuating magnitudes at several axial stations within the combustor. Furthermore, they give information about the flow inside the swirl injector and turbulent mixing profiles. As for the numerical study in [70], data are available only close to the swirler exit, where special attention is paid to turbulence and power spectra. Finally, output from [8] covers all results generated in [6], so enough information is accessible.

[1] Defined as $Re_J = \frac{\rho D_J V_{x_J}}{\mu}$ at injector's exit plane

[2] Defined as $Re_S = \frac{\rho D_S V_{x_S}}{\mu}$ at injector's exit plane

[3] Defined as $S = \frac{\int_{\frac{D_{S_0}}{2}}^{\frac{D_S}{2}} \rho V_{\theta,s} V_{x,s} r^2 dr}{\frac{D_S}{2} \int_{\frac{D_{S_0}}{2}}^{\frac{D_S}{2}} \rho V_{x,s}^2 r dr}$ at injector's exit plane

5.2 Grid generation and Boundary Conditions

After deep analysis, it was found that the low dissipation problem affecting FLAMENCO was better overcome if a suitable combination of Low Dissipation strategies was followed. In this way, it must be said that none of these methods alone produced satisfactory results, since energy evacuation did not balance energy production within the jet injector. Thus, the issue was tackled from several fronts, including geometry modifications, non-reflecting boundary conditions and dissipative schemes.

Regarding geometry modifications, the baseline geometry shown in Figure 5.1, used by researchers from Perm University in their simulations of the Dry Low NOx GTU combustor, was redefined by slightly reducing the jet injector duct. This small change was only made after checking flow independence downstream at the jet injector exit. In this way, several tests were conducted prior to any final simulation in order to ensure that flow dynamics were not significantly perturbed by this duct shortening. In fact, from the two actors potentially affected by the modification, namely turbulence and boundary layer, only turbulence may induce appreciable errors, since the actual tube length used was long enough to allow a quasi-developed boundary layer. This conclusion is only true for the coarse grid used, since the fine grid required a shorter tube in order to balance low numerical dissipation, leading to a partially-developed boundary layer at the jet injector exit.

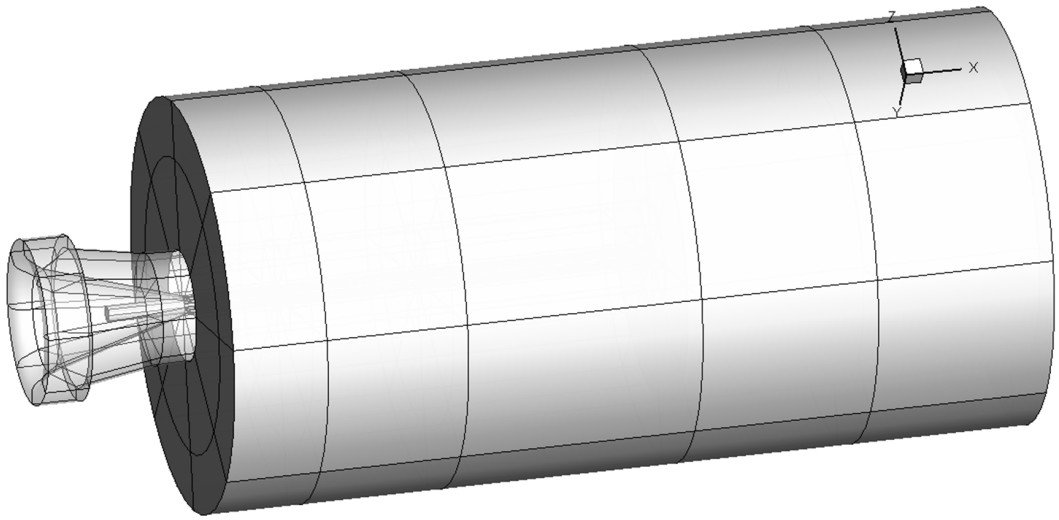

Figure 5.1: Baseline geometry of the Dry Low NOx GTU Combustor

Two grids based on the baseline geometry presented in Figure 5.1 were used to perform all simulations, one coarse and one fine. In fact, due to the huge computational cost of calculations in the fine grid, where the CFL number was sensitively decreased, and the limited computational resources available, just one case was run in this mesh (see Section 5.3 below). Figure 5.2 shows planar views of both grids, highlighting the jet injector tube

where different lengths were used. As seen, whereas approximately 75% of the baseline tube (L = 0.01253 m) was used in the coarse mesh, only a 25% was employed in the fine one. This modification was necessary to control energy generation and dissipation, ensuring balanced contributions. As could not be otherwise, smaller cells in the fine grid lead to lower numerical dissipation, which in turn forces a shorter tube length in order to prevent pressure divergence. Table 5.2 shows characteristic parameters of both meshes.

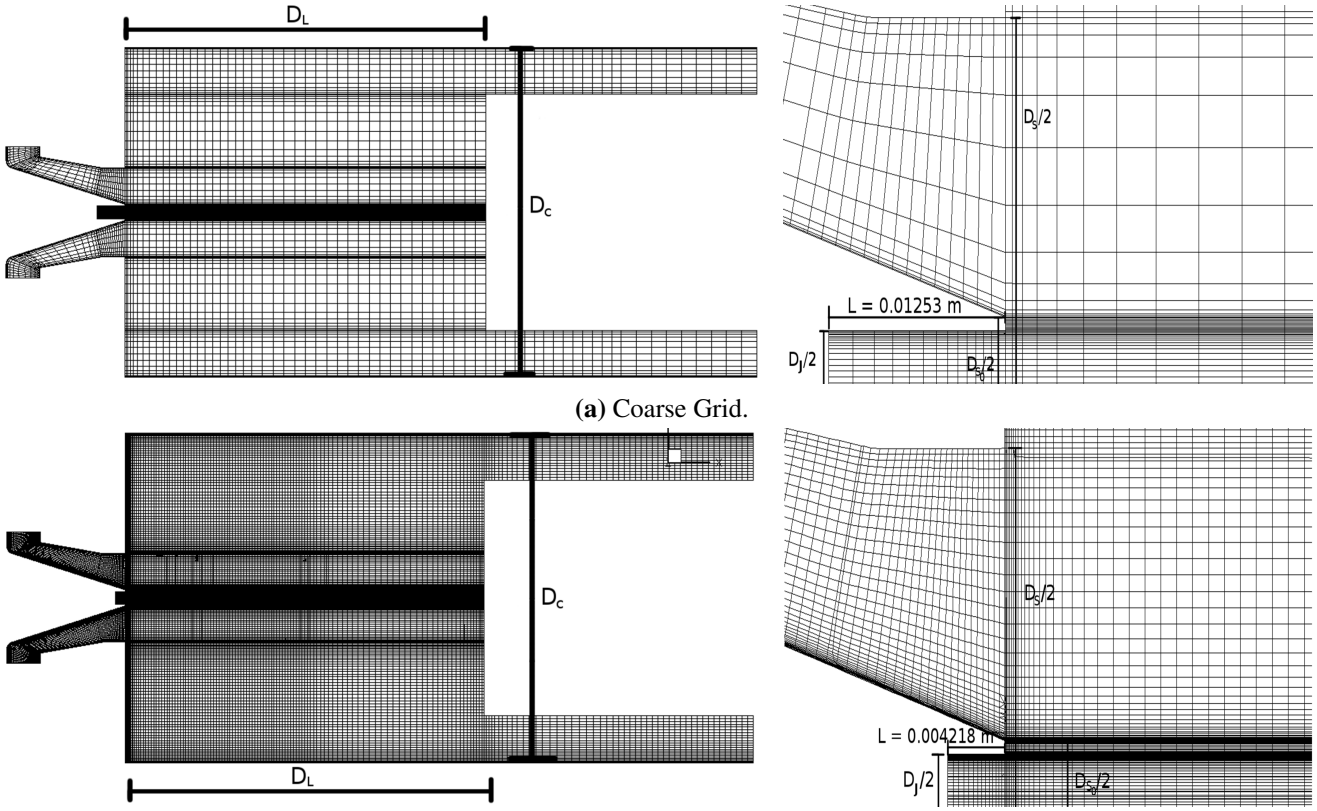

(a) Coarse Grid.

(b) Fine Grid

Figure 5.2: Coarse and fine grids. Jet Injector and Swirler are shown in detail. Geometric parameters are given in Table 5.1. The central zone in Figures a and b is filled with black due to high number of cells and low printing resolution

Two properties of above grids must be pointed out. First, it has been a priority to define higher resolution and smooth transitions at critical regions such as walls, shear layers, separation and recirculation zones, etc. Thus, mesh refinement at the jet tube upper wall, swirler lower wall, central region close to the rotation axis and surroundings of the injector exit has been intensified, ensuring coherent cell lengths at every single point of the domain. Second, according to LES criteria, boundary layers developed in both ducts are only resolved in the fine grid. Indeed, as seen in Table 5.2, while 20 cells are placed within the boundary layer in the fine grid, only 6 are used in the coarse one. This certainly implies that all phenomena associated with turbulence in boundary layers (and subsequent effects) are only taken into account in the fine mesh simulations.

	COARSE	FINE
Total Number of cells	147,700	1,594,476
y^+ Upper wall Swirler[1]	30.44	30.44
x^+ Upper wall Swirler[2]	83.10	41.55
y^+ Lower wall Swirler	4.96	1.02
x^+ Lower wall Swirler	83.10	38.90
Cells in boundary layer δ Lower Wall Swirler	5	20
y^+ Jet Injector wall	13.47	3.94
x^+ Jet Injector wall	355.77	81.40
Cells in boundary layer δ Jet Injector wall	5	20
Characteristic interior cell size x^+,[3]	204.04	73.15

Table 5.2: Characteristic parameters of both coarse and fine grids

From Table 5.2 above there are several features that must be kept in mind. First of all, it should be noted that dimensionless wall distances are based on the characteristic Reynolds number at each region. In this way, at the swirler walls Re_S is taken and at the jet injector walls Re_J is used instead (see Table 5.1 for definition of these variables). Within the combustion chamber, however, a dimensionless length is provided based on Re_J, giving a rough idea of the mean cell size used in the mixing and recirculation zones. As seen, the fine grid presents three times more resolution here than the coarse one (x^+=73.15 vs x^+=204.04). The second important aspect is the y^+ distance defined at both jet and swirler, which must be approximately 1 for accurate resolution. Although it is the fine mesh the one that provides values closer to unity, this is not a potential source of significant errors in the coarse definition, since y^+ was taken small enough to capture mean turbulent scales (y^+=4.96 at the lower swirler wall and y^+=13.47 at the jet injector wall). Finally, it should be pointed out that large y^+ values at the upper swirler wall were chosen for reasons of computational efficiency, provided that high-shear regions, separation and sharp gradients are likely to occur close to the lower swirler wall.

Regarding the boundary conditions specified, if was found after several tests that the best performance in terms of acoustic reflections, computational efficiency and numerical stability was delivered by the Non-Reflecting Subsonic Inflow at both jet injector and swirler inlets and Non-Reflecting Subsonic Outflow at the combustor outlet. Figure 5.3 illustrates, in a 2D-cut containing the rotational axis, all boundaries and physical magnitudes specified. It must be borne in mind that all variables at both inlets were chosen in such a way that nominal conditions were achieved at the injector's exit plane indicated in Figure 5.3, which is the exact location where inflow conditions are indicated

[1] Defined as $y^+ = \frac{y \cdot U_\tau}{\nu}$; $U_\tau = 0.19748 \frac{\nu}{\rho} Re^{\frac{7}{8}}$; $y \equiv$ First cell height normal to wall

[2] Defined as $x^+ = \frac{x \cdot U_\tau}{\nu}$; $U_\tau = 0.19748 \frac{\nu}{\rho} Re^{\frac{7}{8}}$; $x \equiv$ First cell length parallel to wall

[3] Based on the Jet Injector Reynolds Number

in the experimental analysis (see Table 5.1). The calibration procedure followed to obtain these magnitudes was tedious, computationally expensive and somehow inaccurate, since several "ad-hoc" simulations were undertaken in order to produce acceptable data. As a consequence, the actual characteristic parameters employed were slightly deviated from the nominal ones, introducing a source of errors that cannot be neglected in any case. Finally, all walls were set as "Viscous walls", reversing velocity components and mirroring scalars.

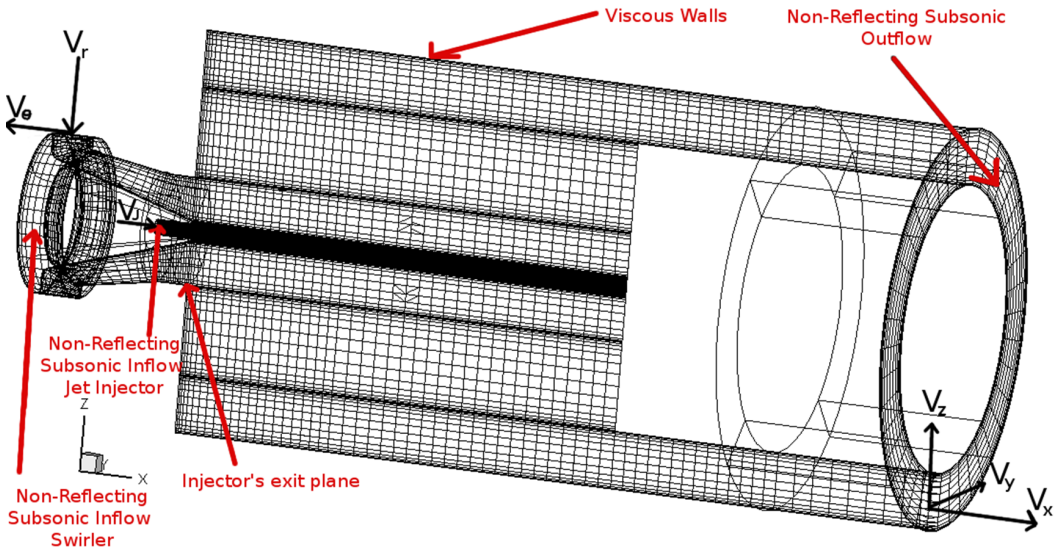

Figure 5.3: Boundary Conditions

5.3 Problem set-up

In order to compare with data from [6], where experiments were conducted using only water as working fluid, magnitudes must be specified consistently in the present problem, knowing that FLAMENCO deals with compressible flows and only air is considered as both swirling and jet flows. A dimensional analysis shows that, as long as all characteristic dimensionless parameters are equal, comparable flow phenomena may occur. Hence, variables here were set to yield same Reynolds numbers and Swirl number, which were computed using bulk magnitudes at the injector's exit plane. It must be said that although consistent, there are important acoustic-related issues that induce significant perturbations at this plane, making an accurate set up more difficult. Table 5.3 shows values at all boundaries (illustrated in Figure 5.3) compared to the experimental ones used using water. As for the initial conditions, the flow field within the whole geometry was filled with stagnated air, z_{air}=1, z_{fuel}=0, at constant pressure 101325 Pa.

Several simulations were run, aiming to cover a broad range of numerical methods. In particular, 2^{nd} Order Minmod, 5^{th} Order TVD-MLP and 5^{th} Order WENO reconstructions were applied separately in the coarse grid. As for the fine mesh, due to huge computational

cost and limited resources only the 5^{th} Order TVD-MLP algorithm was tested. Such scheme was selected after noting that it performed the best in the coarse grid, expecting to get the potentially most accurate results achievable with FLAMENCO.

		Non-Reflecting Subsonic Inflow				Non-Reflecting Subsonic Outflow
		Jet Injector		Swirler		
$V_x\left(\frac{m}{s}\right)$		V_J	u_a=70.7673 in Eq. (4.4)	0		Extrapolated
$V_y\left(\frac{m}{s}\right)$		0		V_r	12.150[1]	Extrapolated
$V_z\left(\frac{m}{s}\right)$		0		V_θ	17.325[2]	Extrapolated
P (Pa)		p_a=101325 in Eq. (4.4)		p_a=101325 in Eq. (4.4)		p_a=101325 in Eq. (4.4)
$\rho\left(\frac{kg}{m^3}\right)$		ρ_a=1.225 in Eq. (4.4)		ρ_a=1.225 in Eq. (4.4)		ρ_a=1.225 in Eq. (4.4)
z_{fuel}		1		0		Extrapolated
z_{air}		0		1		Extrapolated
Injector's exit plane		**Num.**	**Exp.**	**Num.**	**Exp.**	
	$V_x\left(\frac{m}{s}\right)$	70.7673	4.88	30.8915	2.13	
	$V_y\left(\frac{m}{s}\right)$	0	0	V_θ=33.86	V_θ=2.30	
	$V_z\left(\frac{m}{s}\right)$	0	0			
	S	-	-	0.74	0.74	
	Re	$2.63{\cdot}10^4$	$2.63{\cdot}10^4$	$8.0{\cdot}10^4$	$8.0{\cdot}10^4$	

Table 5.3: Boundary Conditions

In terms of general configuration, all simulations were run with the Adaptive Reconstruction Scheme enabled only in the jet injector walls. This choice was made to enhance transversal wave dumping just in the region where pressure divergence is expected. Additionally, the 2^{nd} Order 4-Stages Enhanced Explicit Runge-Kutta was always used to ensure stable numerics, allowing larger time step sizes and thus bringing the computational time to affordable values. Finally, molecular viscosity for the air was computed using Sutherland's law.

Table 5.4 displays all information commented before as well as computational times for each simulation. As seen, two physical times are given, one associated with the initialisation stage (period where the flow is taken to a "statistically steady state") and another related to the elapsed time between samples. The initialisation stage was assumed to last approximately 10 characteristic times, understanding "characteristic time" as the period during which an average fluid particle is travelling from any inflow to the outflow of the chamber. Whereas in the coarse grid this requirement was almost satisfied (note that, for characteristic length and velocity of 0.25 m and 50 m/s, the time of residence is approximately 0.005 s which is roughly 1/9 of the initialisation time 0.043 s), only 6.5

[1] v_a in Eq. (4.4) is computed as $v_a = -12.15 \cdot \frac{y}{\sqrt{y^2+z^2}} - 17.325 \cdot \frac{z}{\sqrt{y^2+z^2}}$; y,z coordinates

[2] w_a in Eq. (4.4) is computed as $w_a = -12.15 \cdot \frac{z}{\sqrt{y^2+z^2}} + 17.325 \cdot \frac{y}{\sqrt{y^2+z^2}}$; y,z coordinates

characteristic times were run in the fine grid, again due to computational cost. This fact must be borne in mind when assessing the accuracy of both approaches.

Regarding the sampling stage, 100 samples every $8.86{\cdot}10^{-4}$ s (20000 time steps) and 40 samples every $8.25{\cdot}10^{-4}$ s (100000 time steps) were collected from simulations run in the coarse and fine grids respectively. In this way, providing a homogeneous sampling interval for all cases was prioritised over the number of samples. This of course will have some repercussions on the accuracy of statistically steady and intrinsically unsteady phenomena estimated in the fine mesh. Finally, looking at the computational cost of each simulation, it seems clear that while running 100-150 hours in 32 CPU is affordable in a small, shared HPC machine ($\sim$1280 CPU), 600 hours in 128 CPU becomes much more difficult. This is the main reasons why simulations had to be carefully chosen before being launched.

Simulation		2ndCoarse	5thMLP_Coarse	5thWENO_Coarse	5thMLP_Fine
Grid		Coarse	Coarse	Coarse	Fine
Reconstruction		2^{nd} Order Minmod	5^{th} Order TVD-MLP	5^{th} Order WENO Enhanced Comp.	5^{th} Order TVD-MLP
CFL		0.4	0.4	0.4	0.4
Time Step		$\sim 4.43 \cdot 10^{-8}$ s	$\sim 4.43 \cdot 10^{-8}$ s	$\sim 4.43 \cdot 10^{-8}$ s	$\sim 8.25 \cdot 10^{-9}$ s
Phyisical Time	**Initialisation**	0.043 s	0.043 s	0.043 s	0.033 s
	Sampling	0.086 s	0.086 s	0.086 s	0.033 s
Sampling Frequency (time between samples)		$8.86 \cdot 10^{-4}$ s	$8.86 \cdot 10^{-4}$ s	$8.86 \cdot 10^{-4}$ s	$8.25 \cdot 10^{-4}$ s
Computational Cost		108 h/32 CPU	120 h/32 CPU	144 h/32 CPU	600 h/128 CPU

Table 5.4: Simulation set-ups

5.4 Statistically steady phenomena: CRZ and Vortex Breakdown

When addressing such a complex problem as the mixing process in the Dry Low NOx GTU Combustor, it is convenient to separate the analysis of phenomena different in nature. For this purpose, whereas statistically steady features, namely the CRZ and Vortex

Breakdown, are studied through averaged profiles, intrinsically unsteady structures are characterised using root mean square profiles.

Regarding statistically steady phenomena, all samples collected were averaged to create mean axial and volume fraction profiles. This way of proceeding was chosen because only these two magnitudes are enough to characterise both qualitatively and quantitatively internal structures that maintain a repetitive behaviour over time. Firstly, the CRZ is completely defined by axial mean velocity profiles along the combustion chamber, which must shown the toroidal shape by means of negative axial velocity close to the axis of rotation and high positive velocities neat the walls. This distribution must be relaxed towards the rear wall of the chamber where axial velocity profiles are much flatter, and must shift to positive values with little recirculation close to the injector's exit plane. As for the Vortex Breakdown, since this process takes place near the end of the swirler (close to the lower wall), axial velocity profiles are extracted there in order to observe separation and recirculation. Finally, it must be said that the axi-symmetrical behaviour of all structures allows 1-D representation of profiles along the radial direction.

For a general overview of the statistically steady flow distribution, Figure 5.4 depicts velocity vectors in a 2-D cut along the combustion chamber for all cases considered. It can be seen that all approaches identify the main statistically steady structures to a greater or lesser extent. As expected, the CRZ is always captured in the middle of the combustor, extending approximately from X/Ds = 1.5 to X/Ds = 3 and from r/Ds = 0.2 to r/Ds = 1.5. This central eddy is obviously the two-dimensional cut of the main toroidal vortex responsible for flow recirculation from the rear wall to the injection region. Comparing to Figure 5.4a, where experimental velocity vectors are represented, it can be observed that 5thMLP_Fine, 5thMLP_Coarse and 5thMLP_WENO yield a similar layout. As for the 2ndCoarse, the field predicted is quite chaotic and imprecise, showing small unphysical eddies within the CRZ.

Regarding separation near the lower wall of the swirler, it was reported in [6] that an angle of approximately 60 deg. is described by the detached flow. From vector plots in Figure 5.4, it is appreciable that only 5^{th} Order reconstruction is able to capture this feature properly. Although both 5thLID and 2ndCoarse cases predict separation reasonably well from a qualitative point of view, they fail to give an accurate opening angle (note that 2ndCoarse separation is only partially defined due to unphysical eddies scattered near the lower wall).

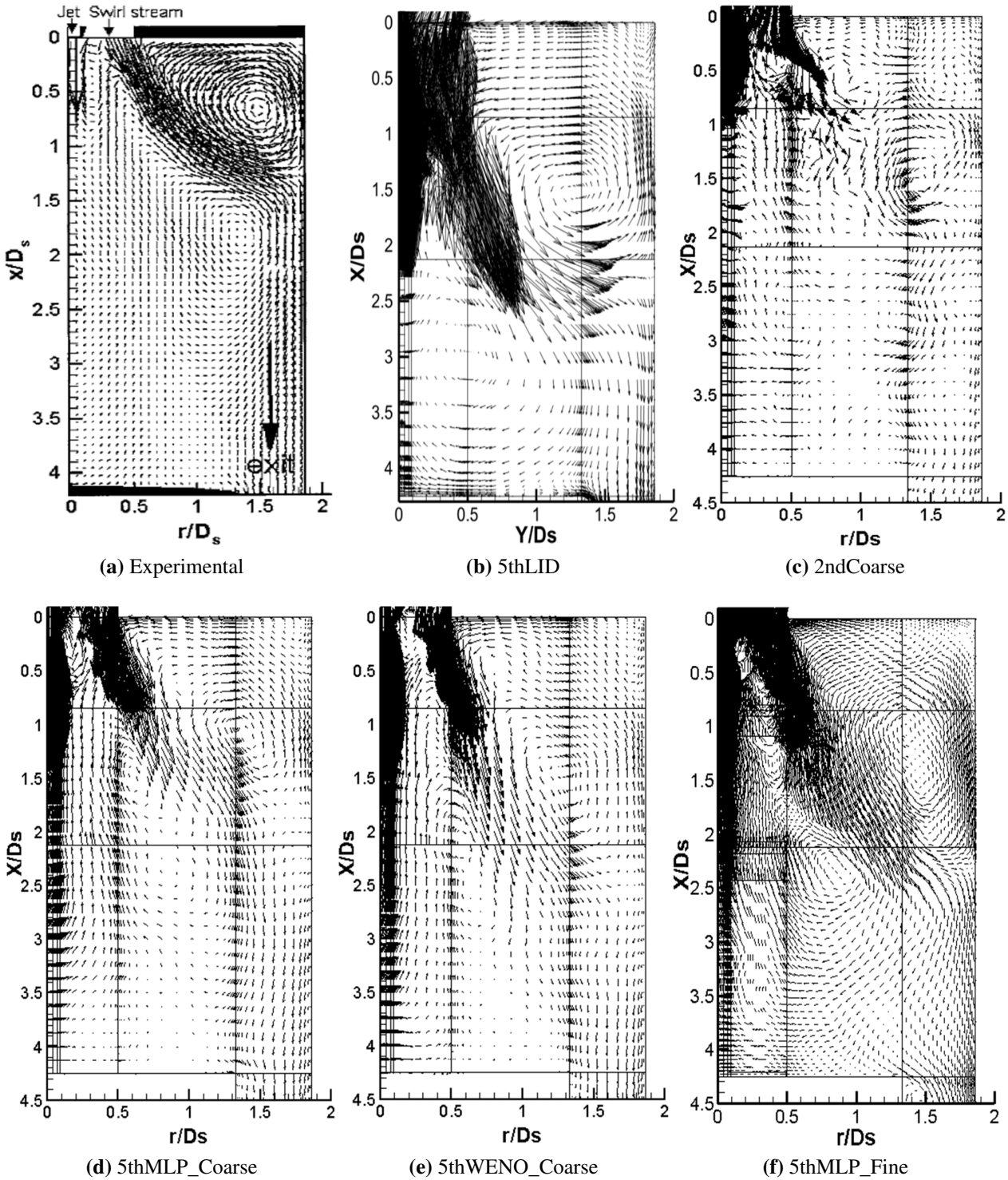

(a) Experimental **(b)** 5thLID **(c)** 2ndCoarse

(d) 5thMLP_Coarse **(e)** 5thWENO_Coarse **(f)** 5thMLP_Fine

Figure 5.4: Overall flow structure. All cases under study are represented.

The final important structure to be mentioned is the recirculation zone developed in the upper-corner. This is also a toroidal structure, whose influence in the recirculation process is residual (note that only gases from the outer edge of the CRZ are transported towards the outer wall, brought to the upper corner and introduced again at the beginning of the

CRZ at very low velocity). All models capture this vortex, although in the 2ndCoarse one is not well defined, in the 5thLID case is estimated too far from the upper corner and in the 5thWENO_Coarse is excessively large.

Above observations are supported by streamtraces in the same 2D plane. For simplicity, Figure 5.5 only compares experimental data to 5thMLP_Coarse and 5thMLP_Fine cases, arguably the most accurate models in Figure 5.4. Here, the CRZ, recirculation vortex in the upper corner and separation in the swirler are well appreciated. Although quite accurate, the opening angle at the injector exit is still a little bit smaller than expected in both numerical models. This is additionally supported by axial velocity contours non-dimensionalised with Vs (actually V_x at the injector's exit plane of the Swirler in Table 5.3), also represented in Figure 5.5.

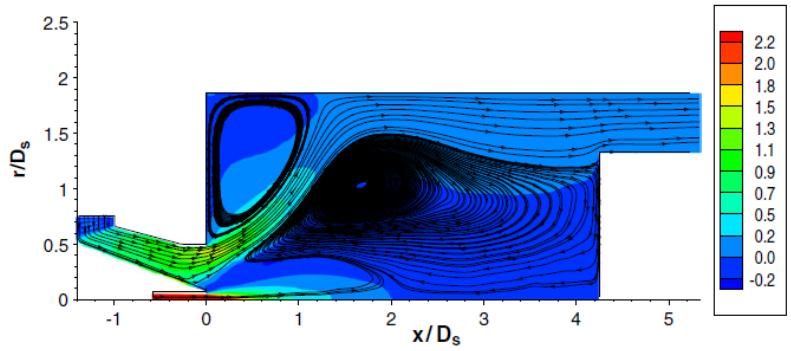

(a) Experimental from [70].

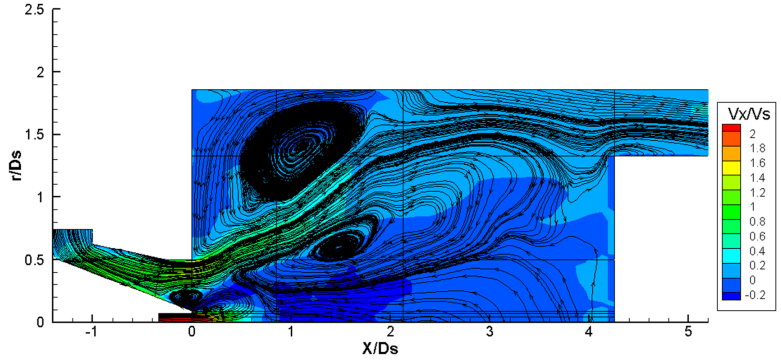

(b) 5thMLP_Coarse

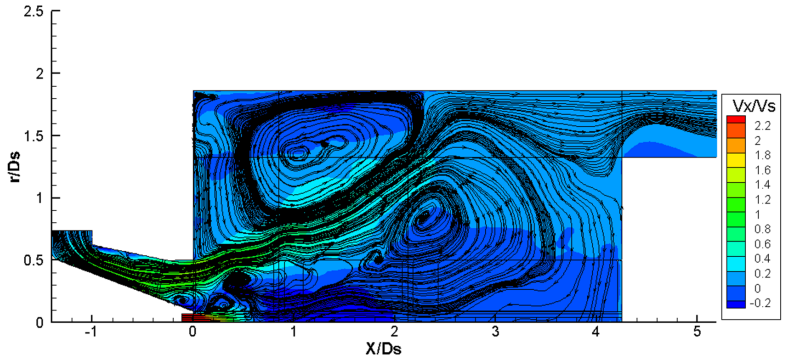

(c) 5thMLP_Fine

Figure 5.5: Streamtraces and dimensionless axial velocity contours.

Moving towards a quantitative analysis, axial mean velocity and mean volume fraction profiles are shown in Figure 5.7 and Figure 5.8 at six representative positions along the combustion chamber. Focusing on Figure 5.7, data from all simulations run are added to 5thLID results in order to be compared with experimental profiles at the injector's exit plane (X/Ds = 0), immediately after the injector exit (X/Ds = 0.02), at the front end (X/Ds =0.27), middle (X/Ds = 0.53) and rear end (X/Ds = 1.06) of the CRZ, and at 2/3 of the combustion chamber length (X/Ds = 2.65) where CRZ effects are small and the flow field becomes more relaxed. Figure 5.6 clarifies the exact location where data extraction was performed.

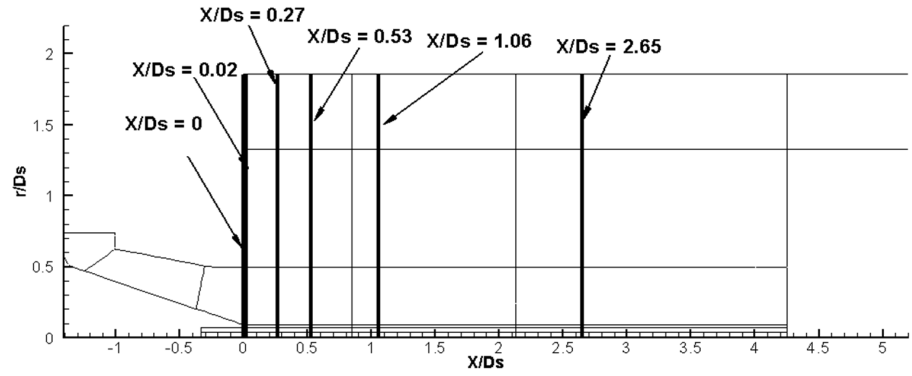

Figure 5.6: Data extraction lines along the combustion chamber.

Initial axial mean velocity distribution at both jet injector and swirler can be observed in Figure 5.7a (note that plots are only relevant up to r/Ds = 0.5, since further away the extraction line overlaps with the front wall of the combustor). A couple of points must be discussed regarding fuel and air injection. First of all, although Reynolds numbers are the same, viscous effects in water and a fully-developed boundary layer at the jet injector wall induce different experimental velocity distributions along the jet injector exit from those computed with the numerical models. Indeed, whereas experimental data in Figure 5.7a define a blunt velocity profile with the boundary layer extending almost to the very centre of the jet, all numerical approaches identify a sharp distribution with a thin boundary layer restricted to the near-wall region. This inaccuracy indicates that the fuel jet is not fully developed, and may be a potential source of errors to be discussed later. Regarding the swirler, the accuracy of 5thMLP_Coarse and 5thWENO_Coarse when capturing flow separation and recirculation due to Vortex Breakdown at the lower swirler wall is remarkable, even better than the one delivered by 5thMLP_Fine. This is explained by the fact that calibration of boundary conditions was done in the coarse grid, extrapolating the values to the fine mesh. As a consequence, small grid-dependencies lead to slightly inaccurate profiles in the fine grid, as seen in Figure 5.7a. Finally, although 2ndCoarse results improves the 5thLID solution obtained with a previous version of FLAMENCO, it fails notably in capturing axial velocity through the swirler.

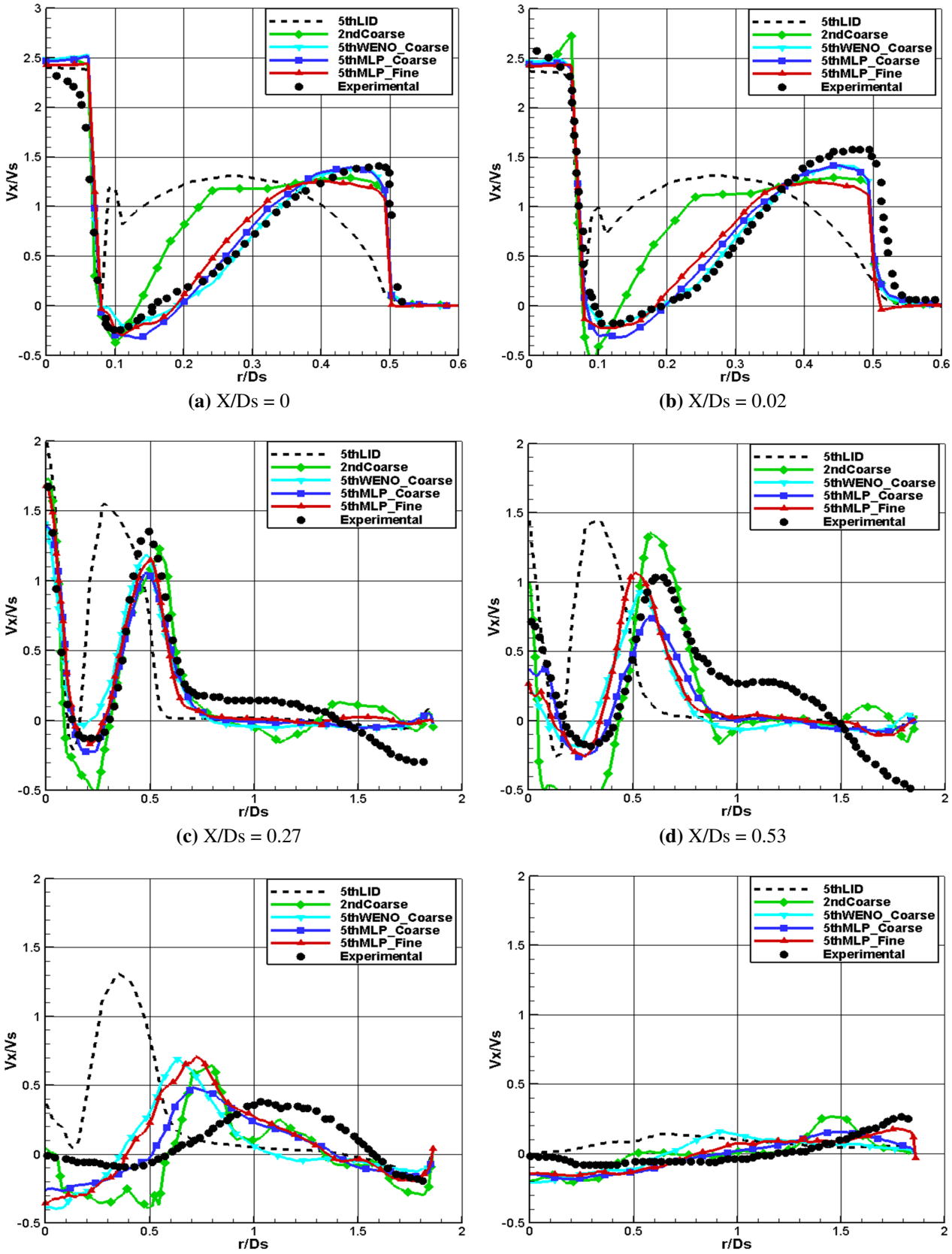

(a) X/Ds = 0

(b) X/Ds = 0.02

(c) X/Ds = 0.27

(d) X/Ds = 0.53

(e) X/Ds = 1.06

(f) X/Ds = 2.65

Figure 5.7: Axial mean velocity profiles in the x-r plane at five representative positions

Paying attention to the CRZ Figures 5.7c-5.7d-5.7e plot the reverse-flow region near the rotation axis, the "eye" of the structure characterised by stagnated conditions and the fast flow in the outer edge of the CRZ where high shear layers develop. In term of accuracy achieved, here 5thMLP_Fine stands as the best approach, followed closely by 5thMLP_Coarse and 5thWENO_Coarse. As for 2ndCoarse, it fails specially in the middle of the CRZ and again, all new computations perform much better than 5thLID. From Figure 5.7e the lack of accuracy obtained regarding the end of the CRZ must be pointed out, provided that all models predict a forward, smaller CRZ than the actual one. This is directly related to jet injector flow velocity, which is higher in numerical computations, leading to flatter but more intense CRZ.

Fuel Volume Fraction in profiles wrapping the CRZ are depicted in Figure 5.8 (referred as Volume Fraction 2). As seen, all methods mimic fairly well the experimental curve, denoting suitable volume fraction advection (and thus its numerical discretisation strategy). Again, and totally linked to what happened in the axial mean velocity profiles, at the end of the CRZ there is less fuel than expected, suggesting fast mixing near the injector and fuel transport towards the combustor wall.

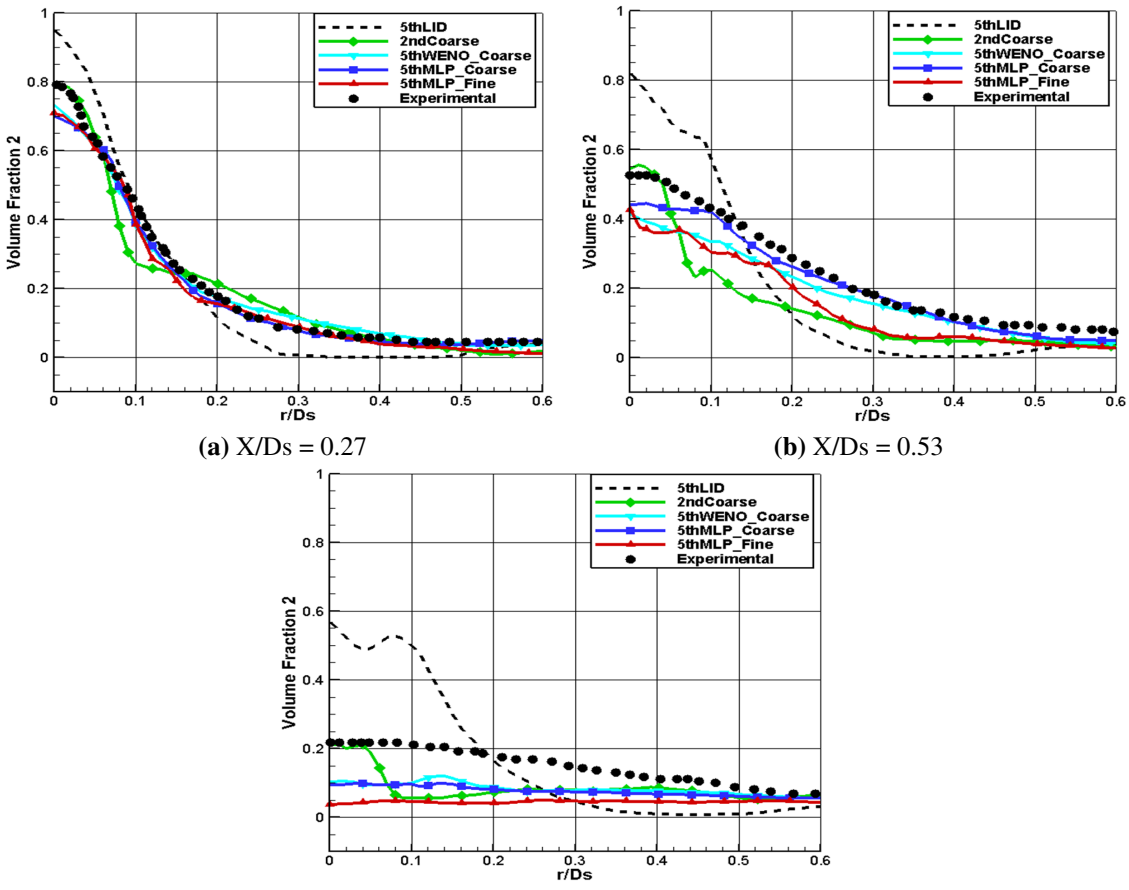

(a) X/Ds = 0.27

(b) X/Ds = 0.53

(c) X/Ds = 1.06

Figure 5.8: Mean Volume Fraction profiles in the x-r plane at three representative positions

5.5 Intrinsically unsteady structures: PVC and Secondary Vortices

PVC and Secondary Vortices are intrinsically unsteady structures tightly linked to turbulence and vortical perturbations derived from the chaotic flow developing in the combustion chamber. Hence, in order to study these complex 3D structures further analysis of turbulent kinetic energy is required. Bearing in mind that the inception of both PVC and Secondary Vortices occurs near the swirler exit, mainly affecting the flow in the first half of the chamber, the same procedure as the one employed in the previous section was followed. In this way, turbulent-related profiles were extracted along the same radial directions. Aiming to identify different features, turbulent kinetic energy and turbulent scalar diffusion are decomposed in axial, radial and tangential rms velocity fluctuations on one side and fuel volume fraction rms profiles on the other. In addition, turbulent axial fluxes were computed as they were found to be extremely useful to analyse the ability of each model to account for high-mixing in regions where turbulence plays a major role.

First of all, axial and radial rms velocity fluctuations are depicted in Figure 5.9 and Figure 5.10. Generally speaking, the good agreement evidenced indicates, on the one hand that secondary vortices responsible for the fluctuations generated near the separation region are well identified, and on the other hand that the mixing layer is well described both in size and position. These facts are extremely important when considering the suitability of the code for this type of problems where turbulence plays a vital role, supporting the idea that LES performs very well in this case.

Axial and radial profiles are particularly relevant to characterise PVC and Secondary Vortices developing near the injector exit (X/Ds = 0, X/Ds = 0.02, X/Ds = 0.27) and outer edge of the CRZ approximately at X/Ds = 0.53. Additionally, they are also very useful to identify the shear regions where high-mixing takes place. Focusing on turbulent profiles near the injector's exit plane, Figures 5.9a,b and Figures 5.10a,b show very good performance of 5^{th} Order methods, specially in the fine grid. This results are coherent with the treatment of turbulence made by FLAMENCO, where low dissipation is needed to model turbulence effects (5^{th} Order WENO is more dissipative that 5^{th} Order TVD-MLP, and obviously the finer the mesh, the less dissipative the numerical approach will be). Agreeing with this is the output of 2ndCoarse case, where 2^{nd} Order reconstruction kills all perturbations to a greater extent. It must be said, however, that turbulent velocities and fuel volume fraction in the 2ndCoarse case are not exactly 0, but their low value (ranging from 10^{-3} to 10^{-8} depending on the property) makes them indistinguishable from 0 in all figures presented.

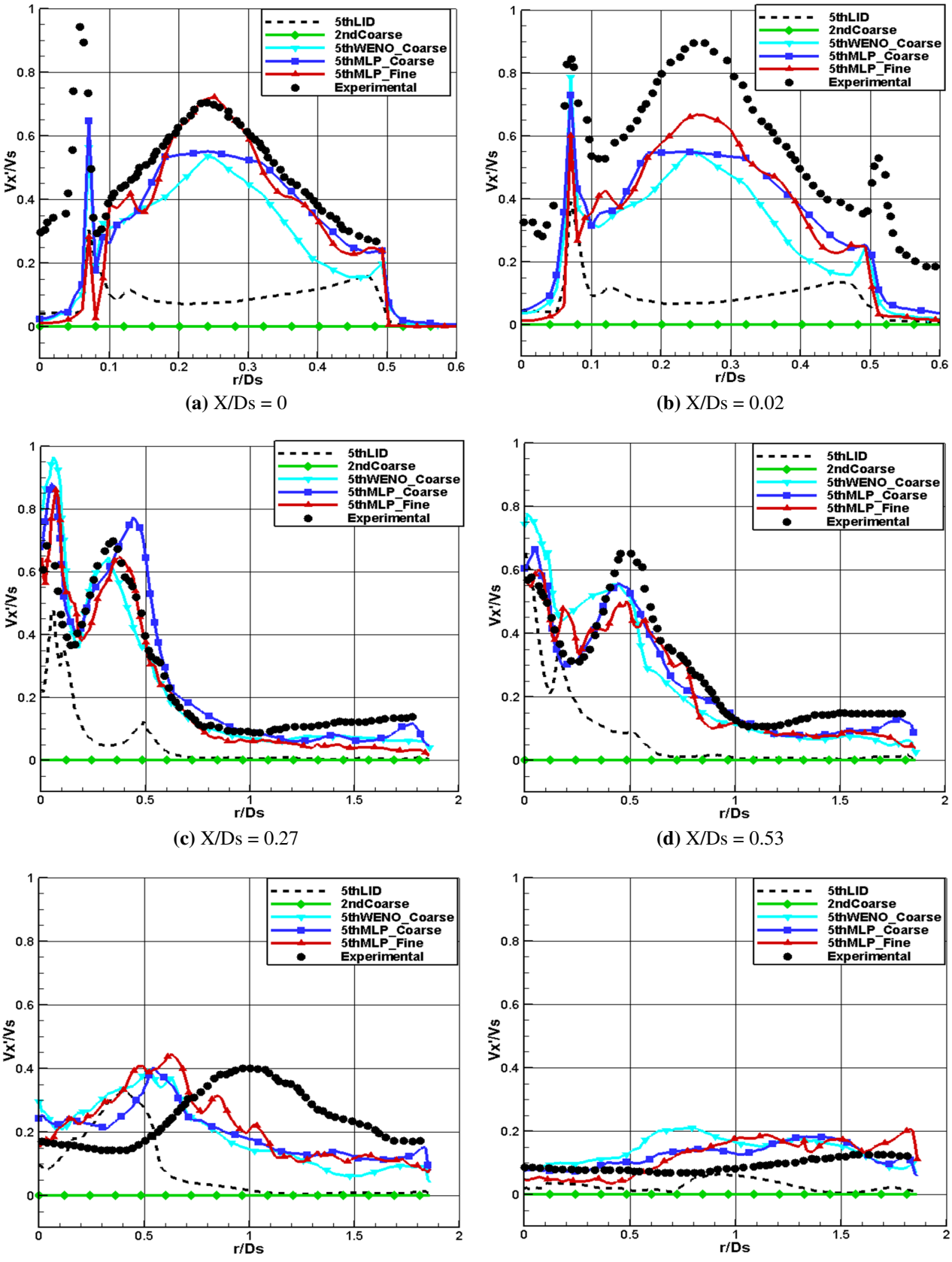

(a) X/Ds = 0

(b) X/Ds = 0.02

(c) X/Ds = 0.27

(d) X/Ds = 0.53

(e) X/Ds = 1.06

(f) X/Ds = 2.65

Figure 5.9: Axial rms velocity profiles in the x-r plane at five representative positions

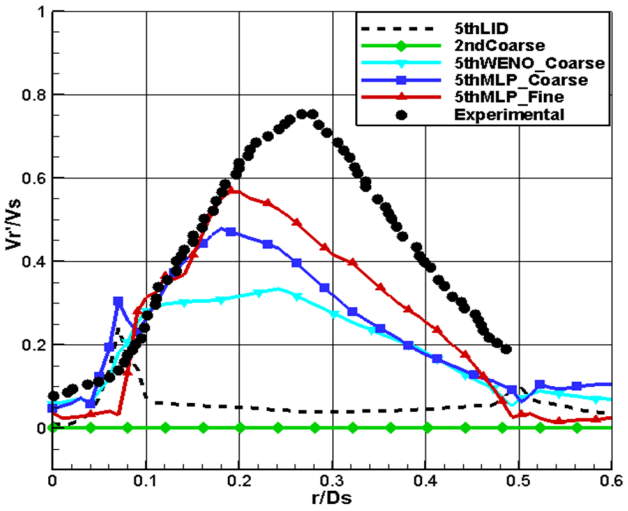

(a) X/Ds = 0

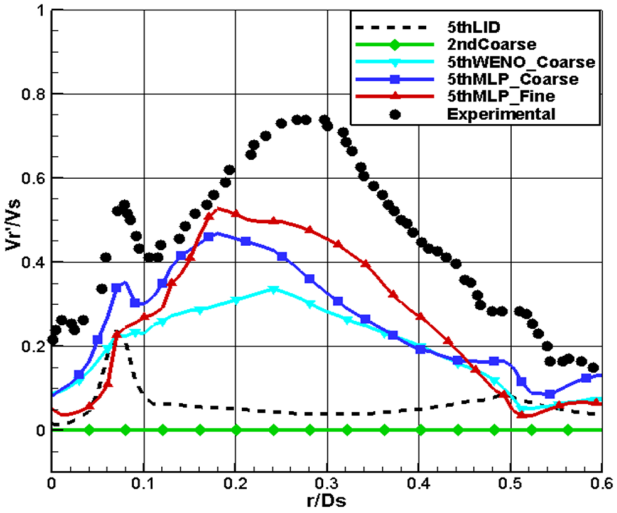

(b) X/Ds = 0.02

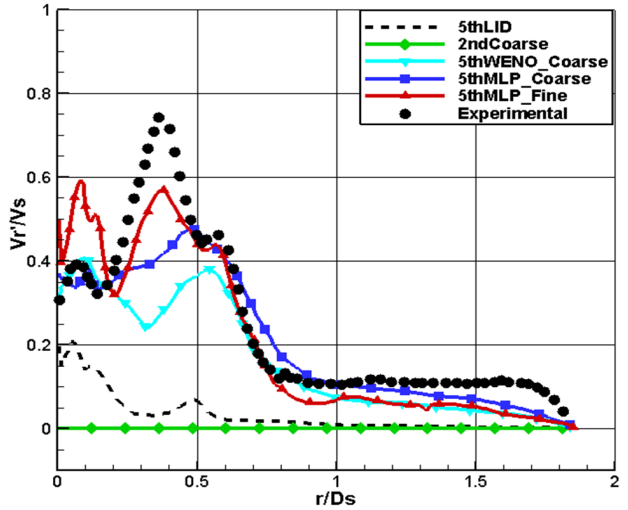

(c) X/Ds = 0.27

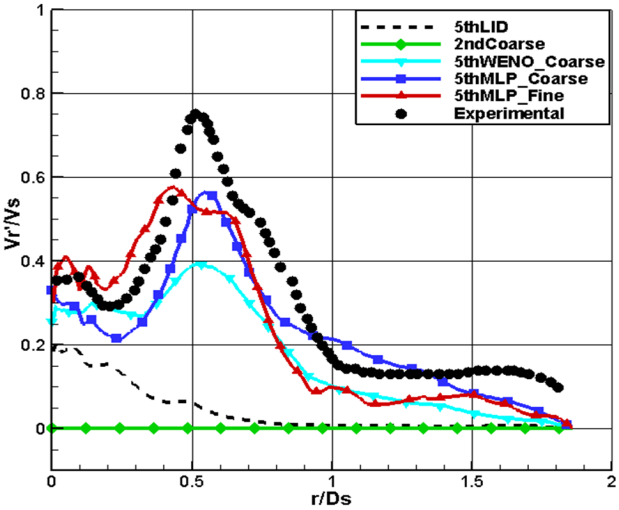

(d) X/Ds = 0.53

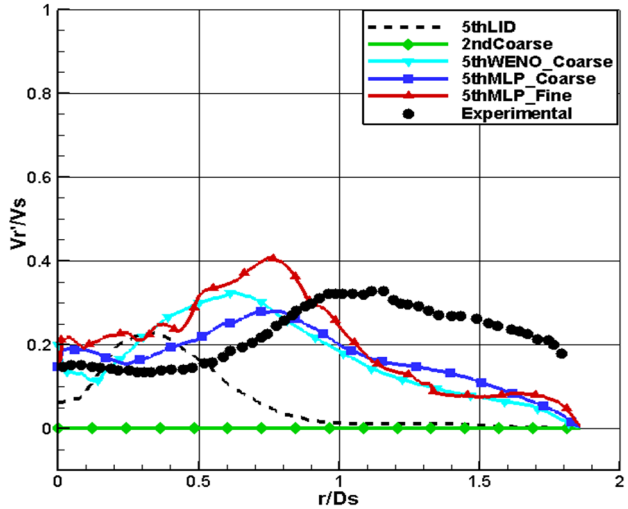

(e) X/Ds = 1.06

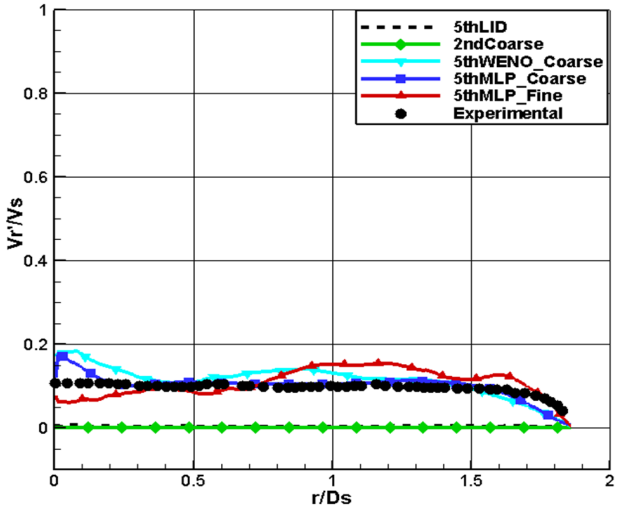

(f) X/Ds = 2.65

Figure 5.10: Radial rms velocity profiles in the x-r plane at five representative positions

There are two significant peaks in axial velocity profiles at X/Ds = 0 and X/Ds = 0.02 that suggest proper modelling of 3D vortical structures. The first one, associated with the high-mixing region located near the short wall between the swirler and jet ducts, is particularly well captured by 5^{th} Order methods in the coarse grid (note that simulations run in the fine grid with boundary conditions calibrated in the coarse one may be affected, at this location, by substantial errors). The second peak, associated with Secondary Vortices induced by Vortex Breakdown at the lower wall of the swirler, is best computed by 5thMLP_Fine, followed by 5thMLP_Coarse and 5thWENO_Coarse. In fact, this trend is also kept in radial velocity profiles, where generally the 5thMLP_Coarse case yields slightly better results than the 5thWENO_Coarse one.

The great performance of 5^{th} Order methods can be observed again in axial and radial rms velocity profiles near the front edge and middle section of the CRZ (X/Ds = 0.27 and X/Ds = 0.53). Here, all peaks associated with shear layers enhanced by Secondary Vortices and PVC perturbations are very well captured, denoting proper modelling of such structures. As a consequence, it can be fairly said that both 5^{th} Order schemes proposed, particularly the TVD-MLP one, are suitable for this problem in particular and for problems involving similar physics from a general point of view.

The analysis of the PVC structure needs further support in order to be accurate and reliable. In this way, Figure 5.11 depicts tangential rms velocity profiles, provided that this magnitude is directly related to the position and behaviour of the PVC (see [6]). Indeed, bearing in mind that the PVC extends from the lower swirler exit wall to the rear of the combustion chamber, wrapping the CRZ in a characteristic helical motion, tangential velocity experiences significant perturbations at the edge of the CRZ. Such perturbations are mainly introduced by the PVC, so capturing them is a clear indicator that the PVC is being tracked.

Results near the injector's exit plane, at X/Ds = 0 and X/Ds = 0.02, are not very relevant in the analysis of the PVC, since here rms values are not only affected by this structure, but also by Vortex Breakdown and Secondary Vortices to a similar extent. Nevertheless, the performance of all 5^{th} Order methods (with the exception of 5thLID) is quite good, with little difference between MLP-WENO and Coarse-Fine results. Focusing on stages X/Ds = 0.27 and X/Ds = 0.53, the presence of the PVC is evidenced in Figures 5.11c,d, in the form of smooth peaks at the edge of the CRZ. In this way, Midgley et al. [6] claim that such peaks are mainly caused by the PVC, since perturbations due to the CRZ are contained within the x-r plane (locally, the CRZ axis of rotation has tangential direction) and no additional phenomena affect this region significantly. The physical meaning of these overshoots is simple: the PVC near the edge of the CRZ enhances turbulence due to its coherent periodic motion of precession, inducing a maximum in tangential rms velocity near r/Ds = 0.5. Finally, the PVC is well approximated by 5^{th} Order Reconstruction, specially in the fine grid (overshoots near the axis are not caused by the PVC, but rather by perturbations associated with flow recirculation towards the injector exit).

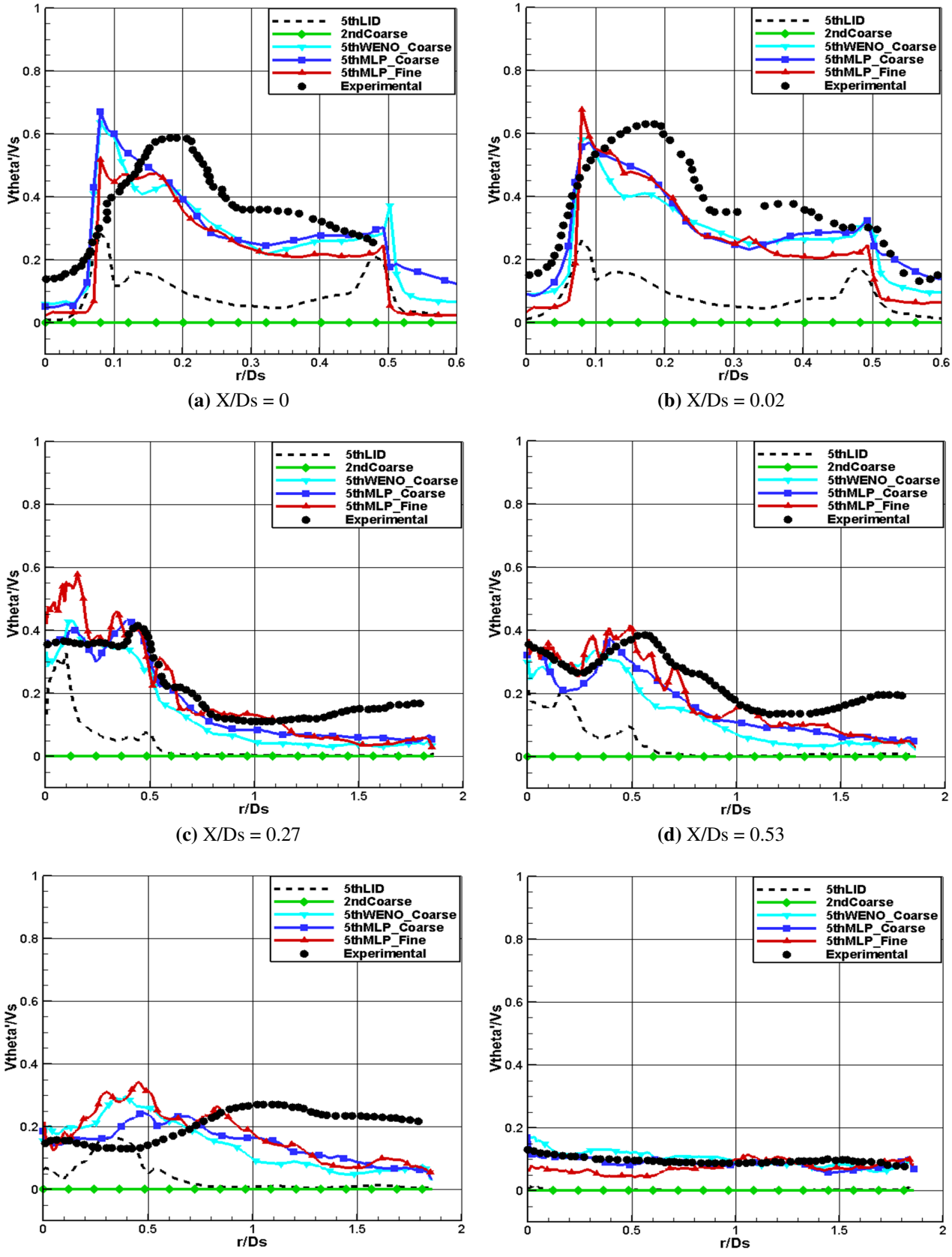

(a) X/Ds = 0

(b) X/Ds = 0.02

(c) X/Ds = 0.27

(d) X/Ds = 0.53

(e) X/Ds = 1.06

(f) X/Ds = 2.65

Figure 5.11: Tangential rms velocity profiles in the x-r plane at five representative positions

One of the main contributions of the present work to the numerical analysis of mixing processes within Dry Low NOx GTU Combustors is the mixing model implemented. As said before, injection conditions generate high-shear layers developing downstream the combustor where enhanced mixing occurs. Therefore, whether the mixing model is suitable or not can be inferred from Turbulent fuel volume fraction profiles at significant locations. Accordingly, Figure 5.12 presents rms Fuel Volume Fraction at X/Ds = 0.27 and X/Ds = 0.53, two representative positions where mixing is enhanced by the CRZ, PVC and inner Secondary Vortices. As seen, 5thMLP_Fine performs the best close to the axis of rotation where higher quantities of fuel are transported. For further radial distances, 5thMLP_Coarse and 5thWENO_Coarse become, at least, as good as the former one. This behaviour may be explained by lower numerical diffusion in the fine grid, which does not damp mixing processes as much as it should.

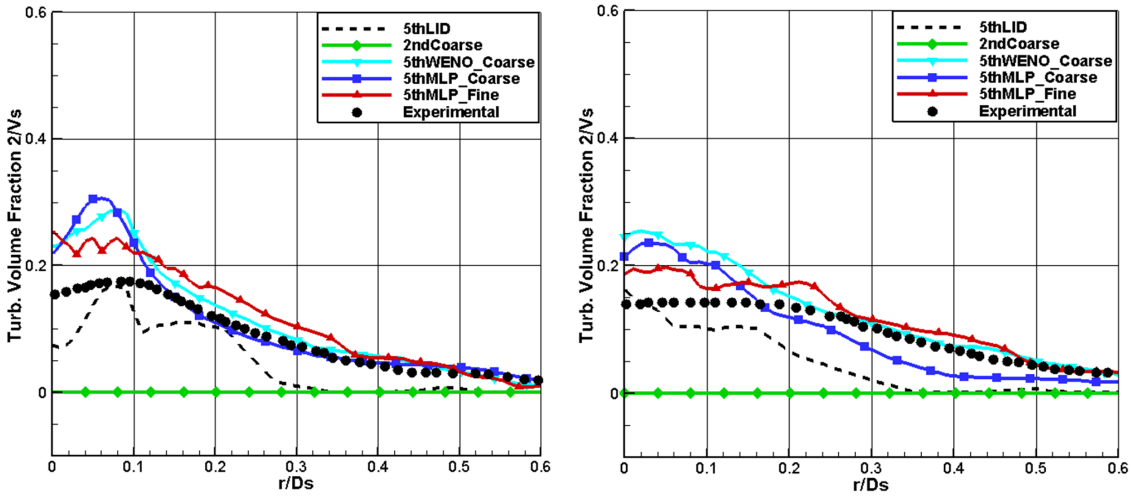

(a) X/Ds = 0.27 **(b)** X/Ds = 0.53

Figure 5.12: Rms Volume Fraction profiles in the x-r plane at two representative positions.

As stated in [70], "the most direct measure of accuracy of modelling of scalar mixing is to compare the predicted turbulent scalar fluxes against the current experimental measurements for the same quantity". Therefore, to conclude the analysis Figure 5.13 depicts axial and radial turbulent fuel volume fraction flux contours in the x-r plane. For reasons of simplicity, only 5thMLP_Coarse case is compared with experimental data, but it was found that all 5^{th} Order approaches (except of 5thLID) yield quite similar results. In light of these figures, it is striking how good the prediction of these magnitudes is, particularly in the axial case where high mixing takes place in the small wall between the injector and swirler exit planes. Both quantitatively and qualitatively, Figure 5.13 confirms that the mixing model and numerical approach considered in this research are suitable for turbulent mixing process in compressible flows.

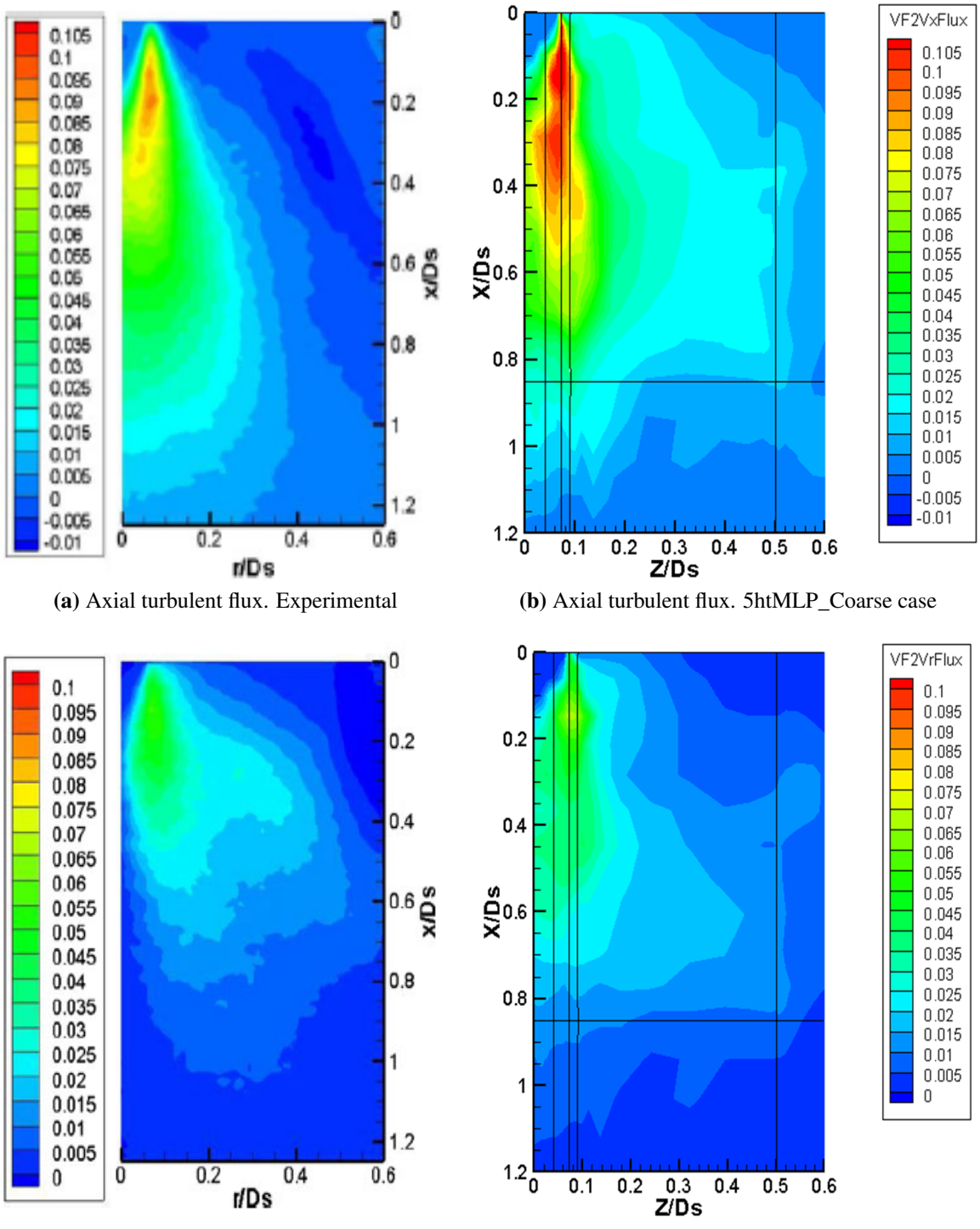

(a) Axial turbulent flux. Experimental

(b) Axial turbulent flux. 5htMLP_Coarse case

(c) Radial turbulent flux. Experimental

(d) Radial turbulent flux. 5thMLP_Coarse case

Figure 5.13: Contours of axial and radial turbulent Volume Fraction 2 fluxes in XY plane

Finally, visual evidence of the PVC structure is shown in Figure 5.14, which illustrates Reynolds decomposition of pressure iso-surfaces with contours of Fuel. As seen, after its inception near the injector's exit plane, it extends downstream the combustion chamber describing a characteristic helical motion with increasing radius, defining the 60-degree

conical surface mentioned in Chapter 1. For the sake of completion, the reader is referred to Figure 2.2 in Section 2.1 to see the resemblance.

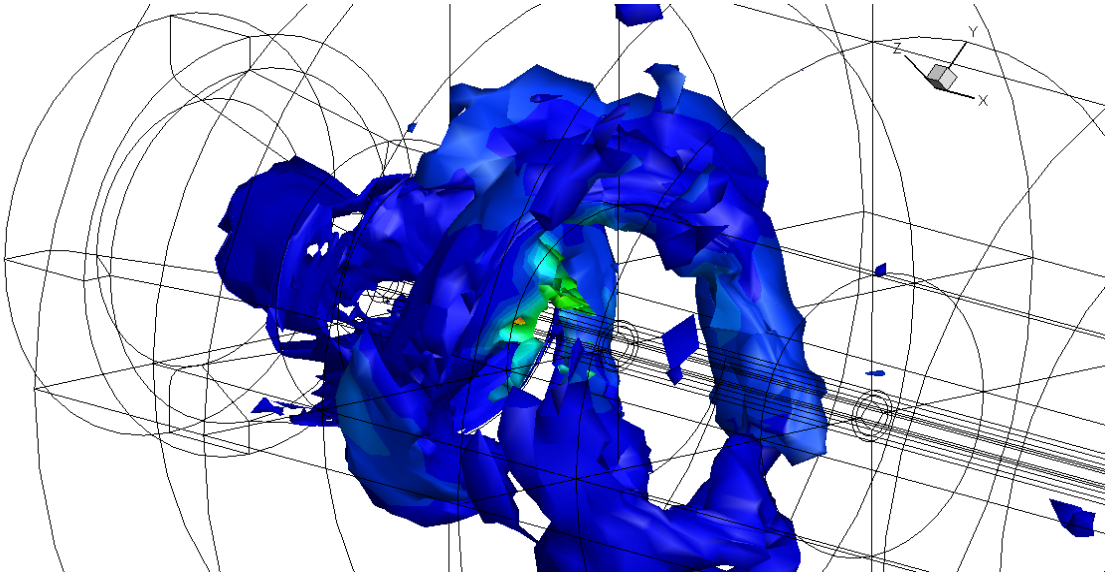

Figure 5.14: Iso-surfaces computed as the difference between averaged pressure and instantaneous pressure at p = -250. Fuel Contours.

5.6 Discussion

The analysis of results strongly supports the idea that FLAMENCO, and thus all physical, mathematical and numerical methods defined in it, is a powerful tool to model physical problems involving turbulent, high-mixing processes. Its applicability to the Dry Low NOx GTU Combustor confirms that FLAMENCO not only is capable of capturing statistically steady structures such as the CRZ and Vortex Breakdown, but it also solves extremely complex intrinsically unsteady structures such as the PVC and Secondary Vortices. In this way, the ability to capture such unsteady phenomena is indicative of the accuracy achieved by the algorithm, since their palpable effects, although very important, are often overlapped by the CRZ.

In terms of the accuracy of each method, generally speaking 5^{th} Order TVD-MLP reconstruction in the fine grid is the best approach. Then, 5^{th} Order TVD-MPL and 5^{th} Order WENO in the coarse grid yield quite similar results, albeit TVD-MLP is slightly less dissipative and therefore a little bit more accurate as a general rule. Here, it is very surprising that provided the low resolution of the coarse mesh (other numerical studies have been conducted using grids with more than 6 million cells), simulations are yet very accurate. Results obtained using 2^{nd} Order Minmod reconstruction are quite unphysical regarding statistically steady features and fails completely in modelling intrinsically unsteady phenomena. Finally, results obtained with the new version of FLAMENCO are undoubtedly better than those computed with old versions where low

numerical dissipation was an issue. In this way, Non-Reflecting Subsonic Inflows and Outflow, Adaptive Reconstruction Scheme at walls and Enhanced Explicit 2^{nd} Order 4-Stages Runge-Kutta seem to succeed in overcoming the problem.

Although comparison with experimental data proves that the methodology chosen is suitable for this kind of problems, some inaccuracies arise at different levels. Obviously, there are plenty of reasons why discrepancies may occur, but only a few are critical. The first one refers to the main physical hypothesis itself: incompressible vs compressible. Indeed, whereas experiments were conducted using water as the working fluid, all numerical computations treated the flow as compressible, concomitant of FLAMENCO numerics. Although Reynolds and Swirl Numbers were matched in order to get comparable results, relevant acoustic perturbations developed only in the simulations. Such perturbations were quickly damped within the combustion chamber where great characteristic lengths dominate, but introduced transient phenomena in confined areas such as the jet injector tube or the small wall between injection ducts. As a consequence, deviations from experimental data were directly induced through transient wave reflections and indirectly induced through inaccuracies in boundary condition calibration, interaction with other flow features, etc.

Another source of errors is the calibration of boundary conditions and initialisation of the problem. First of all, calibration of boundary conditions is at some extent grid-dependent, considering the extreme coarse resolution of the grid used for reasons of computational cost. Since nominal conditions at the injector's exit plane were initially matched with numerical values in the coarse grid and then extrapolated to the fine mesh, small (but not negligible) errors where introduced in the basis of the computation in this last grid. This conclusion is evidenced in Figure 5.15, where tangential mean velocity profiles are plotted for all models at X/Ds = 0.02. In light of this figure it is clear that, for instance, the Swirl number derived from this magnitude is not the same in the fine grid as in the coarse one.

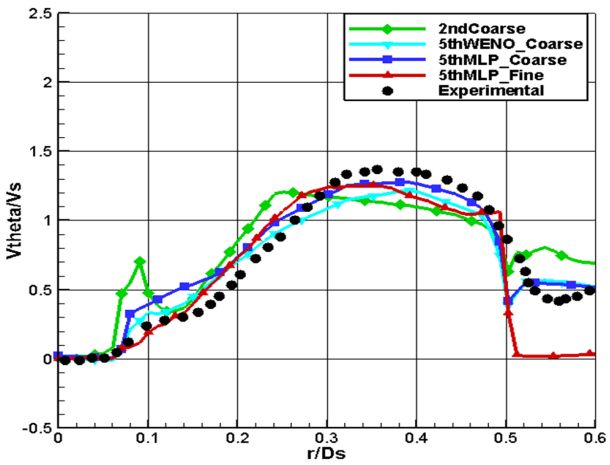

Figure 5.15: Tangential mean velocity at X/Ds = 0.02.

Regarding the general configuration of the problem, the boundary layer within the jet injector is inaccurate in many ways. Due to the short length of the jet injector in conjunction with excessive dissipation of the Adaptive Reconstruction Scheme, the boundary layer is not fully developed, as commented in the previous section. This problem is particularly important in the fine grid, where the jet injector tube only has a 25% of the actual length. As a consequence, wrong velocity profiles at the jet injector exit are computed, introducing additional unphysical phenomena.

Finally, the last (but not least) factor that may affect the accuracy of the approach is related to physical initialisation time, sampling time and number of samples. Firstly, as shown in Table 5.4, 9 characteristic times in the coarse grid and 6 in the fine one were run prior to the sampling stage. In the first case this value is close to the 10 characteristic times typically used in this kind of applications, but in the fine mesh it is almost half the preferable time. As a consequence, larger errors are expected in the 5thMLP_Fine case. In the same way, during the sampling time 100 samples were collected in the coarse grid and 40 in the fine one. Although both are far from the 200 samples recommended in problems of the same nature, in the case of the fine grid this difference is quite significant, having sensitive repercussion on the accuracy of intrinsically unsteady phenomena.

In conclusion, FLAMENCO have shown to perform really well when using 5^{th} Order reconstruction schemes, but poorly when 2^{nd} Order is selected. As for the accuracy of each method, best results are provided by 5^{th} Order TVD-MLP Reconstruction in the fine grid, followed closely by 5^{th} Order TVD-MLP Reconstruction and5^{th} Order WENO Reconstruction in the coarse mesh, which perform similarly (TVD-MLP slightly better). Results are similar in any case and much better than those obtained with old versions of FLAMENCO where low numerical dissipation was a major issue, but the potential of the algorithm in the fine mesh is not fully developed due to additional sources of errors. Finally, 2^{nd} Order Minmod Reconstruction is definitely not suitable for this type of problems.

Chapter 6

Conclusions

6.1 Conclusions

The numerical compressible, multi-species, LES algorithm FLAMENCO has shown to perform very well when it comes to simulate the mixing process within a Dry Low NOx GTU combustor even in an extremely coarse grid. The main three-dimensional structures that define the process, namely the Central Recirculation Zone (CRZ) located in the middle of the chamber, the Precessing Vortex Core (PVC) wrapping the outer edge of the CRZ wall and Secondary Vortical structures, are well captured both quantitatively and qualitatively. This fact indicates the suitability of the algorithm to deal with complex fluid-dynamic processes where turbulent mixing leads to highly unsteady, irregular and heterogeneous structures.

Previous studies addressing the same problem with FLAMENCO fail in producing accurate results due to low numerical dissipation in certain zones of the domain. Indeed, the combination of reflecting subsonic inflows, small cells and adverse flow conditions lead to pressure overshoots that trigger non-physical phenomena. As demonstrated, local energy production is significantly higher than its evacuation, affecting the intensity of trapped bouncing acoustic waves. The present work overcomes this issue by devising different strategies. Firstly, different boundary conditions are implemented in order to decrease the level of total energy reflected inside the domain. In this way, Non-Reflecting, Partially Non-reflecting and Nozzle-type subsonic inflows and outflow are constructed according to acoustic waves propagation. Additionally, an Adaptive Reconstruction Scheme is used in the jet injector wall in order to increase damping of transversal waves. Secondly, a new 5^{th} Order WENO scheme with higher dissipation is also included in the algorithm in order to keep the level of accuracy while damping the excess of local energy associated with acoustic waves. Finally, aiming to decrease the energy accumulated inside the jet injector tube, geometries with a shorter duct are chosen. As a result, an appropriate combination of such strategies lead to a situation where the local energy generated is much lower, being balanced by the global dissipation of the scheme. In the present work results were obtained utilising a combination of Non-reflecting Subsonic Inflows and Outflows, Adaptive Reconstruction Scheme and modified grids with 75% and 25% of the actual jet injector length (in the coarse and fine grids respectively) .

Prior to any simulation in the combustor, the new version of FLAMENCO has been extensively validated through contrasted test cases such as Stationary Contact Wave, Moving Contact Wave, Shock Tube, Kelvin-Helmholtz Instability, 2D Explosion and 3D Explosion. Generally speaking, best performance is achieved with 5^{th} Order TVD-MLP Reconstruction, followed closely by 5^{th} Order WENO Reconstruction and sensitively better than 2^{nd} Order Minmod scheme. In addition to being the most accurate, the TVD-MLP method has another advantage over WENO, since it damps small oscillations near discontinuities significantly faster. As for the computational time, TVD-MLP is a little bit slower than Minmod, but way faster than WENO. Thus, in order to run affordable computations in the combustor, a 1-D WENO scheme is employed instead, sacrificing simplicity for accuracy. Finally, Low Numerical Dissipation strategies have been validated using the actual jet injector duct discharging in a basic combustion chamber with no swirl flow. This test shows that the flow field becomes much more relaxed when such strategies are utilised, damping both longitudinal and transversal acoustic perturbations and leading to a physically correct thermodynamic state after the initial transient.

Regarding the application to the Dry Low NOx GTU Combustor, a broad range of numerical results have been extracted and compared with contrasted experimental data. Whereas the overall flow within the combustor was inaccurately predicted by previous versions of FLAMENCO, the new version of the algorithm has proved to be really precise. Accurate axial mean velocity profiles reveal the ability of FLAMENCO to compute Vortex Breakdown, separation and CRZ very well. In the same way, mean Fuel Volume Fraction profiles suggest proper treatment of multi-species mixing in high-shear regions. Regarding intrinsically unsteady structures (PVC and Secondary Vortices), the good agreement in axial, radial and tangential rms velocity profiles indicates accurate prediction of them, even in the coarse grid under consideration, suggesting proper treatment of turbulence and vortical structures. Finally, similarities with experimental axial and radial scalar turbulent fluxes observed confirm even further that the mixing model employed is suitable to compute highly turbulent flows with strong shear layers.

6.2 Contributions and Suggestions for future work

From a general point of view, this work contributes, to some extent, to the simulation of mixing processes in highly compressible, turbulent environments. In particular, some ideas are addressed

- Description, development and validation of an accurate algorithm based on LES, 5-Equiation Transport Model with iso-baric closure devised to deal with three-dimensional, compressible, turbulent, unsteady, multi-species flows.
- Definition of successful numerical strategies, including boundary conditions,

adaptive reconstruction schemes and enhance time integration schemes, that overcome Low Numerical Dissipation issues arising in old versions of the algorithm.

- Introduction of different reconstruction schemes into the code in order to broaden its numerical capacity.
- Application to the Dry Low NOx GTU Combustor, obtaining accurate results and evidencing the potential of FLAMENCO.
- In-depth analysis and characterisation of complex physical processes taking place within the Dry Low NOx GTU Combustor.

There are many fields in the present approach subjected to further research. Firstly, although the Adaptive Reconstruction Scheme performs its task fairly well, its definition is somehow basic and "ad hoc". In order to make it more consistent physically and mathematically speaking, alternative (or formalised) ways must be introduced, leading to a well-posed model from all points of view. Secondly, the initial set up and boundary condition calibration must be analysed in depth to produce accurate boundary layers in the jet injector and nominal Swirl and Reynolds Numbers at the Swirler exit. In this way, variable specification at boundaries must be either provided for each configuration separately or introduced somehow in the plane of interest. Also, alternative jet injector geometries must be investigated to allow full boundary layer development while keeping confined energy at physical levels. Finally, another issue to be reviewed in future studies is related to computational efficiency. For given resources, the initialisation time and number of samples can only be increased if some methods are rearranged within FLAMENCO. Although it is a difficult task, improvement is completely feasible provided that primary analysis shown an overall computational efficiency of 60%. As for enhancing techniques, redefinition of FLAMENCO to work with GPUs in a parallel environment is something that should be borne in mind for future developments.

Bibliography

[1] L. B. Davis ; S. H. Black. Dry low nox combustion systems for ge heavy-duty gas turbines. *GE Power Systems*, GER-3568G, 2000.

[2] R. M. Washam. Dry low nox combustion system for utility gas turbine. *ASME Paper*, 83-JPGC-GT-13, 1983.

[3] K. Liu ; J. P. Wood ; E. R. Buchanan ; P. Martin ; V. E. Sanderson. Biodiesel as an alternative fuel in siemens dry low emissions combustors: Atmospheric and high pressure rig testing. *J. Eng. Gas Turbines Power*, 132(1), 2009.

[4] P. C. Miles. Turbulent flow structures in direct-injection, swirl-supported diesel engies. *Flow and Combustion in Reciprocating Engines, Springer*, pages 173–256, 2009.

[5] L. Yang ; Q. Fu ; W. Zhang ; M. Du ; B. Xu. Spray characteristics of gelled propellants in swirl injectors. *Fuel*, 97:253–261, 2012.

[6] K. Midgley ; A. Spencer ; J. J. McGuirk. Unsteady flow structures in radial swirler fed fuel injectors. *Journal of Engineering for Gas Turbines and Power*, 127:755–764, 2004.

[7] B. Thornber. Implicit large eddy simulation for unsteady multi-component compressible turbulent flows. *PhD Thesis*, 2007.

[8] P. Aguado. Implicit large-eddy simulation of the mixing process in a gas-turbine swirl injector. *MSc Thesis*, 2012.

[9] Q. Fu ; L. Yang. Theoretical investigation of the dynamics of a gas-liquid coaxial swirl injector. *Journal of Propulsion and Power*, 27(1), 2011.

[10] S. A. Ahmed. Three component velocity measurements of an isothermal confined swirling flow. *Institution of Mechanical Engineerings*, 211G, 1996.

[11] N. Syred ; J. M. Beer. Combustion in swirling flows: A review. *Combustion and Flame*, 23:143–201, 1974.

[12] A. Valera-Medina ; M. Abdulsada ; N. Syred ; A. Griffiths. Studies of large coherent structures and their effects on swirl combustion. *48th AIAA Aerospace Sciences Meeting Including the New Horizons Forum and Aerospace Exposition*, (4-7), 2010.

[13] A. Valera-Medina ; N. Syred ; A. Griffiths. Characterisation of large coherent structures in a swirl burner. *46th AIAA Aerospace Sciences Meeting and Exhibit*, pages 7–10, 2008.

[14] J. S. Perisetty ; M. V. Panchagnula ; J. Cui. Development of cfd model for a swirl stabilized spray combustor. *Proceedings of ASME IMECE: International Mechanical Engineering Conference and Exposition*, 2006.

[15] N. Syred ; W. Fick; T. ODoherty ; A. J. Griffiths. The effect of the precessing vortex core on combustion in a swirl burner. *Combustion Science and Technology*, 125:139–157, 1997.

[16] S. Rouxa ; G. Lartiguea ; T. Poinsot ; U. Meier ; C. Berat. Studies of mean and unsteady flow in a swirled combustor using experiments, acoustic analysis, and large eddy simulations. *Combustion and Flame*, 141:40–54, 2005.

[17] Y. Al-Abdeli ; A. Masri. Stability characteristics and flow fields of turbulent non-premixed swirling flames. *Combustion Theory and Modeling*, 7(4):655–766, 2003.

[18] M. R. Baer ; J. W. Nunziato. A two-phase mixture theory for the deflagration-to-detonation transition (ddt) in reactive granular materials. *International Journal of Multiphase Flow*, 12(6):861–889, 1986.

[19] R. Saurel ; R. Abgrall. A multiphase godunov method for compressible multifluid and multiphase flows. *Journal of Computational Physics*, 150:425–467, 1998.

[20] A. Murrone ; H. Guillard. A five equation reduced model for compressible two phase flow problems. *Journal of Computational Physics*, 202:664–698, 2004.

[21] G. Allaire ; S. Clerc ; S. Kokh. A five-equation model for the simulation of interfaces between compressible fluids. *Journal of Computational Physics*, 181:577–616, 2002.

[22] D. L. Brown. An unsplit godunov method for systems of conservation laws on curvilinear overlapping grids. *Mathematical and Computer Modeling*, 20(10/11):29–48, 1994.

[23] B. Kreiss. Construction of a curvilinear grid. *SIAM Journal of Scientific and Statistical Computing*, 4:270–279, 1983.

[24] P. D. Thomas ; C. K. Lombard. Geometric conservation law and its application to flow computations on moving grids. *AIAA*, 17(10):1030–1037, 979.

[25] E. F. Toro. Riemann solvers and numerical methods for fluid dynamics. *Springer-Verlag, Berlin*, 1997.

[26] S. K. Godunov. A difference method for the numerical computation of discontinuous solutions of the equations of fluid dynamics. *Math. Sbornik*, 47:271–290, 1959.

[27] S. K. Godunov ; A. Zabrodine ; M. Ivanov ; A. Kraiko ; G. Prokopov. Resolution numerique des problemes multidimensionnels de la dynamique des gaz. *Editions de Moscou*, 1979.

[28] R. J. LeVeque. Numerical methods for conservation laws. *Lectures in Mathematics ETH Zurich*, 1994.

[29] Y. Shimada ; B. Thornber ; D. Drikakis. High-order implicit large eddy simulation of gaseous fuel injection and mixing of a bluff body burner. *Computers and Fluids*, 44:229–237, 2011.

[30] B. Thornber ; A. Mosedale ; D. Drikakis. Implicit large-eddy simulation of a deep cavity using high resolution methods. *Journal of Computational Physics*, 226(2):1902–1929, 2008.

[31] B. Einfeldt. On godunov-type methods for gas dynamics. *SIAM J. Numer. Anal.*, 25:294–318, 1988.

[32] B. Einfeldt ; C. D. Munz ; P. L. Roe ; B. Sjogreen. On godunov-type methods near low densities. *Journal of Computational Physics*, 92:273–295, 1991.

[33] P. Batten ; N. Clarke ; C. Lambert ; D.M. Causon. On the choice of wave speeds for the hllc riemann solver. *SIAM J. Sci.Comput.*, 18:1553–1570, 1997.

[34] A. Bagabir ; D. Drikakis. Numerical experiments using high-resolution schemes for unsteady, inviscid, compressible flows. *Computational Methods for Applied Mechanical Engineering*, 193:4675–4705, 2004.

[35] A. A. Amsden ; P. J. O'Rourke ; T. D. Butler. Kiva-ii: A computer program for chemically reactive flows with sprays. *Los Alamos National Laboratory*, 1989.

[36] B. van Leer. Towards the ultimate conservative difference scheme i. the quest for monotonicity. *Lecture Notes in Physics*, 18:163–168, 1973.

[37] B. van Leer. Towards the ultimate conservative difference scheme ii. mono-tonicity and conservation combined in a second order scheme. *Journal of Computational Physics*, 14:361–370, 1974.

[38] B. van Leer. Towards the ultimate conservative difference scheme iii.upstream-centered finite difference schemes for ideal compressible flow. *Journal of Computational Physics*, 23:263–275, 1977.

[39] B. van Leer. Towards the ultimate conservative difference scheme iv. a new approach to numerical convection. *Journal of Computational Physics*, 26:276–299, 1977.

[40] B. van Leer. Towards the ultimate conservative difference scheme v. a second order sequel to godunov's method. *Journal of Computational Physics*, 32:101–136, 1979.

[41] A. Harten. High resolution schemes for hyperbolic conservation laws. *Journal of Computational Physics*, 49:357–393, 1983.

[42] P. K. Sweby. High resolution schemes using flux limiters for hyperbolic conservation laws. *SIAM Journal Numerical Analysis*, 21:995–1011, 1984.

[43] P. L. Roe. Numerical algorithms for the linear wave equation. *Technical Report 81047, Royal Aircraft Establishment*, 1984.

[44] P. L. Roe. Discrete models for the numerical analysis of time-dependent multidimensional gas dynamics. *Journal of Computational Physics*, 63:458–476, 1986.

[45] A. Majda and S. Osher. Numerical viscosity and entropy condition. *Communications in Pure and Applied Mathematics*, 32:797–838, 1979.

[46] J. Casper. A finite-volume high-order eno scheme for two-dimensional hyperbolic systems. *Journal of Computational Physics*, 106:62–76, 1993.

[47] A. Harten. Uniformly high order accurate essentially non-oscillatory schemes, iii. *Journal of Computational Physics*, 71:231–303, 1987.

[48] F. Grasso ; S. Pirozzoli. Shock wave - thermal inhomogeneity interactions: analysis and numerical simulations of sound generation. *Physics of Fluids*, 12(1):205–219, 2000.

[49] E. Johnsen ; T. Colonius. Implementation of weno schemes in compressible multicomponent flow problems. *Journal of Computational Physics*, 219:715–732, 2006.

[50] R. Burger ; A. Kozakevicius. Adaptive multiresolution weno schemes for multi-species kinematic flow models. *Journal of Computational Physics*, 224:1190–1222, 2007.

[51] C. Hu ; C. W. Shu. Weighted essentially non-oscillatory schemes on triangular meshes. *Journal of Computational Physics*, 150:97–127, 1999.

[52] G. S. Jiang ; C. W. Shu. Efficient implementation of weighted eno schemes. *Journal of Computational Physics*, 126:202–228, 1996.

[53] C. W. Shu. Total variation diminishing time discretisations. *SIAM Journal of Statistical Computing*, 9(6), 1988.

[54] S. V. Mikhailov ; A. A. Savelyev. Comparison of tvd and weno schemes in the case of wave packet transport and vortex numerical diffusion problems. *Jour. Matem. Mod.*, 23(11):99–110, 2011.

[55] C. W. Shu. High order finite difference and finite volume weno schemes and discontinuous galerkin methods for cfd. *ICASE Report*, 11, 2001.

[56] V. A. Titarev ; E. F. Toro. Finite-volume weno schemes for three-dimensional conservation laws. *Journal of Computational Physics*, 201(1):238–260, 2004.

[57] J. Shi ; C. Hu ; C. W. Shu. A technique for treating negative weights in weno schemes. *Journalof Computational Physics*, 175:108–127, 2002.

[58] A. Harten ; S. Osher. Uniformily high-order accurate nonoscillatory schemes i. *SIAM Journal of Numerical Analysis*, 24(2):279–309, 1987.

[59] A. Kurganov ; E. Tadmor. Solution of two-dimensional riemann problems for gas dynamics without riemann problem solvers. *Dept. Of Mathematics, University of Michigan*, 2000.

[60] C. Kim K. H. Kim. Accurate, efficient and monotonic numerical methods for multi-dimensional compressible flows part i: Spatial discretization. *Journal of Computational Physics*, 208:527–569, 2005.

[61] C. Kim K. H. Kim. Accurate, efficient and monotonic numerical methods for multi-dimensional compressible flows part ii: Multi-dimensional limiting process. *Journal of Computational Physics*, 208:570–615, 2005.

[62] S. Karni. Multicomponent flow calculations by a consistent primitive algorithm. *Journal of Computational Physics*, 112(31), 1994.

[63] R. Abgrall. How to prevent pressure oscillations in multicomponent flow calculations: A quasi-conservative approach. *Journal of Coputational Physics*, 125(150), 1996.

[64] T. H. Pulliam. Solution methods in computational fluid dynamics. *NASA Ames Research Center*.

[65] E. Giacomazzi. Turbulent combustion modelling and simulation. *Combustion Chemistry and Fluidynamics PhD Course*, 2009.

[66] J. Blazek. Computational fluid dynmaics: Principles and applications. *Elsevier*, 2001.

[67] T. Poinsot ; D. Veynante. Theoretical and numerical combustion. *R.T. edwards, Inc.*, 2001.

[68] K. W. Thomson. Time- dependent boundary conditions for hyperbolic systems, ii. *Journal of Computational Physics*, 89:439–461, 1990.

[69] T. Pulliam ; J. Steger. Implicit finite-difference simulations of three-dimensional compressible flow. *AIAA*, 18(2).

[70] L. Cheng ; M. Dianat ; A. Spencer ; J. J. McGuirk. Validation of les predictions of scalar mixing in high-swirl fuel injector flows. *Flow Turbulence Combustion*, 88:143–168, 2012.

[71] G. S. Jiang ; C. W. Shu. Efficient implementation of weighted eno schemes. *Journal of Computational Physics*, 126:202–212, 1996.

APPENDIX A

The 5-Equation Transport Model can be easily derived from the 7-Equation Multifluid Model of Nunziato [18] for relaxation times approaching asymptotically to 0. The demonstration is presented here, without any loss of generality, for two phases and one dimension. First, let the 7-Equation Multifluid Model be represented as

$$\frac{\partial (z_1\rho_1)}{\partial t} + \frac{\partial (z_1\rho_1 u_1)}{\partial x} = 0 \tag{A.1}$$

$$\frac{\partial (z_1\rho_1 u_1)}{\partial t} + \frac{\partial (z_1\rho_1 u_1 u_1)}{\partial x} + \frac{\partial (z_1 p_1)}{\partial x} = p^I \frac{\partial z_1}{\partial x} + \lambda (u_2 - u_1) \tag{A.2}$$

$$\frac{\partial (z_1\rho_1 E_1)}{\partial t} + \frac{\partial [(z_1\rho_1 E_1 + z_1 p_1) u_1]}{\partial x} = p^I u^I \frac{\partial z_1}{\partial x} + \mu p^I (p_2 - p_1) + \lambda u^I (u_2 - u_1) \tag{A.3}$$

$$\frac{\partial (z_2\rho_2)}{\partial t} + \frac{\partial (z_2\rho_2 u_2)}{\partial x} = 0 \tag{A.4}$$

$$\frac{\partial (z_2\rho_2 u_2)}{\partial t} + \frac{\partial (z_2\rho_2 u_2 u_2)}{\partial x} + \frac{\partial (z_2 p_2)}{\partial x} = p^I \frac{\partial z_2}{\partial x} - \lambda (u_2 - u_1) \tag{A.5}$$

$$\frac{\partial (z_2\rho_2 E_2)}{\partial t} + \frac{\partial [(z_2\rho_2 E_2 + z_2 p_2) u_2]}{\partial x} = p^I u^I \frac{\partial z_2}{\partial x} - \mu p^I (p_2 - p_1) - \lambda u^I (u_2 - u_1) \tag{A.6}$$

$$\frac{\partial z_2}{\partial t} + u^I \frac{\partial z_2}{\partial x} = \mu (p_2 - p_1) \tag{A.7}$$

where it has been assumed that $p_1^I = p_2^I = p^I$, $u_1^I = u_2^I = u^I$, E is the Total Energy and the Volume Fraction satisfies the condition

$$z_1 + z_2 = 1 \tag{A.8}$$

Conservative system (A.1)-(A.6) can be recast and rearranged in primitive variables as

$$z_1 \underbrace{\left(\frac{\partial \rho_1}{\partial t} + u_1 \frac{\partial \rho_1}{\partial x} \right)}_{\frac{D_1\rho_1}{Dt}} = \rho_1 \left(u^I - u_1\right) \frac{\partial z_1}{\partial x} - \rho_1 z_1 \frac{\partial u_1}{\partial x} + \rho_1 \mu (p_2 - p_1) \tag{A.9}$$

$$z_2 \underbrace{\left(\frac{\partial \rho_2}{\partial t} + u_2 \frac{\partial \rho_2}{\partial x} \right)}_{\frac{D_2\rho_2}{Dt}} = -\rho_2 \left(u^I - u_2\right) \frac{\partial z_2}{\partial x} - \rho_2 z_2 \frac{\partial u_2}{\partial x} - \rho_2 \mu (p_2 - p_1) \tag{A.10}$$

$$z_1\rho_1 \frac{D_1 u_1}{Dt} = -\frac{\partial (z_1 p_1)}{\partial x} + p^I \frac{\partial z_1}{\partial x} + \lambda (u_2 - u_1) \tag{A.11}$$

$$z_2\rho_2 \frac{D_2 u_2}{Dt} = -\frac{\partial (z_2 p_2)}{\partial x} + p^I \frac{\partial z_2}{\partial x} - \lambda (u_2 - u_1) \tag{A.12}$$

$$z_1 \frac{D_1 p_1}{Dt} + z_1 \rho_1 a_1^2 \frac{\partial u_1}{\partial x} = \rho_1 a_{1_I}^2 \left(u^I - u_1\right) \frac{\partial z_1}{\partial x} + \mu \rho_1 a_{1_I}^2 \left(p_2 - p_1\right) + \frac{\lambda}{\chi_{p_1} \rho_1} \left(u^I - u_1\right) \left(u_2 - u_1\right) \tag{A.13}$$

$$z_2 \frac{D_2 p_2}{Dt} + z_2 \rho_2 a_2^2 \frac{\partial u_2}{\partial x} = \rho_2 a_{2_I}^2 \left(u^I - u_2\right) \frac{\partial z_2}{\partial x} - \mu \rho_2 a_{2_I}^2 \left(p_2 - p_1\right) - \frac{\lambda}{\chi_{p_2} \rho_2} \left(u^I - u_2\right) \left(u_2 - u_1\right) \tag{A.14}$$

$$\underbrace{\frac{\partial z_2}{\partial t} + u^I \frac{\partial z_2}{\partial t}}_{\frac{D_I z_2}{Dt}} = \mu \left(p_2 - p_1\right) \tag{A.15}$$

$$z_1 + z_2 = 1 \tag{A.16}$$

where

$$a_k^2 = \frac{\left(\frac{p_k}{\rho_k^2} - \chi_{\rho_k}\right)}{\chi_{p_k}} \;\; ; \;\; a_{k_I}^2 = \frac{\left(\frac{p_I}{\rho_k^2} - \chi_{\rho_k}\right)}{\chi_{p_k}} \quad k = 1,2 \tag{A.17}$$

$$\chi_{p_k} = \left(\frac{\partial \varepsilon_k}{\partial p_k}\right)_{\rho_k = const.} \;\; ; \;\; \chi_{\rho_k} = \left(\frac{\partial \varepsilon_k}{\partial \rho_k}\right)_{p_k = const.} \quad k = 1,2 \;\; ; \;\; \varepsilon \equiv Internal\ energy \tag{A.18}$$

After a transient perturbation, the system develops to restore equilibrium in a characteristic time ε determined by the relaxation coefficients λ and μ. In the limit $\lambda \to \infty$; $\mu \to \infty$, the relationship between the relaxation time and the relaxation coefficients can be written as

$$\varepsilon = \frac{\lambda^*}{\lambda} \;\; ; \;\; \varepsilon = \frac{\mu^*}{\mu} \tag{A.19}$$

where parameters λ^*, μ^* are coefficients introduced for dimensional consistency. Using the Theory of Perturbations, in the mentioned limit $\varepsilon \to 0$ velocities and pressures can be expressed as

$$\left.\begin{array}{l} p_1 = p - \frac{1}{2}\varepsilon p_0 \;\; ; \;\; u_1 = u - \frac{1}{2}\varepsilon u_0 \\ p_2 = p + \frac{1}{2}\varepsilon p_0 \;\; ; \;\; u_2 = u - \frac{1}{2}\varepsilon u_0 \end{array}\right\} \to \begin{array}{l} p_2 - p_1 = \varepsilon p_0 \\ u_2 - u_1 = \varepsilon u_0 \end{array} \tag{A.20}$$

Note that if ε has dimension of time, the reference values $p_0$and u_0 have dimension of pressure and velocity divided by time, respectively. Introducing (A.19) and (A.20) in system (A.9)-(A.16) and bearing in mind that it is $a_1 = a_{1_I}$; $a_2 = a_{2_I}$, the resulting expression reads

$$z_1 \frac{D_1 \rho_1}{Dt} = -\rho_1 z_1 \frac{\partial u_1}{\partial x} + \rho_1 \frac{u_0}{2} \frac{\lambda^*}{\lambda} \frac{\partial z_1}{\partial x} + \rho_1 \mu^* p_o \tag{A.21}$$

$$z_2 \frac{D_2 \rho_2}{Dt} = -\rho_2 z_2 \frac{\partial u_2}{\partial x} - \rho_2 \frac{u_0}{2} \frac{\lambda^*}{\lambda} \frac{\partial z_2}{\partial x} - \rho_2 \mu^* p_o \tag{A.22}$$

$$z_1\rho_1\frac{D_1u_1}{Dt} = -z_1\frac{\partial p_1}{\partial x} + \frac{1}{2}p_0\frac{\mu^*}{\mu}\frac{\partial z_1}{\partial x} + u_0\lambda^* \tag{A.23}$$

$$z_2\rho_2\frac{D_2u_2}{Dt} = -z_2\frac{\partial p_2}{\partial x} - \frac{1}{2}p_0\frac{\mu^*}{\mu}\frac{\partial z_2}{\partial x} - u_0\lambda^* \tag{A.24}$$

$$z_1\frac{D_1p_1}{Dt} + z_1\rho_1a_1^2\frac{\partial u_1}{\partial x} = \rho_1a_1^2\frac{u_0}{2}\frac{\lambda^*}{\lambda}\frac{\partial z_1}{\partial x} + \rho_1a_1^2p_0\mu^* + \frac{1}{2}\frac{u_0^2}{\lambda}\frac{(\lambda^*)^2}{\chi_{p_1}\rho_1} \tag{A.25}$$

$$z_2\frac{D_2p_2}{Dt} + z_2\rho_2a_2^2\frac{\partial u_2}{\partial x} = -\rho_2a_2^2\frac{u_0}{2}\frac{\lambda^*}{\lambda}\frac{\partial z_2}{\partial x} - \rho_2a_2^2p_0\mu^* - \frac{1}{2}\frac{u_0^2}{\lambda}\frac{(\lambda^*)^2}{\chi_{p_2}\rho_2} \tag{A.26}$$

$$\frac{D_Iz_2}{Dt} = p_0\mu^* \tag{A.27}$$

Now, making (A.23)+(A.24), (A.25)+(A.26) and (A.25)-(A.26), neglecting terms $\propto \frac{1}{\lambda}$; $\propto \frac{1}{\mu}$ (when $\lambda \to \infty$; $\mu \to \infty$), and taking $u_2 = u_1 = u$; $p_2 = p_1 = p$

$$z_1\frac{D_1\rho_1}{Dt} = -\rho_1z_1\frac{\partial u}{\partial x} + \rho_1\mu^*p_o \tag{A.28}$$

$$z_2\frac{D_2\rho_2}{Dt} = -\rho_2z_2\frac{\partial u}{\partial x} - \rho_2\mu^*p_o \tag{A.29}$$

$$(z_1\rho_1 + z_2\rho_2)\frac{Du}{Dt} = -\frac{\partial p}{\partial x}(z_1 + z_2) \tag{A.30}$$

$$(z_1 + z_2)\frac{Dp}{Dt} + \left(z_1\rho_1a_1^2 + z_2\rho_2a_2^2\right)\frac{\partial u}{\partial x} = \left(\rho_1a_1^2 - \rho_2a_2^2\right)p_o\mu^* \tag{A.31}$$

$$\frac{D(p_2 - p_1)}{Dt} = \frac{D(p-p)}{Dt} = 0 = -\left(\frac{\rho_2a_2^2}{z_2} + \frac{\rho_1a_1^2}{z_1}\right)p_0\mu^* + \left(\rho_1a_1^2 - \rho_2a_2^2\right)\frac{\partial u}{\partial x} \tag{A.32}$$

$$\frac{Dz_1}{Dt} = p_0\mu^* \tag{A.33}$$

$$\textit{From } (A.28),\ (A.33) \implies \frac{\partial(z_1\rho_1)}{\partial t} + \frac{\partial(z_1\rho_1u)}{\partial x} = 0 \tag{A.34}$$

$$\textit{From } (A.29),\ (A.33) \implies \frac{\partial(z_2\rho_2)}{\partial t} + \frac{\partial(z_2\rho_2u)}{\partial x} = 0 \tag{A.35}$$

$$(A.30) \xrightarrow[\substack{\rho = \sum_{k=1}^{2} z_k\rho_k \\ \sum_{k=1}^{2} z_k = 1}]{} \frac{\partial u}{\partial t} + u\frac{\partial u}{\partial x} = -\frac{1}{\rho}\frac{\partial p}{\partial x} \tag{A.36}$$

$$\textit{From } (A.32) \implies p_0\mu^* = \left(\frac{\rho_1a_1^2 - \rho_2a_2^2}{\frac{\rho_1a_1^2}{z_1} + \frac{\rho_2a_2^2}{z_2}}\right)\frac{\partial u}{\partial x} \tag{A.37}$$

Introducing equation (A.37) in (A.31)

$$\frac{Dp}{Dt} + \underbrace{\left(z_1\rho_1a_1^2 + z_2\rho_2a_2^2 - \frac{\left(\rho_1a_1^2 - \rho_2a_2^2\right)^2}{\frac{\rho_2a_2^2}{z_2} + \frac{\rho_1a_1^2}{z_1}}\right)}_{\rho\widehat{a}^2 = \frac{1}{\sum_{k=1}^{2}\frac{z_k}{\rho_ka_k^2}}}\frac{\partial u}{\partial x} = \frac{Dp}{Dt} + \rho\widehat{a}^2\frac{\partial u}{\partial x} = 0 \tag{A.38}$$

and from (A.33)

$$\frac{Dz_2}{Dt} = \left(\frac{\rho_1 a_1^2 - \rho_2 a_2^2}{\frac{\rho_2 a_2^2}{z_2} + \frac{\rho_1 a_1^2}{z_1}} \right) \frac{\partial u}{\partial x} \tag{A.39}$$

Now, employing the relationships for the mixture

$$\rho = \sum_{k=1}^{2} z_k \rho_k \ ; \ \sum_{k=1}^{2} z_k = 1 \tag{A.40}$$

Equations(A.34)-(A.39) can be presented as the 5-Equation Reduced Model for Compressible Flows

$$\frac{\partial (z_1 \rho_1)}{\partial t} + \frac{\partial (z_1 \rho_1 u)}{\partial x} = 0 \tag{A.41}$$

$$\frac{\partial (z_2 \rho_2)}{\partial t} + \frac{\partial (z_2 \rho_2 u)}{\partial x} = 0 \tag{A.42}$$

$$\frac{\partial u}{\partial t} + u \frac{\partial u}{\partial x} = -\frac{1}{\rho} \frac{\partial p}{\partial x} \tag{A.43}$$

$$\frac{Dp}{Dt} + \rho \widehat{a}^2 \frac{\partial u}{\partial x} = 0 \tag{A.44}$$

$$\frac{Dz_2}{Dt} = \left(\frac{\rho_1 a_1^2 - \rho_2 a_2^2}{\frac{\rho_2 a_2^2}{z_2} + \frac{\rho_1 a_1^2}{z_1}} \right) \frac{\partial u}{\partial x} \tag{A.45}$$

Forcing system (A.41)-(A.45) to work only with immiscible phases, where relationship

$$z_1 z_2 = 0 \ ; \ \forall x,t \tag{A.46}$$

implies

$$\left(\frac{\rho_1 a_1^2 - \rho_2 a_2^2}{\frac{\rho_2 a_2^2}{z_2} + \frac{\rho_1 a_1^2}{z_1}} \right) = \underbrace{z_1 z_2}_{=0} \underbrace{\left(\frac{\rho_1 a_1^2 - \rho_2 a_2^2}{z_1 \rho_2 a_2^2 + z_2 \rho_1 a_1^2} \right)}_{=finite} = 0 \rightarrow \rho \widehat{a}^2 = z_1 \rho_1 a_1^2 + z_2 \rho_2 a_2^2 = \rho a^2 \tag{A.47}$$

it gets reduced to

$$\frac{\partial (z_1 \rho_1)}{\partial t} + \frac{\partial (z_1 \rho_1 u)}{\partial x} = 0 \tag{A.48}$$

$$\frac{\partial (z_2 \rho_2)}{\partial t} + \frac{\partial (z_2 \rho_2 u)}{\partial x} = 0 \tag{A.49}$$

$$\frac{Du}{Dt} = -\frac{1}{\rho} \frac{\partial p}{\partial x} \tag{A.50}$$

$$\frac{Dp}{Dt} + \rho a^2 \frac{\partial u}{\partial x} = 0 \tag{A.51}$$

$$\frac{Dz_2}{Dt} = 0 \tag{A.52}$$

Which can be rewritten in term of conserved variables in the form

$$\frac{\partial (z_1\rho_1)}{\partial t} + \frac{\partial (z_1\rho_1 u)}{\partial x} = 0 \tag{A.53}$$

$$\frac{\partial (z_2\rho_2)}{\partial t} + \frac{\partial (z_2\rho_2 u)}{\partial x} = 0 \tag{A.54}$$

$$\frac{\partial (\rho u)}{\partial t} + \frac{\partial (\rho uu + p)}{\partial x} = 0 \tag{A.55}$$

$$\frac{\partial (\rho E)}{Dt} + \frac{\partial [(\rho E + p)\, u]}{\partial x} = 0 \tag{A.56}$$

$$\frac{Dz_2}{Dt} = 0 \tag{A.57}$$

Which is the form of the 5-Equation Transport Model. Although the mathematical derivation of the model requires both phases to be immiscible, the numerical diffusion arising in (A.57) introduces miscibility in the problem, which is addressed with a suitable mixture model. This of course does not affect in any case the mathematical definition of the 5-Equation Transport Model.

APPENDIX B

The computation of convective fluxes using a three-dimensional dimension-by-dimension WENO reconstruction can be easily performed by reconstruction at certain integration points. Assuming that the numerical field is such that all thermodynamic and kinetic variables are known at cell centres, the convective flux at cell interface $i-\frac{1}{2},j,k$

$$\overline{F}^{Inviscid}_{i-\frac{1}{2},j,k}=\overline{F}^{3D\,WENO}_{i-\frac{1}{2},j,k}=\left(\begin{array}{c}(z_1\rho_1)\left(un_\xi+vn_\eta+wn_\zeta\right)\\ \vdots\\ (z_N\rho_N)\left(un_\xi+vn_\eta+wn_\zeta\right)\\ (\rho u)\left(un_\xi+vn_\eta+wn_\zeta\right)+pn_\xi\\ (\rho v)\left(un_\xi+vn_\eta+wn_\zeta\right)+pn_\eta\\ (\rho w)\left(un_\xi+vn_\eta+wn_\zeta\right)+pn_\zeta\\ \rho\left(E+p\right)\left(un_\xi+vn_\eta+wn_\zeta\right)\end{array}\right)_{i-\frac{1}{2},j,k}=\overline{F}^{3D\,WENO}_{i-\frac{1}{2},j,k}\left(\overline{U}^{3D\,WENO}_{i-\frac{1}{2},j,k}\left(\bigcup\overline{U}_{s_i,s_j,s_k}\right)\right) \tag{B.1}$$

where notation $\bigcup\overline{U}_{s_i,s_j,s_k}$ denotes the union of certain cell centre values. For instance, a 5^{th} Order scheme reconstructing at $i-\frac{1}{2},j,k$ is

$$\begin{array}{l}s_i=i-3,...,i+2\\ s_j=j-2,...,j+2\\ s_k=k-2,...,k+2\end{array}\rightarrow\bigcup\overline{U}_{s_i,s_j,s_k}=\underbrace{\overline{U}_{i-3,j-2,k-2},\overline{U}_{i-2,j-2,k-2},...,\overline{U}_{i+2,j-2,k-2},\overline{U}_{i-3,j-1,k-2},...,\overline{U}_{i+2,j+2,k+2}}_{6\times5\times5=150\,Elements} \tag{B.2}$$

Therefore, the problem reduces to find the relationships

$$\overline{F}^{3D\,WENO}_{i-\frac{1}{2},j,k}\left(\overline{U}^{3D\,WENO}_{i-\frac{1}{2},j,k}\right) \tag{B.3}$$

$$\overline{U}^{3D\,WENO}_{i-\frac{1}{2},j,k}\left(\bigcup\overline{U}_{s_i,s_j,s_k}\right) \tag{B.4}$$

First of all, we focus on expression (B.3) above. If one chooses the HLLC approximate Riemann solver from Toro [25] to compute fluxes at the interface, the convective flux can be written in the Cartesian space (ξ,η,ζ) as

$$\overline{F}^{3D\,WENO}_{i-\frac{1}{2},j,k}=\int_{\zeta_{i,j,k-\frac{1}{2}}}^{\zeta_{i,j,k+\frac{1}{2}}}\int_{\eta_{i,j+\frac{1}{2},k}}^{\eta_{i,j+\frac{1}{2},k}}\overline{F}^{HLLC}\left(\overline{U}^{L}\left(\xi_{i-\frac{1}{2},j,k},\eta,\zeta\right),\overline{U}^{R}\left(\xi_{i-\frac{1}{2},j,k},\eta,\zeta\right)\right)d\eta d\zeta \tag{B.5}$$

Integrals above are approximated via numerical integrations in the form

$$\int_{S_{i-\frac{1}{2}}}^{S_{i+\frac{1}{2}}}\phi\left(\varepsilon\right)d\varepsilon=\sum_{p=1}^{T}\Delta\varepsilon_p\phi\left(\frac{S_{i-\frac{1}{2}}+S_{i-\frac{1}{2}}}{2}+a_p\Delta\varepsilon_p\right) \tag{B.6}$$

In case of considering only two integration points in (B.6), T = 2, and following indications made in Titarev et al. [56], the maximum accuracy is found if such integration points are the so-called first and second Gaussian Integration Points

$$a_1 = -\frac{1}{2\sqrt{3}} \quad ; \quad a_1 = +\frac{1}{2\sqrt{3}}$$

Having selected the integration points, expression (B.5) can be integrated in η to obtain

$$\begin{aligned}
&\overline{F}^{3D\,WENO}_{i-\frac{1}{2},j,k} = \\
&= \frac{\Delta\eta}{2}\int_{\zeta_{i,j,k-\frac{1}{2}}}^{\zeta_{i,j,k+\frac{1}{2}}} d\zeta \left\{ \overline{F}^{HLLC}\left(\overline{U}^L\left(\xi_{i-\frac{1}{2},j,k}, \eta_{i-\frac{1}{2},j,k} - \frac{\Delta\eta}{2\sqrt{3}}, \zeta\right), \overline{U}^R\left(\xi_{i-\frac{1}{2},j,k}, \eta_{i-\frac{1}{2},j,k} - \frac{\Delta\eta}{2\sqrt{3}}, \zeta\right)\right)\right. \\
&\qquad \left. + \overline{F}^{HLLC}\left(\overline{U}^L\left(\xi_{i-\frac{1}{2},j,k}, \eta_{i-\frac{1}{2},j,k} + \frac{\Delta\eta}{2\sqrt{3}}, \zeta\right), \overline{U}^R\left(\xi_{i-\frac{1}{2},j,k}, \eta_{i-\frac{1}{2},j,k} + \frac{\Delta\eta}{2\sqrt{3}}, \zeta\right)\right)\right\}
\end{aligned} \tag{B.7}$$

and subsequently integrated in ζ to recover the final form of the flux

$$\begin{aligned}
&\overline{F}^{3D\,WENO}_{i-\frac{1}{2},j,k} = \frac{\Delta\eta\Delta\zeta}{4}\cdot \\
&\left\{ \overline{F}^{HLLC}\left(\overline{U}^L\left(\xi_{i-\frac{1}{2},j,k}, \eta_{i-\frac{1}{2},j,k} - \frac{\Delta\eta}{2\sqrt{3}}, \zeta_{i-\frac{1}{2},j,k} - \frac{\Delta\zeta}{2\sqrt{3}}\right), \overline{U}^R\left(\xi_{i-\frac{1}{2},j,k}, \eta_{i-\frac{1}{2},j,k} - \frac{\Delta\eta}{2\sqrt{3}}, \zeta_{i-\frac{1}{2},j,k} - \frac{\Delta\zeta}{2\sqrt{3}}\right)\right)\right. \\
&+ \overline{F}^{HLLC}\left(\overline{U}^L\left(\xi_{i-\frac{1}{2},j,k}, \eta_{i-\frac{1}{2},j,k} - \frac{\Delta\eta}{2\sqrt{3}}, \zeta_{i-\frac{1}{2},j,k} + \frac{\Delta\zeta}{2\sqrt{3}}\right), \overline{U}^R\left(\xi_{i-\frac{1}{2},j,k}, \eta_{i-\frac{1}{2},j,k} - \frac{\Delta\eta}{2\sqrt{3}}, \zeta_{i-\frac{1}{2},j,k} + \frac{\Delta\zeta}{2\sqrt{3}}\right)\right) \\
&+ \overline{F}^{HLLC}\left(\overline{U}^L\left(\xi_{i-\frac{1}{2},j,k}, \eta_{i-\frac{1}{2},j,k} + \frac{\Delta\eta}{2\sqrt{3}}, \zeta_{i-\frac{1}{2},j,k} - \frac{\Delta\zeta}{2\sqrt{3}}\right), \overline{U}^R\left(\xi_{i-\frac{1}{2},j,k}, \eta_{i-\frac{1}{2},j,k} + \frac{\Delta\eta}{2\sqrt{3}}, \zeta_{i-\frac{1}{2},j,k} - \frac{\Delta\zeta}{2\sqrt{3}}\right)\right) \\
&\left. + \overline{F}^{HLLC}\left(\overline{U}^L\left(\xi_{i-\frac{1}{2},j,k}, \eta_{i-\frac{1}{2},j,k} + \frac{\Delta\eta}{2\sqrt{3}}, \zeta_{i-\frac{1}{2},j,k} + \frac{\Delta\zeta}{2\sqrt{3}}\right), \overline{U}^R\left(\xi_{i-\frac{1}{2},j,k}, \eta_{i-\frac{1}{2},j,k} + \frac{\Delta\eta}{2\sqrt{3}}, \zeta_{i-\frac{1}{2},j,k} + \frac{\Delta\zeta}{2\sqrt{3}}\right)\right)\right\}
\end{aligned} \tag{B.8}$$

So using the face Jacobian from (3.14) one can finally write

$$\overline{F}^{Inviscid} = \beta_{i-\frac{1}{2},j,k}\overline{F}^{3D\,WENO} \tag{B.9}$$

Now, to close the calculation, relation (B.4) has to be defined. One-dimensional reconstruction has to be performed in the 4 integration points of (B.8), providing a function of the form

$$\overline{U}^{3D\,WENO}_{i-\frac{1}{2},j,k}\left(\bigcup \overline{U}_{s_i,s_j,s_k}\right) = \overline{U}^{HLLC}_{i-\frac{1}{2},j,k}\left(\overline{U}^L_{WENO}\left(\bigcup_{\substack{s_i=i-3,\ldots,i+1\\ s_j=j-2,\ldots,j+2\\ s_k=k-2,\ldots,k+2}} \overline{U}_{s_i,s_j,s_k}\right), \overline{U}^R_{WENO}\left(\bigcup_{\substack{s_i=i-2,\ldots,i+2\\ s_j=j-2,\ldots,j+2\\ s_k=k-2,\ldots,k+2}} \overline{U}_{s_i,s_j,s_k}\right)\right)$$

(B.10)

where the vector of conserved variables at the cell interface $\overline{U}^{HLLC}_{i-\frac{1}{2},j,k}$ can be easily computed from Left and Right states by solving the Local Riemann Problem as shown in equation (3.6). The final step then is to generate Left and Right states from values at cell centres. For a general variable ϕ, 5^{th} Order one-dimensional WENO reconstruction at cell interface $i-\frac{1}{2},j,k$ reads

$$\begin{aligned}
\phi^{L}_{i-\frac{1}{2},j,k} &= \phi_{i-1} + \omega_{0_L} v_{0_L} + \omega_{1_L} v_{1_L} + \omega_{2_L} v_{2_L} \\
\phi^{R}_{i-\frac{1}{2},j,k} &= \phi_{i} + \omega_{0_R} v_{0_R} + \omega_{1_R} v_{1_R} + \omega_{2_R} v_{2_R}
\end{aligned} \tag{B.11}$$

$$\begin{aligned}
\omega_{0_L} &= \frac{\alpha_{0_L}}{\alpha_{0_L}+\alpha_{1_L}+\alpha_{2_L}} \qquad \omega_{0_R} = \frac{\alpha_{0_R}}{\alpha_{0_R}+\alpha_{1_R}+\alpha_{2_R}} \\
\omega_{1_L} &= \frac{\alpha_{1_L}}{\alpha_{0_L}+\alpha_{1_L}+\alpha_{2_L}} \qquad \omega_{1_R} = \frac{\alpha_{1_L}}{\alpha_{0_L}+\alpha_{1_L}+\alpha_{2_L}} \\
\omega_{2_L} &= \frac{\alpha_{2_L}}{\alpha_{0_L}+\alpha_{1_L}+\alpha_{2_L}} \qquad \omega_{2_R} = \frac{\alpha_{2_R}}{\alpha_{R_L}+\alpha_{1_R}+\alpha_{2_R}}
\end{aligned} \tag{B.12}$$

$$\begin{aligned}
\alpha_{0_L} &= \frac{d_0}{\left(\varepsilon+\beta_{0_L}\right)^2} \qquad \alpha_{0_R} = \frac{d_0}{\left(\varepsilon+\beta_{0_R}\right)^2} \\
\alpha_{1_L} &= \frac{d_1}{\left(\varepsilon+\beta_{1_L}\right)^2} \qquad \alpha_{1_R} = \frac{d_1}{\left(\varepsilon+\beta_{1_R}\right)^2} \\
\alpha_{2_L} &= \frac{d_2}{\left(\varepsilon+\beta_{2_L}\right)^2} \qquad \alpha_{2_R} = \frac{d_2}{\left(\varepsilon+\beta_{2_R}\right)^2}
\end{aligned} \tag{B.13}$$

with the so-called smoothness indicators β taken from [71]

$$\begin{aligned}
\beta_{0_L} &= \tfrac{13}{12}\left(\phi_{i-1} - 2\phi_i + \phi_{i+1}\right)^2 + \tfrac{1}{4}\left(3\phi_{i-1} - 4\phi_i + \phi_{i+1}\right)^2 \\
\beta_{1_L} &= \tfrac{13}{12}\left(\phi_{i-2} - 2\phi_{i-1} + \phi_i\right)^2 + \tfrac{1}{4}\left(\phi_{i-2} - \phi_i\right)^2 \\
\beta_{2_L} &= \tfrac{13}{12}\left(\phi_{i-3} - 2\phi_{i-2} + \phi_{i-1}\right)^2 + \tfrac{1}{4}\left(\phi_{i-3} - 4\phi_{i-2} + 3\phi_{i-1}\right)^2 \\
\beta_{0_R} &= \tfrac{13}{12}\left(\phi_{i} - 2\phi_{i-1} + \phi_{i-2}\right)^2 + \tfrac{1}{4}\left(3\phi_{i} - 4\phi_{i-1} + \phi_{i-2}\right)^2 \\
\beta_{1_R} &= \tfrac{13}{12}\left(\phi_{i+1} - 2\phi_{i} + \phi_{i-1}\right)^2 + \tfrac{1}{4}\left(\phi_{i+1} - \phi_{i-1}\right)^2 \\
\beta_{2_R} &= \tfrac{13}{12}\left(\phi_{i+2} - 2\phi_{i+1} + \phi_{i}\right)^2 + \tfrac{1}{4}\left(\phi_{i+2} - 4\phi_{i+1} + 3\phi_{i}\right)^2
\end{aligned} \tag{B.14}$$

The residual parameter ε is introduced to prevent the denominator from being 0 and. A typical suitable value for this magnitude is $\varepsilon = 10^{-15}$ for a machine working in double precision. Finally, tables below shows the values of the optimum weights d_0, d_1, d_2 and interpolation stencils v_0, v_1, v_2 for each one-dimensional reconstruction stage in (3.35) at each integration point. It also sketches the solving procedure. Finally, Left and Right primitive variables $z_1\rho_1, ..., z_N\rho_N, u, v, w, p, z_1, ..., z_{N-1}$ can be reconstructed using this procedure to build both vectors of conserved variables $\overline{U}^{L}_{WENO}, \overline{U}^{R}_{WENO}$ and the volume fraction flux for (3.28).

Stage 1. Reconstruction at interface $\xi = \xi_{i,j,k} - \frac{\Delta\xi}{2}$.

$$\begin{cases} Input \rightarrow & \bigcup \quad \phi_{s_i,s_j,s_k} \\ & s_i = i-3,...,i+2 \\ & s_j = j-2,...,j+2 \\ & s_k = k-2,...,k+2 \\ Output \rightarrow & \phi^{L;\xi} = \phi^L\left(\xi_{i,j,k} - \frac{\Delta\xi}{2}, \eta, \zeta\right) \\ & \phi^{R;\xi} = \phi^R\left(\xi_{i,j,k} - \frac{\Delta\xi}{2}, \eta, \zeta\right) \end{cases},$$

	d_0	d_1	d_2	v_0	v_1	v_2
Left	0.3	0.6	0.1	$\frac{1}{6}\left(-4\phi_{i-1}+5\phi_i-\phi_{i+1}\right)$	$\frac{1}{6}\left(-\phi_{i-2}-\phi_{i-1}+2\phi_i\right)$	$\frac{1}{6}\left(-2\phi_{i-3}-7\phi_{i-2}+5\phi_{i-1}\right)$
Right				$\frac{1}{6}\left(-4\phi_i+5\phi_{i-1}-\phi_{i-2}\right)$	$\frac{1}{6}\left(-\phi_{i+1}-\phi_i+2\phi_{i-1}\right)$	$\frac{1}{6}\left(-2\phi_{i+2}-7\phi_{i+1}+5\phi_i\right)$

Stage 2. Reconstruction at Lines

$$\begin{cases} \overline{L}_1 = \left(\xi_{i,j,k} - \frac{\Delta\xi}{2}, \eta_{i,j,k} - \frac{\Delta\eta}{2\sqrt{3}}, \zeta\right) \\ \overline{L}_2 = \left(\xi_{i,j,k} - \frac{\Delta\xi}{2}, \eta_{i,j,k} + \frac{\Delta\eta}{2\sqrt{3}}, \zeta\right) \end{cases} \quad \begin{cases} Input \rightarrow & \phi^{L;\xi} = \phi^L\left(\xi_{i,j,k} - \frac{\Delta\xi}{2}, \eta, \zeta\right) \\ & \phi^{R;\xi} = \phi^R\left(\xi_{i,j,k} - \frac{\Delta\xi}{2}, \eta, \zeta\right) \\ Output \rightarrow & \phi^{L;\xi;1} = \phi^L\left(\overline{L}_1\right); \phi^{R;\xi;1} = \phi^R\left(\overline{L}_1\right) \\ & \phi^{L;\xi;2} = \phi^L\left(\overline{L}_2\right); \phi^{R;\xi;2} = \phi^R\left(\overline{L}_2\right) \end{cases}$$

		d_0	d_1	d_2	v_0	v_1	v_2
$\overline{L}_1$	Left	$\frac{210-\sqrt{3}}{1080}$	$\frac{11}{18}$	$\frac{210+\sqrt{3}}{1080}$	$\frac{\sqrt{3}}{12}\left(3\phi_j^{L;\xi} - 4\phi_{j+1}^{L;\xi} + \phi_{j+2}^{L;\xi}\right)$	$\frac{\sqrt{3}}{12}\left(\phi_{j-1}^{L;\xi} - \phi_{j+1}^{L;\xi}\right)$	$\frac{\sqrt{3}}{12}\left(-3\phi_j^{L;\xi} + 4\phi_{j-1}^{L;\xi} - \phi_{j-2}^{L;\xi}\right)$
	Right				$\frac{\sqrt{3}}{12}\left(3\phi_j^{R;\xi} - 4\phi_{j+1}^{R;\xi} + \phi_{j+2}^{R;\xi}\right)$	$\frac{\sqrt{3}}{12}\left(\phi_{j-1}^{R;\xi} - \phi_{j+1}^{R;\xi}\right)$	$\frac{\sqrt{3}}{12}\left(-3\phi_j^{R;\xi} + 4\phi_{j-1}^{R;\xi} - \phi_{j-2}^{R;\xi}\right)$
$\overline{L}_2$	Left	$\frac{210+\sqrt{3}}{1080}$	$\frac{11}{18}$	$\frac{210-\sqrt{3}}{1080}$	$\frac{\sqrt{3}}{12}\left(-3\phi_j^{L;\xi} + 4\phi_{j+1}^{L;\xi} - \phi_{j+2}^{L;\xi}\right)$	$\frac{\sqrt{3}}{12}\left(-\phi_{j-1}^{L;\xi} + \phi_{j+1}^{L;\xi}\right)$	$\frac{\sqrt{3}}{12}\left(3\phi_j^{L;\xi} - 4\phi_{j-1}^{L;\xi} + \phi_{j-2}^{L;\xi}\right)$
	Right				$\frac{\sqrt{3}}{12}\left(-3\phi_j^{R;\xi} + 4\phi_{j+1}^{R;\xi} - \phi_{j+2}^{R;\xi}\right)$	$\frac{\sqrt{3}}{12}\left(-\phi_{j-1}^{R;\xi} + \phi_{j+1}^{R;\xi}\right)$	$\frac{\sqrt{3}}{12}\left(3\phi_j^{R;\xi} - 4\phi_{j-1}^{R;\xi} + \phi_{j-2}^{R;\xi}\right)$

		Stage 3. Reconstruction at points $\begin{cases} \bar{I}_1 = \left(\xi_{i,j,k} - \frac{\Delta\xi}{2}, \eta_{i,j,k} - \frac{\Delta\eta}{2\sqrt{3}}, \zeta_{i,j,k} - \frac{\Delta\zeta}{2\sqrt{3}}\right) \\ \bar{I}_2 = \left(\xi_{i,j,k} - \frac{\Delta\xi}{2}, \eta_{i,j,k} - \frac{\Delta\eta}{2\sqrt{3}}, \zeta_{i,j,k} - \frac{\Delta\zeta}{2\sqrt{3}}\right) \\ \bar{I}_3 = \left(\xi_{i,j,k} - \frac{\Delta\xi}{2}, \eta_{i,j,k} + \frac{\Delta\eta}{2\sqrt{3}}, \zeta_{i,j,k} - \frac{\Delta\zeta}{2\sqrt{3}}\right) \\ \bar{I}_4 = \left(\xi_{i,j,k} - \frac{\Delta\xi}{2}, \eta_{i,j,k} + \frac{\Delta\eta}{2\sqrt{3}}, \zeta_{i,j,k} + \frac{\Delta\zeta}{2\sqrt{3}}\right) \end{cases}$			$\begin{cases} Input \rightarrow & \begin{cases} \phi^{L;\xi;1}, \phi^{R;\xi;1} \end{cases} = \left\{\phi^L\left(\bar{L}_1\right), \phi^R\left(\bar{L}_1\right)\right\} \\ & \begin{cases} \phi^{L;\xi;2}, \phi^{R;\xi;2} \end{cases} = \left\{\phi^L\left(\bar{L}_2\right), \phi^R\left(\bar{L}_2\right)\right\} \\ Out. \rightarrow & \begin{cases} \phi^{L;\xi;1;1}, \phi^{R;\xi;1;1} \end{cases} = \left\{\phi^L\left(\bar{I}_1\right), \phi^R\left(\bar{I}_1\right)\right\} \\ & \begin{cases} \phi^{L;\xi;1;2}, \phi^{R;\xi;1;2} \end{cases} = \left\{\phi^L\left(\bar{I}_2\right), \phi^R\left(\bar{I}_2\right)\right\} \\ & \begin{cases} \phi^{L;\xi;2;1}, \phi^{R;\xi;2;1} \end{cases} = \left\{\phi^L\left(\bar{I}_3\right), \phi^R\left(\bar{I}_3\right)\right\} \\ & \begin{cases} \phi^{L;\xi;2;2}, \phi^{R;\xi;2;2} \end{cases} = \left\{\phi^L\left(\bar{I}_4\right), \phi^R\left(\bar{I}_4\right)\right\} \end{cases}$		
		d_0	d_1	d_2	v_0	v_1	v_2
$\bar{I}_1$	Left	$\frac{210-\sqrt{3}}{1080}$	$\frac{11}{18}$	$\frac{210+\sqrt{3}}{1080}$	$\frac{\sqrt{3}}{12}\left(3\phi_k^{L;\xi;1} - 4\phi_{k+1}^{L;\xi;1} + \phi_{k+2}^{L;\xi;1}\right)$	$\frac{\sqrt{3}}{12}\left(\phi_{k-1}^{L;\xi;1} - \phi_{k+1}^{L;\xi;1}\right)$	$\frac{\sqrt{3}}{12}\left(-3\phi_k^{L;\xi;1} + 4\phi_{k-1}^{L;\xi;1} - \phi_{k-2}^{L;\xi;1}\right)$
	Right				$\frac{\sqrt{3}}{12}\left(3\phi_k^{R;\xi;1} - 4\phi_{k+1}^{R;\xi;1} + \phi_{k+2}^{R;\xi;1}\right)$	$\frac{\sqrt{3}}{12}\left(\phi_{k-1}^{R;\xi;1} - \phi_{k+1}^{R;\xi;1}\right)$	$\frac{\sqrt{3}}{12}\left(-3\phi_k^{R;\xi;1} + 4\phi_{k-1}^{R;\xi;1} - \phi_{k-2}^{R;\xi;1}\right)$
$\bar{I}_2$	Left	$\frac{210+\sqrt{3}}{1080}$	$\frac{11}{18}$	$\frac{210-\sqrt{3}}{1080}$	$\frac{\sqrt{3}}{12}\left(-3\phi_k^{L;\xi;1} + 4\phi_{k+1}^{L;\xi;1} - \phi_{k+2}^{L;\xi;1}\right)$	$\frac{\sqrt{3}}{12}\left(-\phi_{k-1}^{L;\xi;1} + \phi_{k+1}^{L;\xi;1}\right)$	$\frac{\sqrt{3}}{12}\left(3\phi_k^{L;\xi;1} - 4\phi_{k-1}^{L;\xi;1} + \phi_{k-2}^{L;\xi;1}\right)$
	Right				$\frac{\sqrt{3}}{12}\left(-3\phi_k^{R;\xi;1} + 4\phi_{k+1}^{R;\xi;1} - \phi_{k+2}^{R;\xi;1}\right)$	$\frac{\sqrt{3}}{12}\left(-\phi_{k-1}^{R;\xi;1} + \phi_{k+1}^{R;\xi;1}\right)$	$\frac{\sqrt{3}}{12}\left(3\phi_k^{R;\xi;1} - 4\phi_{k-1}^{R;\xi;1} + \phi_{k-2}^{R;\xi;1}\right)$
$\bar{I}_3$	Left	$\frac{210-\sqrt{3}}{1080}$	$\frac{11}{18}$	$\frac{210+\sqrt{3}}{1080}$	$\frac{\sqrt{3}}{12}\left(3\phi_k^{L;\xi;2} - 4\phi_{k+1}^{L;\xi;2} + \phi_{k+2}^{L;\xi;2}\right)$	$\frac{\sqrt{3}}{12}\left(\phi_{k-1}^{L;\xi;2} - \phi_{k+1}^{L;\xi;2}\right)$	$\frac{\sqrt{3}}{12}\left(-3\phi_k^{L;\xi;2} + 4\phi_{k-1}^{L;\xi;2} - \phi_{k-2}^{L;\xi;2}\right)$
	Right				$\frac{\sqrt{3}}{12}\left(3\phi_k^{R;\xi;2} - 4\phi_{k+1}^{R;\xi;2} + \phi_{k+2}^{R;\xi;2}\right)$	$\frac{\sqrt{3}}{12}\left(\phi_{k-1}^{R;\xi;2} - \phi_{k+1}^{R;\xi;2}\right)$	$\frac{\sqrt{3}}{12}\left(-3\phi_k^{R;\xi;2} + 4\phi_{k-1}^{R;\xi;2} - \phi_{k-2}^{R;\xi;2}\right)$
$\bar{I}_4$	Left	$\frac{210+\sqrt{3}}{1080}$	$\frac{11}{18}$	$\frac{210-\sqrt{3}}{1080}$	$\frac{\sqrt{3}}{12}\left(-3\phi_k^{L;\xi;2} + 4\phi_{k+1}^{L;\xi;2} - \phi_{k+2}^{L;\xi;2}\right)$	$\frac{\sqrt{3}}{12}\left(-\phi_{k-1}^{L;\xi;2} + \phi_{k+1}^{L;\xi;2}\right)$	$\frac{\sqrt{3}}{12}\left(3\phi_k^{L;\xi;2} - 4\phi_{k-1}^{L;\xi;2} + \phi_{k-2}^{L;\xi;2}\right)$
	Right				$\frac{\sqrt{3}}{12}\left(-3\phi_k^{R;\xi;2} + 4\phi_{k+1}^{R;\xi;2} - \phi_{k+2}^{R;\xi;2}\right)$	$\frac{\sqrt{3}}{12}\left(-\phi_{k-1}^{R;\xi;2} + \phi_{k+1}^{R;\xi;2}\right)$	$\frac{\sqrt{3}}{12}\left(3\phi_k^{R;\xi;2} - 4\phi_{k-1}^{R;\xi;2} + \phi_{k-2}^{R;\xi;2}\right)$

Table 6.1: Optimum weights and interpolation stencils for each integration stage and integration point.